

# TECHNICAL REPORT 00-06

Grimsel Test Site  
Investigation Phase IV (1994-1996)

**The Nagra-JNC in situ study of safety  
relevant radionuclide retardation  
in fractured crystalline rock**

**II: The RRP project methodology  
development, field and laboratory tests**

July 2003

Edited by W.R. Alexander, K. Ota and B. Frieg



# TECHNICAL REPORT 00-06

Grimsel Test Site  
Investigation Phase IV (1994-1996)

**The Nagra-JNC in situ study of safety  
relevant radionuclide retardation  
in fractured crystalline rock**

**II: The RRP project methodology  
development, field and laboratory tests**

July 2003

Edited by W.R. Alexander<sup>1)</sup>, K. Ota<sup>2)</sup> and B. Frieg<sup>1)</sup>

<sup>1)</sup> Nagra, Wettingen, Switzerland

<sup>2)</sup> JNC (Japan Nuclear Cycle Development Institute),  
Tono Geoscience Centre, Gifu, Japan

This report was prepared on behalf of Nagra. The viewpoints presented and conclusions reached are those of the author(s) and do not necessarily represent those of Nagra.

**ISSN 1015-2636**

"Copyright © 2003 by Nagra, Wettingen (Switzerland) / All rights reserved.

All parts of this work are protected by copyright. Any utilisation outwith the remit of the copyright law is unlawful and liable to prosecution. This applies in particular to translations, storage and processing in electronic systems and programs, microfilms, reproductions, etc."

## Foreword

Concepts for the disposal of radioactive waste in geological formations depend crucially on a thorough knowledge of relevant processes in the host rock and on an understanding of the whole repository system, comprising both engineered and geological barriers. The Grimsel Test Site (GTS) is an underground rock laboratory which is used to investigate many of these processes in hard, fractured rocks. It has been operated since 1984 by the Swiss National Co-operative for the Disposal of Radioactive Waste (Nagra).

The laboratory is located in the crystalline rock of the Central Aare Massif, 450 m below the eastern flank of the Juchlistock at an altitude of 1730 m. It is reached via a 1200 m long horizontal access tunnel, operated by the hydroelectric power company KWO. The layout of the tunnels that comprise the GTS allowed the establishment of a radiation controlled zone (IAEA type C in 1990, being upgraded to Type B in 1996) in which experiments with radioactive tracers are carried out. With increasing experience in the implementation of *in situ* experiments, improved process understanding and more advanced repository concepts, the experimental programmes at the GTS have gradually become more complex and more directly related to open questions defined by performance assessors or by regulatory bodies. Demonstration of disposal concepts by performing large- or full-scale, long-term experiments has also become a key aspect of investigations in the rock laboratory. The GTS Phase IV, 1994 – 1996, was initiated in close co-operation with a number of international partner organisations. The programmes which were carried out focussed on the characterisation and conceptualisation of the tunnel nearfield, geophysical investigations and experiments related to *in situ* radionuclide retardation.

Within the current investigation phase (Phase V, 1997 – 2002) seven experimental programmes and projects are included (see [www.grimsel.com](http://www.grimsel.com) for details).

Within GTS Phase IV, the Nagra-JNC Radionuclide Migration Programme (RMP) examined the behaviour of a large suite of radionuclides in the geosphere. The Radionuclide Retardation Project (RRP) is an integral part of RMP, beginning in 1990 and continuing until 1998, and this report summarises the results of the Excavation Project (EP) for the period 1991 – 1995 (for Phase I see ALEXANDER & KAWAMURA 1992, which provides the results of a desk-top feasibility study). The main aim of RRP Phase II was a laboratory and field feasibility study which took the methods and techniques identified in Phase I and tested (and further developed) them under relevant conditions. As such, the report covers three main areas: first, shear zone preservation techniques (mainly covering development of the resin which was injected into the field site), second, overcoring tests and methodology improvements and third, defining appropriate radiochemical analytical techniques for the specimens which were finally delivered to the laboratories (in Phase III).

This report is one of a series of four Nagra Technical Reports (NTBs) on RMP, including NTB 00-07 (EP-Phase III, Radionuclide Retardation Project RRP final report), NTB 00-08 (Connected Porosity CP report) and NTB 00-09 (Radionuclide Migration Experiment MI report), all of which will be synthesised in ALEXANDER et al. (2003a).

## Vorwort

Bei Lagerkonzepten für die Entsorgung radioaktiver Abfälle in geologischen Formationen sind eine vertiefte Kenntnis der relevanten Prozesse im Wirtgestein sowie ein Verständnis des gesamten Lagersystems mit den technischen und geologischen Barrieren von entscheidender Bedeutung. Im Felslabor Grimsel (FLG) werden zahlreiche dieser Prozesse in geklüftetem Festgestein untersucht. Es wird seit 1984 von der Nagra (Nationale Genossenschaft für die Lagerung radioaktiver Abfälle) betrieben.

Das FLG befindet sich im Kristallingestein des Zentralen Aarmassives 450 m unterhalb der Ostflanke des Juchlistocks auf einer Höhe von 1730 m ü.M. und kann durch einen 1200 m langen horizontalen Zugangstollen der Kraftwerke Oberhasli AG (KWO) erreicht werden. 1990 wurde in einem Stollenabschnitt des FLG eine kontrollierte Zone (IAEA Typ B 1990, Höherstufung auf Typ C 1996) für Versuche mit radioaktiven Tracern eingerichtet. Mit zunehmender Erfahrung bei der Durchführung von In-situ-Feldversuchen und verbessertem Systemverständnis der weiter entwickelten Lagerkonzepte, verlagerten sich die experimentellen Programmschwerpunkte hin zu komplexen, direkt auf die Anforderungen der Sicherheitsanalyse und Behörden ausgerichteten Versuche. Langzeit-Demonstrationsversuche in grösserem oder Originalmassstab gewannen im Felslabor zunehmend an Bedeutung. Die FLG Untersuchungsphase IV (1994 – 1996) wurde in enger Zusammenarbeit mit einer Anzahl internationaler Partnerorganisationen geplant. Die durchgeführten Versuchsprogramme konzentrierten sich auf die Charakterisierung und Konzeptualisierung des Tunnelnahfeldbereichs mit geophysikalischen Methoden und Versuchen zur Radionuklidrückhaltung.

Die jetzige Untersuchungsphase (Phase V, 1997 – 2002) umfasst sieben Versuchsprogramme und -projekte (siehe auch [www.grimsel.com](http://www.grimsel.com) für Einzelheiten).

Innerhalb der FLG Phase IV wurde mit dem Nagra-JNC Radionuklid-Migrationsprojekt (Radionuclide Migration Programme, RMP) das Verhalten einer Reihe von Radionukliden in der Geosphäre untersucht. Das Projekt Radionuklidretardation (Radionuclide Retardation Project RRP) ist ein eigenständiges Teilprojekt von RMP, das 1990 begonnen und bis 1998 fortgeführt wurde. Der vorliegende Bericht fasst die im Zeitraum 1991 – 1995 erhobenen Daten für das Exkavationsprojekt (Excavation Project EP) zusammen (Phase I, siehe ALEXANDER & KAWAMURA 1992, dort sind die Resultate einer Desktop-Machbarkeitsstudie dargelegt). Die Hauptzielsetzung von RRP Phase II war eine Labor- und Feldmachbarkeitsstudie, bei der die in Phase I identifizierten Methoden und Technologien unter entsprechenden Bedingungen getestet (und weiter entwickelt) wurden. Der Bericht umfasst drei Themenschwerpunkte: 1. Verfahren zur Konservierung der Scherzone (dabei v. a. die Entwicklung des im Feldversuch injizierten Harzes), 2. Überbohrtests und Verbesserung der Methodik sowie 3. Festlegung geeigneter radiochemischer Analyseverfahren für die Proben, die schliesslich an die Labors geliefert wurden (in Phase III).

Der vorliegende Bericht ist Teil einer Reihe von vier Nagra Technischen Berichten (NTB) zum Thema RMP, zusammen mit NTB 00-07 (Schlussbericht RRP, Radionuclide Retardation Project, EP Phase III), NTB 00-08 (Bericht CP, Connected Porosity) und NTB 00-09 (MI Bericht, Radionuclide Migration Experiment), deren Synthese in ALEXANDER et al. (2003a) dargelegt ist.

## Préface

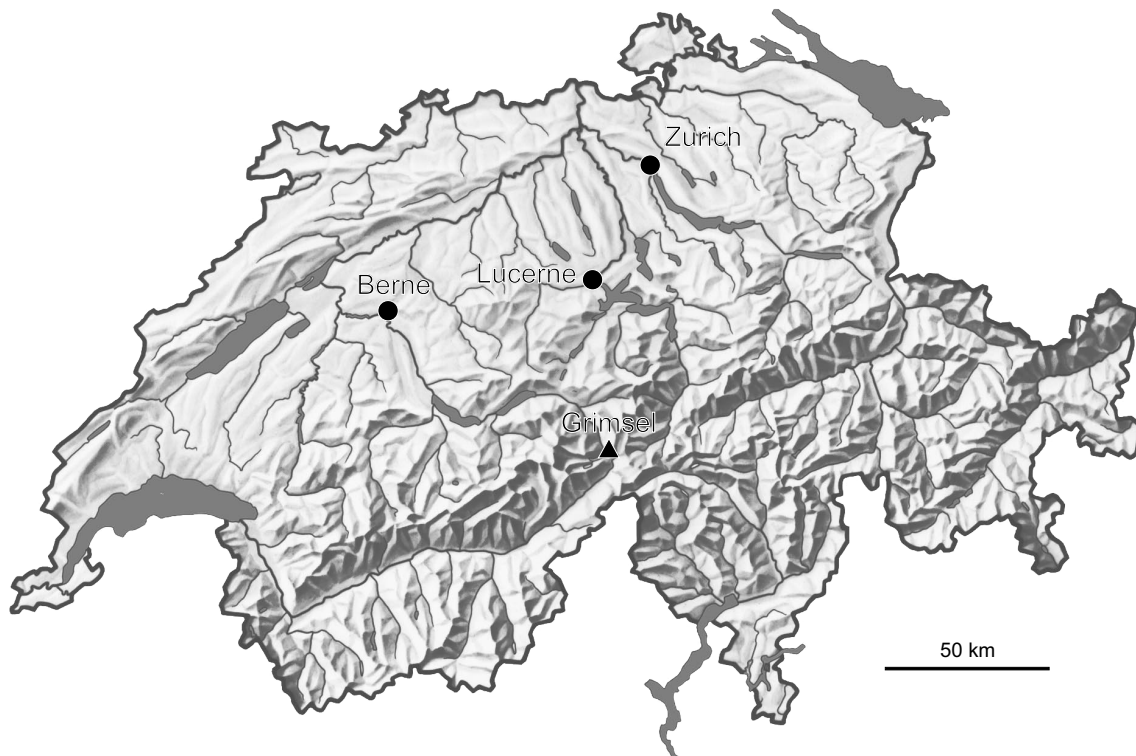
Les concepts développés pour le dépôt de déchets radioactifs dans des formations géologiques dépendent étroitement d'une connaissance approfondie des processus significatifs qui se déroulent dans la roche d'accueil et de la compréhension globale de tout le système de dépôt, comprenant les barrières techniques et les barrières géologiques. Le laboratoire souterrain du Grimsel (LSG) est un laboratoire souterrain destiné à l'investigation de nombre de ces processus se déroulant en roche cohérente fissurée. En fonction depuis 1984, il est exploité par la Société coopérative nationale pour l'entreposage de déchets radioactifs (Nagra).

Le laboratoire est situé à une altitude de 1730 m dans les roches granitiques du Massif Central de l'Aar, à 450 m de profondeur sous le flanc est du Juchlistock. On l'atteint par un tunnel d'accès horizontal à une longueur de 1200 m exploité par la centrale électrique de Oberhasli de la société KWO. La disposition des galeries qui accueillent le LSG a permis l'aménagement en 1990 d'une zone de radiation contrôlée (type B selon l'AIEA en 1990, classée type C – catégorie supérieure – à partir de 1996) dans laquelle sont effectués des essais utilisant des traceurs radioactifs. Au fil des expériences acquises dans la réalisation des essais in-situ, d'une connaissance améliorée des processus et de l'évolution des concepts de dépôts, les programmes expérimentaux au LSG ont gagné en complexité et ont été mieux reliés aux questions en suspens posées par les analystes de la sûreté ou par les autorités de surveillance. La démonstration de faisabilité de concepts de dépôt sur la base d'expériences à grande échelle ou à l'échelle réelle et à long terme est devenue un élément clé des recherches au laboratoire souterrain. La phase IV du LSG, conduite de 1994 à 1996, a été mise sur pied en collaboration étroite avec plusieurs organisations partenaires au niveau international. Les programmes réalisés ont mis l'accent sur la caractérisation et la conceptualisation du champ proche de la galerie, déjà ausculté par les investigations géophysiques et les essais du retardement des radioéléments.

La phase V des investigations, actuellement en cours (1997 – 2002), comprend sept projets et programmes expérimentaux (cf. [www.grimsel.com](http://www.grimsel.com), pour détails).

Au cours de la phase IV du GTS, le programme d'étude de la migration des radioéléments (Radionuclide Migration Programme, RMP) de la Nagra et du JNC a étudié le comportement dans la géosphère de toute une série de radioéléments. Le projet de retardement des radioéléments (Radionuclide Retardation Project, RRP), commencé en 1990 et poursuivi jusqu'en 1998, fait partie du RMP. Le présent rapport résume les résultats du projet d'excavation (Excavation Project, EP) pour la période 1991 – 1995 (pour la phase I, voir ALEXANDER & KAWAMURA 1992, qui présente les résultats d'une étude théorique de faisabilité). L'objectif principal de la phase II du RRP était une étude de faisabilité en laboratoire et sur le terrain, reprenant les techniques et méthodes de la phase I et les testant (avec des développements) dans des conditions représentatives. Le rapport présente donc trois volets principaux: d'abord les techniques de préservation de la zone faillée (comprenant essentiellement le développement de la résine injectée dans la roche), ensuite des tests de surcarottage avec des développements méthodologiques, enfin la recherche de techniques analytiques radiochimiques appropriées pour l'analyse des échantillons livrés aux laboratoires au cours de la phase III.

Le présent rapport est un des quatre rapports techniques de la Nagra (NTB) sur le programme RMP. Cet ensemble comprend aussi le NTB 00-07 (rapport final RRP, Radionuclide Retardation Project, EP-Phase III), le NTB 00-08 (rapport CP, Connected Porosity) et le NTB 00-09, (rapport MI, Radionuclide Migration Experiment). Tous ces rapports seront présentés sous forme synthétique dans ALEXANDER et al. (2003a).



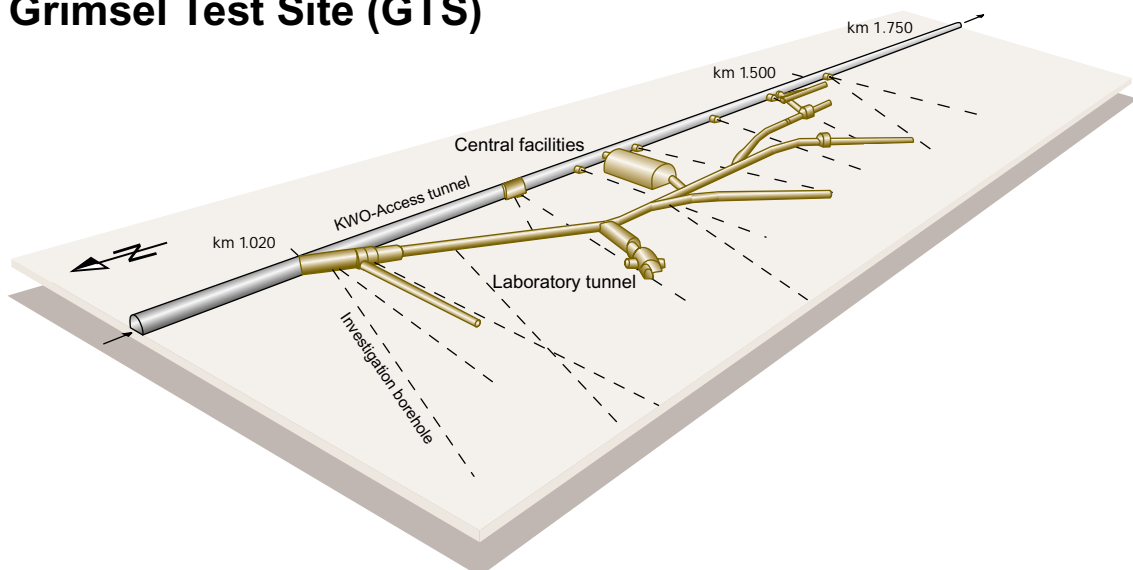
Location of Nagra's underground test facility at the Grimsel Pass in the Central Alps (Bernese Alps) of Switzerland

## Grimsel area (view to the west)



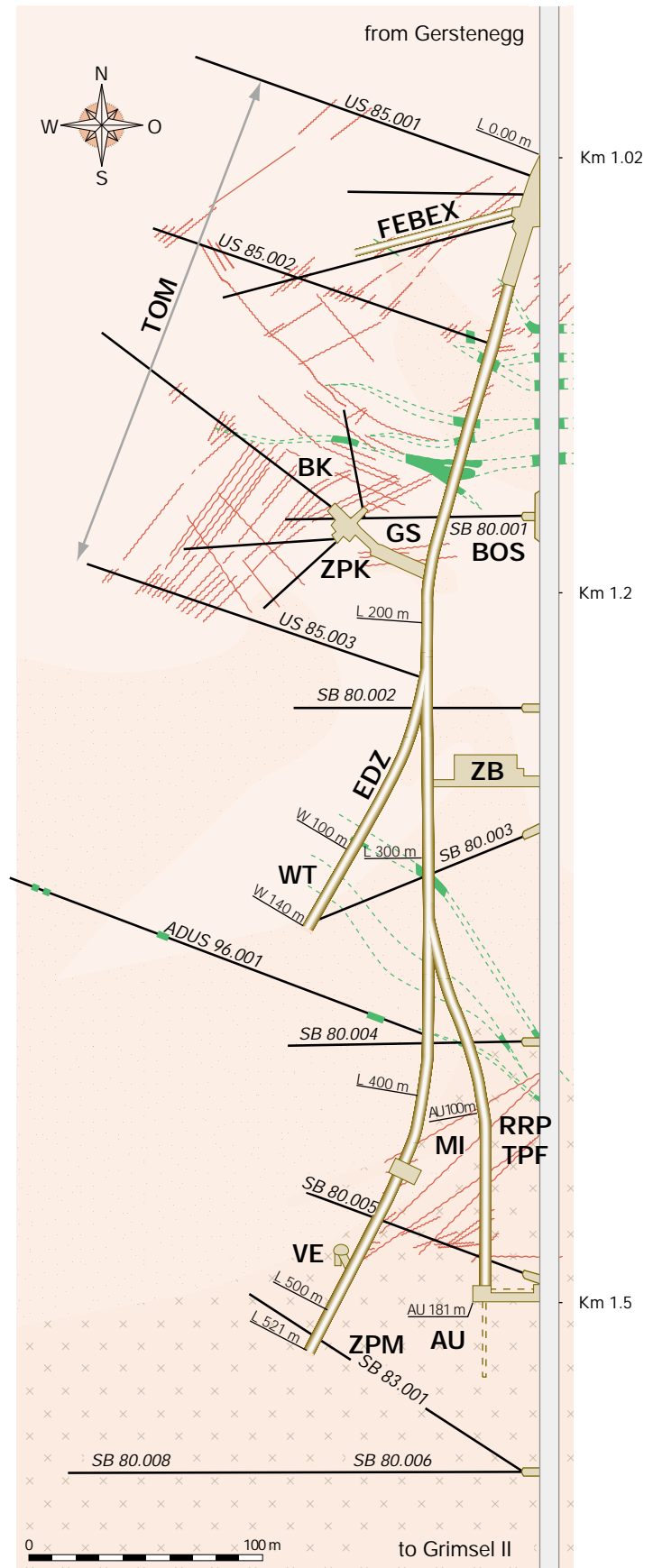
1 Grimsel Test Site    2 Lake Raeterichsboden    3 Lake Grimsel    4 Juchlistock

## Grimsel Test Site (GTS)



# Grimsel Test Site GTS

-  KWO-Access tunnel
-  Laboratory tunnel
-  Central Aaregranite (CAGR)  
High biotite content CAGR
-  Grimsel-Granodiorite
-  Shear zone
-  Lamprophyre
-  Investigation borehole
- ZB** Central facilities
- BK** Fracture system flow
- GS** Rock stresses
- MI** Migration
- VE** Ventilation test
- WT** Heater test
- GTS Phase IV 1994-1996**
- BOS** Borehole Sealing
- TOM** Further Development of Seismic Tomography
- EDZ** Excavation Disturbed Zone
- TPF** Two-Phase Flow
- RRP** Radionuclide Retardation Project
- ZPK** Two-Phase Flow in Fracture Networks of the Tunnel Near-field
- ZPM** Two-Phase Flow in the Unsaturated Matrix of Crystalline Rocks
- FEBEX** 1:1 EBS – Demonstration (HLW)



## Summary

The Nagra-JNC<sup>1</sup> Excavation Project (EP) was a very challenging project where, for the first time, a radionuclide cocktail of strongly sorbing radionuclides was injected into a water-conducting shear zone, followed by the excavation of the traced part of the shear zone (approximately two tonnes of rock). The development, improvement and testing of new methodologies and techniques were required due to the complexity of the project and to the scale of the *in situ* experiment. The extensive efforts which were undertaken in order to guarantee a successful experiment also required a series of laboratory and field tests (at Nagra's Grimsel Test Site, GTS), the latter wherever possible under conditions closely resembling the final experiment.

In this report, the preparation work for the shear zone immobilisation prior to overcoring and the evaluation of the appropriate solid phase analysis techniques following core recovery are presented in detail. Several existing immobilisation techniques were compared and the best compromise was found to be impregnation of the very friable shear zone with a two component epoxy resin (this was also shown to be capable of preserving the fault gouge within the shear zone). The most important criteria considered were viscosity, density, polymerisation time and constancy of the resin volume during polymerisation, wetting properties of water-wet surfaces in the pore space, homogeneous mixing with various dyes and limited sorption of radionuclides.

The physical properties were determined by the resin producers while the impregnation properties were investigated in the laboratory using wet crushed rock (Valanginian Marl) and then fault gouge material from the experimental shear zone. Wetting of the pore space was enhanced by injecting isopropanol prior to the resin injection (in effect replacing the pore water with isopropanol). In order to optimise the injection system, a suite of laboratory and small-scale field tests were performed at the GTS, examining various features of the system such as the applied injection pressure, the method of injecting isopropanol and how best to control the mixing ratio of the resin and hardener. This work revealed satisfactory pore space impregnation, with the resin penetrating open fractures and fault gouge zones at depth in the rock. Consequently, a larger scale field test was carried out to examine both shear zone impregnation over experimentally relevant distances and the subsequent overcoring methodology. The overcoring tests indicated that only a triple-barrel drillcore could guarantee full core recovery and that overcoring in the plane of the shear zone was much better than overcoring perpendicular to the shear zone.

Besides guaranteeing immobilisation of the shear zone, it was necessary that the resin did not disturb the existing radionuclide-rock distribution and so a series of sorption experiments was carried out on a suite of resins. Standard batch sorption experiments were carried out with resin impregnated rock samples and radionuclide-spiked groundwater from the shear zone to study potential competition between resin and granodiorite. In addition, to more precisely emulate the *in situ* conditions during the experiment, spiked rock samples were immersed in liquid epoxy resin, again to study potential competition between resin and granodiorite. The experiments clearly showed that resin impregnation would not significantly influence the *in situ* radionuclide distribution.

The assessment of surface analytical and radiochemical techniques for core analysis focussed on SIMS (secondary ion mass spectrometry) and LAM-ICP-MS (laser ablation microprobe – inductively coupled plasma – mass spectrometry). The studies were done using a range of samples from the experimental shear zone in order to evaluate the influence of surface

---

<sup>1</sup> The Japan Nuclear Cycle Development Institute (previously PNC, Power Reactor and Nuclear Fuel Development Corporation).

roughness, charge neutralisation sample requirements and outgassing of impregnated samples. SIMS could obtain elemental distributions from mineral grains whereas, with LAM-ICP-MS measurements, pre-investigation with SEM (scanning electron microscopy) and BSEM (back-scattered electron microscopy) proved necessary. Additional sample analysis using EMPA (electron microprobe analysis) showed that the technique provides reasonable results only on the rock (granodiorite) surfaces, while, in natural and synthetic fault gouge, a significant degree of beam-wandering made point analysis impossible. Quantitative analysis showed that most minerals have simple composition with little variation within a sample and should be a good internal standard for the laser ablation studies.

Finally, because of potential damage to the cores during sub-sampling, it was decided to assess the possibility of remotely investigating the shear zone structure (channelling, pore distribution, etc.) on the recovered core lengths. Several techniques were tested including PET (positron emission tomography) and MR (micro-resistivity). PET proved to be impractical due to sample size restrictions and very long counting times. In addition, relatively high activities were required to obtain high definition images. Nevertheless, it was felt that PET had good potential for real-time imaging of radionuclide transport through cores in the laboratory and that this would be worth further investigation. MR was also shown to have some promise but a complete lack of background information on MR applications to crystalline rock meant that a large research and development programme would have been necessary. As this was outwith the scope of the EP, it was decided not to take MR further.

This phase of work in the EP indicated that the full scale field experiment could proceed with a reasonable guarantee of a successful outcome using existing techniques adapted to the *in situ* conditions in the experimental shear zone (the full experiment is described in MÖRI et al. 2003a). In addition, some of the techniques developed here have since been applied in both JNC's Kamaishi Test Site in north-east Japan and in SKB's Äspö site in southern Sweden.

## Zusammenfassung

Das von der Nagra und von JNC<sup>2</sup> initiierte Exkavationsprojekt (EP) stellte für alle Beteiligten eine grosse Herausforderung dar, da erstmalig in einem Felslabor ein Cocktail stark sorbierender Radionuklide in eine wasserführende Scherzone injiziert und anschliessend das gesamte Fließfeld exkaviert wurde (ca. zwei Tonnen Gestein). Die Komplexität und der Massstab dieses In-situ-Experiments erforderten die Entwicklung, Verbesserung und den Test neuer Methoden und Techniken. Um den Erfolg des angestrebten Hauptexperiments gewährleisten zu können, wurde ausserdem eine Anzahl umfangreicher Labor- und Feldtests im Felslabor Grimsel der Nagra durchgeführt. Letztere wurden weitgehend unter den für das Hauptexperiment erwarteten Bedingungen durchgeführt.

Im vorliegenden Bericht werden die Vorbereitungsarbeiten für die Stabilisierung der Scherzone vor dem Überbohren sowie die Evaluation geeigneter Analysemethoden zur Untersuchung des Gesteinsmaterials aus den entnommenen Bohrkernen ausführlich dargelegt. Der Vergleich verschiedener bestehender Stabilisierungstechniken ergab, dass ein Zweikomponenten-Epoxidharz zur Imprägnierung der Test-Scherzone und zur Konservierung bzw. Erhaltung des bröckeligen Materials der Kluftfüllung (fault gouge) am besten geeignet ist. Bei diesem Evaluationsprozess mussten folgende Kriterien berücksichtigt werden: Viskosität, Dichte, Polymerisationszeit und Volumenkonstanz des Harzes während der Polymerisation, Benetzbarkeit der Oberflächen der wassergesättigten Poren, homogene Mischbarkeit mit verschiedenen Farbstoffen sowie geringe Radionuklidsorption.

Die physikalischen Eigenschaften wurden von den Harzherstellern bestimmt, während die Imprägnierungseigenschaften im Labor sowohl mit nassem, zermahlenem Gestein (z. B. Valangienmergel) als auch mit "fault gouge"-Probenmaterial aus der betreffenden Test-Scherzone getestet wurden. Die Benetzbarkeit des Porenraums konnte durch die Injektion von Isopropanol unmittelbar vor der eigentlichen Harzinjektion (d. h. das Porenwasser wurde durch Isopropanol ersetzt) verbessert werden. Zur Optimierung des Injektionsvorgangs wurden zusätzliche Labor- und Feldexperimente im Felslabor Grimsel durchgeführt und dabei u. a. Injektionsdruck, Injektionsmethodik und Kontrollmöglichkeiten des Mischungsverhältnisses von Harz und Härter untersucht. Diese Untersuchungen führten zu einer erfolgreichen Imprägnierung des Porenraums innerhalb der Scherzone, wobei das Harz in offene Bruchflächen und mit "fault gouge" verfüllte Bereiche der Scherzone eingedrungen war. Danach wurde vor dem eigentlichen In-situ-Hauptexperiment ein Feldversuch in grösserem Massstab durchgeführt, um die Imprägnierung der Scherzone über experimentell relevante Distanzen sowie die Überbohrtechnik zu untersuchen. Die Erfahrungen aus den Überbohrungsversuchen zeigten, dass nur mit einem Dreifachkernrohr ein vollständiger Kerngewinn erzielt werden konnte und dass die Überbohrung parallel zur Scherzone bedeutend bessere Resultate lieferte als senkrecht dazu.

Neben der Stabilisierung der Scherzone musste auch sichergestellt werden, dass die Harzinjektion nicht die vorhandene Verteilung der Radionuklide im Gestein verändern durfte. Deshalb wurde zusätzlich eine Reihe von Sorptionsexperimenten an verschiedenen Harztypen durchgeführt. Konventionelle Batch-Versuche an harzprägnierten Gesteinsproben und mit Radionukliden versetztem Grundwasser aus der Scherzone wurden durchgeführt, um eine mögliche Konkurrenz zwischen Harz und Granodiorit zu bestimmen. Um die In-situ-Bedingungen während des Experiments noch näher simulieren zu können, wurden zusätzlich mit Radionukliden dotierte Gesteinsproben in flüssiges Harz eingetaucht und wiederum das Konkurrenzverhalten zwischen Harz und Granodiorit untersucht. Die Experimente zeigten eindeutig, dass die Harz-

---

<sup>2</sup> The Japan Nuclear Cycle Development Institute (früher PNC, Power Reactor and Nuclear Fuel Development Corporation).

imprägnierung zu keiner massgeblichen Beeinflussung der In-situ-Verteilung der Radionuklide führt.

Die Auswertung der oberflächenanalytischen Techniken und der radiochemischen Methoden zur Kernanalyse konzentrierte sich v. a. auf SIMS ("Secondary Ion Mass Spectrometry") und LAM-ICP-MS ("Laser Ablation Microprobe – Inductively Coupled Plasma – Mass Spectrometry"). Die Studien an einer Reihe von Proben aus der Test-Scherzone hatten zum Ziel, den Einfluss der Oberflächenbeschaffenheit (Rauigkeit), die Ladungsneutralität der Proben sowie Ausgasungserscheinungen zu untersuchen. Mithilfe von SIMS konnten direkt Elementverteilungen auf dem Mineralkorn bestimmt werden, während sich für LAM-ICP-MS-Messungen Voruntersuchungen mit SEM ("Scanning Electron Microscopy") und BSEM ("Back Scattered Electron Microscopy") als sehr hilfreich erwiesen. Zusätzliche Analysen mit dem EMPA-Verfahren ("Electron Microprobe Analysis") führten nur auf Granodioritoberflächen zum Erfolg, während in natürlichem und synthetischem "fault gouge"-Material eine Punktmessung durch eine nicht zu vernachlässigende Strahlenwanderung verhindert wurde.

Aufgrund des vereinzelt zu erwartenden Kernmaterialverlustes bei der Probenherstellung aus den Bohrkernen (Bohrkernscheiben) wurde ausserdem die Möglichkeit der Scherzonencharakterisierung am intakten Kern untersucht (Visualisierung von Fliesswegen, Verteilung des Porenraums etc.). Dabei wurden verschiedene Techniken evaluiert, wie auch PET ("Positron Emission Tomography") und MR ("Micro-Resistivity"). PET erwies sich wegen der Einschränkungen bei der Probengrösse sowie den sehr langen Zählraten als nicht praktikabel. Zudem erfordert diese Technik relativ hohe Aktivitäten, um eine ausreichende Auflösung erzielen zu können. Dennoch wird PET als eine geeignete Labormethode erachtet, mit der in Echtzeit der Radionuklid-Transport durch Bohrkern im Labor visualisiert werden kann. Auch die MR-Methode erschien zunächst vielversprechend, mangels bereits vorhandener praktischer Erfahrungen im Bereich kristalliner Gesteine hätte aber das hierzu nötige Forschungs- und Entwicklungsprogramm den Rahmen des EP gesprengt. Daher wurde beschlossen, diese Methode nicht weiter zu verfolgen.

Die in dieser Phase des EP gewonnenen Erkenntnisse führten zu der Überzeugung, dass das geplante In-situ-Hauptexperiment erfolgreich durchgeführt werden kann. Die ausgewählten Methoden und Techniken konnten den speziellen Anforderungen, die an ein solches Feldexperiment in diesem Massstab gestellt werden, angepasst werden (das Feldexperiment ist in MÖRI et al. 2003a beschrieben). Einige der für dieses Experiment entwickelten Techniken konnten inzwischen bereits in JNC's Kamaishi Test Site in Nordost-Japan sowie in SKB's Äspö-Labor in Süd-Schweden angewendet werden.

## Résumé

Le projet d'excavation (Excavation Project, EP) de la Nagra et du JNC<sup>3</sup> représente un défi important car pour la première fois un cocktail de radioéléments fortement adsorbants a été injecté in situ dans une zone de cisaillement aquifère, puis la partie de la zone de cisaillement envahie par les traceurs a été excavée (environ deux tonnes de roche). La complexité du projet et la grande échelle de l'expérience in situ ont nécessité le développement et le test de nouvelles méthodologies et techniques. Les efforts importants investis pour garantir le succès de l'expérience comprennent aussi une série d'essais en laboratoire et sur le terrain (au LSG, le laboratoire souterrain du Grimsel) menés dans des conditions aussi proches que possible de celles de l'expérience finale.

Le présent rapport présente en détail les travaux de préparation pour l'immobilisation de la zone de cisaillement avant le surforage, ainsi que l'évaluation des techniques appropriées d'analyse de la phase solide faisant suite à la récupération des carottes. Différentes techniques d'immobilisation existantes ont été comparées. Un compromis optimal a été trouvé, consistant à imprégner la zone de cisaillement très friable avec une résine epoxy à 2 composants (ce procédé s'est avéré aussi à même de préserver les matériaux friables remplissant les fissures dans la zone de cisaillement). Les critères les plus importants considérés pour la résine ont été la viscosité, la densité, le temps de polymérisation et la constance du volume durant la polymérisation, les propriétés de mouillage des surfaces humides dans les pores, la capacité de mélange homogène avec divers traceurs et une adsorption limitée des radioéléments.

Les propriétés physiques de la résine ont été déterminées par les fabricants, tandis que les propriétés d'imprégnation ont été étudiées en laboratoire sur des roches broyées en milieu humide (marnes du Valanginien), et ensuite sur des matériaux de remplissage de la zone de cisaillement investiguée. L'humidification des pores a été stimulée par l'injection d'isopropanol avant l'injection de résine (en fait, l'eau des pores a été remplacée par de l'isopropanol). Afin d'optimiser le système d'injection, une série d'essais a été faite en laboratoire et sur le terrain au LSG, à petite échelle. On a examiné différents aspects du système, tels que la pression d'injection appliquée, la méthode d'injection de l'isopropanol et le meilleur moyen de contrôler la proportion de résine et de durcisseur dans le mélange. Ces essais ont révélé une imprégnation des pores satisfaisante, la résine imprégnant en profondeur dans la roche les fractures ouvertes et les matériaux de remplissage des fissures. Ceci a permis de mener un essai in situ à plus grande échelle, sur des distances significatives pour l'expérience finale, et de tester la méthodologie de surforage subséquente. Les essais de surforage ont indiqué que seule un carotteur à triple tube pouvait garantir une récupération complète des carottes, et que le surforage dans le plan de la zone de cisaillement était de loin préférable au surforage perpendiculaire à cette zone.

En plus d'une immobilisation physique de la zone de cisaillement, la résine doit aussi ne pas modifier la distribution existante des radioéléments dans la roche. A cet effet, une séquence d'essais d'adsorption a été effectuée sur une série de résines. Des essais standard d'adsorption ont été menés sur des échantillons de roche imprégnés de résine et d'eau souterraine de la zone de cisaillement additionnée de radioéléments, pour étudier la compétition potentielle entre la résine et la granodiorite. Dans le même but, mais pour approcher plus précisément les conditions prévalant in situ durant l'expérience, des échantillons de roche additionnés de radioéléments ont ensuite été plongés dans la résine epoxy. Ces expériences ont montré clairement que l'imprégnation de résine n'influencera pas de manière significative la distribution des radioéléments dans la roche.

---

<sup>3</sup> The Japan Nuclear Cycle Development Institute (autrefois PNC, Power Reactor and Nuclear Fuel Development Corporation).

L'évaluation des techniques analytiques et radiochimiques de surface pour l'analyse des carottes s'est concentrée sur deux techniques de spectrométrie, à savoir SIMS (secondary ion mass spectrometry) et LAM-ICP-MS (laser ablation microprobe – inductively coupled plasma – mass spectrometry). Les études ont été faites sur une série d'échantillons de la zone de cisaillement investiguée, dans le but d'évaluer l'influence de la rugosité des surfaces, des exigences de neutralisation de charge des échantillons et du dégazage d'échantillons imprégnés. La technique SIMS a permis l'obtention de distributions des éléments à partir des grains minéraux, tandis que les mesures avec la technique LAM-ICP-MS ont montré la nécessité d'une investigation préalable avec les techniques SEM (secondary electron microscopy) et BSEM (back-scattered electron microscopy). Une analyse additionnelle d'échantillons au moyen de la technique EMPA (electron microprobe analysis) a montré que cette technique ne donne des résultats acceptables que sur les surfaces de granodiorite. Sur les remplissages synthétiques et naturels de fissures, une fluctuation importante du faisceau a rendu l'analyse ponctuelle impossible. L'analyse quantitative montre que les minéraux ont une composition simple pour la plupart, avec une variation faible à l'intérieur d'un échantillon, et représentent un bon standard interne pour les études d'ablation au laser.

Enfin, en raison de dommages possibles aux carottes durant le prélèvement d'échantillons, on a décidé d'évaluer la possibilité d'investiguer les structures de la zone de cisaillement (distribution des conduits et des pores, etc) sur les carottes par télédétection. Diverses techniques ont été utilisées, dont la tomographie PET (positron emission tomography) et la micro-résistivité MR (micro resistivity). La technique PET s'est avérée peu pratique à cause des limitations dans la taille de l'échantillon et des très longues durées de comptage. De plus, il fallait des activités assez élevées pour obtenir une bonne définition des images. Néanmoins, on a jugé que la technique PET avait un bon potentiel pour des images en temps réel du transport de radioéléments à travers les carottes au laboratoire, et que des investigations plus poussées seraient porteuses. La technique MR s'est avérée également prometteuse, mais le manque total d'informations de base sur les applications MR aux roches cristallines signifie qu'il aurait fallu consentir à un important programme de recherche et développement. Comme un tel programme ne peut entrer dans le cadre du projet EP, on a décidé de renoncer à la technique MR.

La présente phase de travail du projet EP a montré que l'expérience in situ finale, à pleine échelle, a de bonnes chances de se dérouler avec succès en utilisant des techniques adaptées aux conditions in situ de la zone de cisaillement investiguée (l'expérience finale est décrite dans MÖRI et al. 2003a). En outre, quelques unes des techniques développées ont été depuis appliquées au site expérimental de Kamaishi du JNC dans le nord-est du Japon, et au site d'Äspö de la SKB dans le sud de la Suède.

## List of Contents

Summary .....	I
Zusammenfassung.....	III
Résumé .....	V
List of Contents .....	VII
List of Tables .....	X
List of Figures .....	XI
List of Authors .....	XIII
<b>1 Introduction .....</b>	<b>1</b>
<b>2 Shear zone isolation methodology .....</b>	<b>5</b>
2.1 Choice of immobilisation technique.....	5
2.2 Laboratory scale resin impregnation of sheared rock.....	7
2.2.1 Selection of resin: results and conclusions of the first stage .....	9
2.3 Further resin development work.....	10
2.3.1 Results from the second stage .....	13
2.3.2 Evaluation of injection pressures.....	15
2.3.3 Epoxy resin injections using isopropanol.....	16
2.3.4 Additional resin characterisation .....	18
2.4 <i>In situ</i> experiments .....	21
2.4.1 Planned procedure .....	21
2.4.2 Injection test in shear zone AU138.....	21
2.4.3 Transmissivities in shear zones AU138 and AU126 .....	22
2.4.4 Impregnation in shear zone AU126.....	23
2.4.5 Rock fabric investigations of shear zone AU126 .....	25
2.4.6 Conclusions and future procedures.....	26
2.5 Field-scale resin impregnation dipole test.....	26
2.5.1 Setting up the flowfield .....	27
2.5.2 Isopropanol injection.....	28
2.5.3 Resin injection.....	31
2.5.4 Resin injection into borehole BOEX 95.003 (dipole flowfield).....	32
2.5.5 Overcoring shear zone AU126 .....	33
2.5.6 Conclusions .....	36

<b>3</b>	<b>Radionuclide sorption effects</b> .....	37
3.1	Evaluation of the sorption properties of resins .....	37
3.1.1	Methodology.....	37
3.1.2	Results and Discussion .....	38
3.1.3	Conclusions .....	40
3.2	Desorption of radionuclides by propan-2-ol.....	40
3.2.1	Methodology.....	40
3.2.2	Results and discussion.....	41
3.2.3	Conclusions .....	42
3.3	Sorption of tracers onto experimental equipment.....	42
3.3.1	Methodology.....	42
3.3.2	Results and discussion.....	43
3.3.3	Conclusions .....	44
3.4	Effect of sorption kinetics .....	45
3.4.1	Methodology.....	45
3.4.2	Results and discussion.....	46
3.4.3	Conclusions .....	50
<b>4</b>	<b>Assessment of analytical techniques</b> .....	51
4.1	SIMS analysis of Grimsel rock samples.....	51
4.1.1	Samples .....	53
4.1.2	Results and discussion.....	53
4.1.3	Conclusions .....	54
4.2	Evaluation of LAM-ICP-MS analysis of doped rock samples .....	55
4.2.1	Samples .....	55
4.2.2	Petrographical characterisation .....	56
4.2.3	Electron microprobe characterisation.....	58
4.2.3.1	Microchemical X-ray mapping.....	58
4.2.3.2	Results of microchemical X-ray mapping .....	59
4.2.3.3	Results of quantitative electron probe point analysis .....	60
4.2.4	LAM-ICP-MS analysis.....	61
4.2.4.1	Results of LAM-ICP-MS study.....	62
4.2.5	Discussion and conclusions .....	65
4.3	Feasibility of the use of PET (Positron Emission Tomography) to determine porosity and image fractures in granodiorite .....	67
4.3.1	Results and Discussion .....	69

4.3.2	Conclusions .....	71
4.4	Feasibility of the use of micro-resistivity core imaging to determine connected porosity in granodiorite .....	71
4.4.1	Micro-resistivity core imaging .....	72
4.4.1.1	Practical micro-resistivity core imaging.....	75
4.4.2	Conclusions .....	75
<b>5</b>	<b>Conclusions</b> .....	<b>77</b>
<b>6</b>	<b>Acknowledgments</b> .....	<b>79</b>
<b>7</b>	<b>References</b> .....	<b>81</b>
<b>Appendix A: Sample production and doping</b> .....		<b>A-1</b>
<b>Appendix B: Trial evaluation of LAM-ICP-MS analysis of doped rock samples from the GTS</b> .....		<b>A-2</b>
B.1	Petrographic characterisation .....	A-2
B.1.1	General .....	A-2
B.1.2	Scanning electron microscopy.....	A-2
B.2	Electron microprobe characterisation.....	A-3
B.2.1	Methodology.....	A-3
B.2.1.1	Microchemical X-ray mapping.....	A-3
B.2.1.2	Quantitative point analysis .....	A-4
B.3	Laser ablation microprobe – inductively coupled plasma – mass spectrometry (LAM-ICP-MS) analysis .....	A-4
B.3.1	Instrumentation.....	A-4
<b>Appendix C: Determination of the radiation dose and required activity</b> .....		<b>A-17</b>
C.1	Introduction .....	A-17

## List of Tables

Tab. 2.1:	Selected physical properties of acrylic and epoxy resins used for laboratory experiments.....	8
Tab. 2.2:	Selected physical properties of epoxy resins and results of test impregnations of synthetic fault gouges with these resins .....	11
Tab. 2.3:	Dynamic viscosity and density of water and isopropanol at 15 and 20 °C.....	17
Tab. 2.4:	Resin/hardener-mixing ratios for five selected samples taken from a synthetic fracture impregnated with resin No. 5 (with a pre-injection of isopropanol) .....	17
Tab. 2.5:	Results of further laboratory characterisation of epoxy and acrylic resins.....	19
Tab. 2.6:	Estimated transmissivities for shear zones AU138 and AU126 .....	23
Tab. 2.7:	Volumes of resin injected in the dipole resin injection test.....	32
Tab. 3.1:	Results of the epoxy resin (+ granodiorite) reservoir depletion experiments.....	39
Tab. 3.2:	Results of the propan-2-ol desorption experiments with 3 rock types.....	41
Tab. 3.3:	$K_a$ [ $\text{cm}^3 \text{cm}^{-2}$ ] for eight radionuclides on various materials ( $\pm 2 \sigma$ , based on the statistics of analysis alone) .....	44
Tab. 3.4:	$K_d$ [ $\text{cm}^3 \text{g}^{-1}$ ] with time for six radionuclides in contact with crushed mylonite (duplicate A and B experiments for alpha and gamma-emitters) .....	46
Tab. 4.1:	Tube dimensions, porosity, activities .....	68
Tab. 4.2:	NEC rate and measuring time in hours as function of granodiorite core diameter in pencil beam model.....	70
Tab. B.1:	LAM-ICP-MS results on NIST611 glass reference material.....	A-6
Tab. B.2:	LAM-ICP-MS results on NIST611 glass reference material.....	A-7
Tab. B.3:	LAM-ICP-MS results on samples spiked with $^{99}\text{Tc}$ .....	A-8
Tab. B.4:	LAM-ICP-MS results on samples spiked with $^{237}\text{Np}$ .....	A-9
Tab. B.5:	LAM-ICP-MS results on samples spiked with $^{233}\text{U}$ .....	A-10
Tab. B.6:	LAM-ICP-MS results on samples spiked with $^{242}\text{Pu}$ .....	A-11
Tab. B.7:	LAM-ICP-MS results on samples spiked with several elements.....	A-12
Tab. B.8:	LAM-ICP-MS results on samples spiked with Eu.....	A-13
Tab. B.9:	LAM-ICP-MS results on samples spiked with Mo .....	A-14
Tab. B.10:	LAM-ICP-MS results on samples spiked with Sn.....	A-15
Tab. B.11:	LAM-ICP-MS results on samples spiked with Se.....	A-16

## List of Figures

Fig. 2.1:	Steps in the development of the resin impregnation technique .....	6
Fig. 2.2:	Schematic representation of the synthetic fault gouge in the granodiorite core (a), check of structural integrity: top and side view of the glass markers distributed in a regular pattern in the synthetic fracture (b), top and side view of the three glass marker layers distributed regularly through the core perpendicular to the flow direction (c) .....	12
Fig. 2.3:	Results of impregnation of the synthetic fault gouge with the low-viscosity resin No. 5 under GTS conditions and 7 bar pressure showing three artificial fault gouge bands, cut surface of core (above), detail of cut surface (below); note the flecked pattern representing heterogeneous resin quality .....	14
Fig. 2.4:	Incremental changes of viscosity of Sikadur 52 and Resin No. 5 with time after mixing of resin and hardener .....	20
Fig. 2.5:	Incremental changes of tensile strength (fracture point) of Sikadur 52 and Resin No. 5 with time after mixing of resin and hardener .....	20
Fig. 2.6:	Concept for <i>in situ</i> injection .....	22
Fig. 2.7:	Test adaptor .....	24
Fig. 2.8:	Estimation of transmissivity from hydrotest 4 in AU138 using the straight-line method .....	25
Fig. 2.9:	Mechanical double packer system .....	28
Fig. 2.10:	Schematic representation of the experimental dipole (BOEX 95.003 to BOEX 94.007) and water injection .....	29
Fig. 2.11:	Schematic representation of the experimental dipole (BOEX 95.003 to BOEX 94.007) and isopropanol injection .....	29
Fig. 2.12:	Schematic representation of the experimental dipole (BOEX 95.003 to BOEX 94.007) and isopropanol extraction from injection borehole BOEX 95.003 .....	30
Fig. 2.13:	Schematic representation of the experimental dipole (BOEX 95.003 to BOEX 94.007) and resin injection in borehole BOEX 95.003 .....	30
Fig. 2.14:	Sketch of the DOPAG mixing pump ECONO-MIX D .....	31
Fig. 2.15:	Overcoring parallel to the plane of the shear zone AU126 (view to the South), diameter of the boreholes is 131 mm, scale 1 : 50 .....	33
Fig. 2.16:	Vertical section in the XZ plane of the injection and extraction boreholes: points of intersection of overcoring boreholes parallel to the plane of the shear zone AU126, diameter of the boreholes is 131 mm, scale 1 : 10 .....	34
Fig. 3.1:	Technetium sorption kinetics .....	47
Fig. 3.2:	Cobalt sorption kinetics .....	47
Fig. 3.3:	Uranium sorption kinetics .....	48
Fig. 3.4:	Europium sorption kinetics .....	48
Fig. 3.5:	Neptunium sorption kinetics .....	49

Fig. 3.6:	Selenium sorption kinetics.....	49
Fig. 4.1:	Overview of the analytical techniques tested within the project .....	52
Fig. 4.2:	X-ray maps for granodiorite sample Eu4G6, area 'a' – (a) BSEM, (b) Si, (c) Na, (d) K.....	60
Fig. 4.3:	TRA scans for masses <sup>237</sup> Np (top), <sup>24</sup> Mg (middle) and <sup>57</sup> Fe (bottom) during LAM- ICP-MS analysis of K-feldspar in granodiorite sample Np4G8.....	64
Fig. 4.4:	Diagrams of experimental set-up used in the numerical simulations .....	74
Fig. C.1:	Approximate layout of the rock core .....	A-17

## List of Authors

AEAT, Harwell, UK:

*J.A. Berry, M. Cowper, G.M.N. Baston, M. Brownsword and P. Oliver*

BGS (British Geological Survey), Keyworth, UK:

*M.T. Styles, A.E. Milodowski, S.R. Cheney, D.J. Bland, M.R. Gillespie, P.D. Jackson, R.C. Flint and J.J. Ball*

Brown Ltd., Macclesfield, UK:

*A. Brown*

Ecoengineers Pty Ltd., Helensburgh, Australia:

*S.A. Short (formerly PSI)*

Geotechnisches Institut, Berne, Switzerland:

*P. Bossart*

Geotechnisches Institut, Solothurn, Switzerland:

*H. Dollinger*

Rock-Water Interaction, Institute of Geology, University of Berne, Switzerland:

*M. Mazurek*

JNC (Japan Nuclear Cycle Development Institute), Tono Geoscience Centre, Gifu, Japan:

*K. Ota and T. Ando*

Nagra, Wetingen, Switzerland:

*W.R. Alexander (formerly University of Berne) and B. Frieg*

Neall Consulting, Kendall, UK:

*F.B. Neall*

PSI (Paul Scherrer Institute), Villigen, Switzerland:

*R.P. Maguire, J.H. Missimer, K.L. Leendars and C. Degueldre*

SIKA AG, Zürich, Switzerland:

*M. Meier*

Solexperts, Schwerzenbach, Switzerland:

*Ch. Bühler*



# 1 Introduction

*W.R. Alexander and F.B. Neall*

The Swiss National Co-operative for the Disposal of Radioactive Waste (Nagra) has, since 1983, undertaken a programme of hydrogeological and geochemical experiments at the Grimsel Test Site (GTS) aimed at developing and evaluating techniques and models relevant for future radioactive waste repository investigations (KICKMAIER et al. 2003). Field work has been complemented by a programme of hydraulic, geochemical and solute transport modelling, along with supporting laboratory studies.

A component of this programme was designed to study the transport of sorbing and non-sorbing radionuclide species in an artificial flowfield through fractured Grimsel Granodiorite host rock. The Nagra/JNC (Japan Nuclear Cycle Development Institute) co-funded Grimsel Migration Experiment (MI) was a multi-disciplinary study aimed at testing models of solute transport in fractured media, determining the degree to which laboratory results could be extrapolated to field conditions and developing the methodology for the characterisation of potential repository sites. Results from this stage of the experiment are documented in MCKINLEY et al. (1988), ALEXANDER et al. (1992), FRICK et al. (1992), SMITH et al. (2001a and b) and ALEXANDER et al. (2003b).

At present, studies such as MI produce data for the overall flow system 'seen' by the radionuclides. These data are then modelled to produce a set of 'best fit' bulk or average values for the retardation parameters, such as rock/water distribution coefficient, flow-wetted surface area and matrix diffusion depth, by comparing calculated model curves with the experimental breakthrough curves. However, the model values obtained may not be unique, other models and data may provide equally good fits. In addition, from this process, no detailed information is obtained about where the retardation actually takes place. Thus it is very difficult to extrapolate from one site, or flow system, to another where properties are different. This is a key issue as, in practice, the geosphere around a radioactive waste repository will not be exhaustively explored, due to the necessity to maintain favourable characteristics in as unperturbed a state as possible. Hence, it is essential that extrapolations from nearby or similar sites, where such restrictions do not apply, can be justified by a thorough understanding of the factors influencing radionuclide transport.

As part of this strategy, Nagra proposed a further experiment – the Excavation Project (EP) – involving the injection of a "cocktail" of important safety-relevant tracers into the MI shear zone which will then be excavated. A mixture of radioactive ( $^{234}\text{U}$ ,  $^{235}\text{U}$ ,  $^{238}\text{U}$ ,  $^{99}\text{Tc}$ ,  $^{75}\text{Se}$ ,  $^{113}\text{Sn}$ ,  $^{60}\text{Co}$ ,  $^{152}\text{Eu}$  and  $^{237}\text{Np}$ ) and non-radioactive tracers (uranine, molybdenum) is injected in a controlled manner into the groundwater flowing through the fracture zone. This is facilitated by using a "dipole flow system" created by intersecting the fracture zone with two boreholes (an injection well and an extraction well) with a spacing of about 2 m, and the experiment is conducted so as to constrain the flow between the two boreholes (see SMITH et al. 2001a for details).

After the tracer test has been completed, the shear zone is immobilised by resin injection, the complete dipole system is extracted by overcoring the shear zone with a triple barrel corer and the distribution of tracer elements within the flowfield determined by detailed petrographical and radiochemical analyses.

Several potential methods of immobilising the MI shear zone prior to excavation were considered in Phase I of EP (see ALEXANDER & KAWAMURA 1992). However, due to the need to preserve both the chemistry and the structure of the experimental shear zone<sup>4</sup> during the subsequent excavation, immobilisation by cement grout injection and by freezing of the pore-water were rejected in favour of resin injection. In the case of cement grout, chemical perturbations would be expected due to the reactivity of the high pH grout. With the freezing technique, the expansion of the water on freezing was expected to disrupt structures, especially of the fine-grained, friable fracture-filling material (fault gouge). In contrast, it was considered that the physical properties of the resin could be adjusted to obtain good penetration of the fine structure of the fault gouge at ambient temperatures without significant disruption or chemical perturbation. Once the basic feasibility of EP had been demonstrated, Phase II of EP began. The aim here was to test the applicability of the major components of the experimental system, identify any problems and, where necessary, develop new techniques for use in the experiment. This was felt necessary as EP was to be a unique experiment: although similar experiments had been conducted in the laboratory or on rock cores (e.g. BISCHOFF et al. 1987), nothing of this scale or complexity had been conducted in the field.

It was recognised that a significant effort would be required to determine the optimum resin composition and range of injection conditions where no significant damage would be caused to the rock-water-radionuclide system. Furthermore, *in situ* experiments would also be required to obtain experience in the injection methodology as there could only be one attempt to inject into the MI shear zone, following the radionuclide injection.

Experimental work was also considered necessary to support the EP in other areas:

- To deal with potential problems arising from interaction of the resin with the radionuclides, thus changing the rock-groundwater radionuclide distribution. In addition, the resin injection technique developed in the experimental programme included the use of isopropanol as a wetting agent and resin sorption tests were expanded to include isopropanol, since radionuclides are known to extract into several similar solvents.
- To assess the sorption of the tracer radionuclides onto the injection equipment. Experience gained within MI suggested that significant sorption of several of the experimental radionuclides on parts of the injection apparatus was likely.
- To assess the effects of sorption kinetics (likely for some of the radionuclides to be injected) in the 1.7 m flowfield where residence times are a couple of hours for non-sorbing tracers and where first breakthrough occurs in 20 minutes. During the MI experiment, it was noted that, for some tracers, there was a definite kinetic hindrance to sorption. In particular, this was noted for Cs in both the laboratory and in the field (BRADBURY & BAEYENS 1992, SMITH et al. 2001b). Scoping experiments with Tc in the MI shear zone also indicated likely kinetic effects.
- To assess techniques which would allow definition of porosity, presence of channels, etc. non-destructively, as compared to traditional, destructive techniques such as thin section petrology. There were two reasons for this: first, it was initially thought that the material excavated from the MI shear zone might be too unstable to transport and thus an initial examination of the pore structure of the sample would have to be carried out immediately in

---

<sup>4</sup> The MI shear zone represents a low temperature and pressure re-activation of a mylonite (MEYER et al. 1989, BOSSART et al. 1991). The brittle re-activation has produced a very weak zone of interconnected fractures filled with a very fine grained fault gouge. Any immobilisation techniques must therefore be capable of not only not perturbing the system, but also of greatly increasing the strength and rigidity of the zone of interest so allowing successful full core recovery during overcoring (excavation).

the GTS tunnels. Second, it was felt worthwhile comparing non-destructive techniques with the standard (destructive) technique to assess any artefacts inherent to the latter method.

- To assess analytical techniques to determine the distribution of radiotracer elements (which will probably be present at very low concentrations) on mineral surfaces in contact with the groundwater. A series of pilot studies were required to investigate a variety of macroscopic and microscopic, petrographical and radioanalytical techniques that might be used to analyse the EP drillcores. These included optical petrography, scanning electron microscopy (SEM), backscattered scanning electron microscopy (BSEM), electron microprobe analysis (EMPA), X-ray micromapping techniques, secondary ion mass spectrometry (SIMS) and laser-ablation microprobe-inductively-coupled plasma mass spectrometry (LAMP-ICP-MS).

This report provides a record of Phase II of EP, tracing a path through the range of experimental techniques which were tested, leading to the basis on which the final choice of immobilisation methodology, radioanalytical techniques and mode of structural analysis was made. This report covers an intensive testing period of some two years and hence it is not possible to detail each incremental change to the designs examined (nor to explain every individual discussion behind the change), but an attempt has been made to note all major decisions which impacted on the final choice of methods, including the usual mistakes and blind alleys which are an inevitable feature of innovative work.



## 2 Shear zone isolation methodology

### 2.1 Choice of immobilisation technique

*K. Ota, F. Neall and W.R. Alexander*

As noted in the introduction, several aspects of the radionuclide retardation project require the immobilisation and recovery of the intact shear zone for further investigations in the laboratory. Immobilisation of the shear zone has proven to be one of the areas in the project where a particularly large degree of effort has had to be invested because the physical properties and structure of the experimental shear zone and the associated rock matrix play a key role in deciding on the methods to be used.

The shear zone is the product of low temperature reactivation of a pre-existing zone of weakness in the granodiorite: later (and still on-going) brittle deformation has produced a friable, structurally weak, rock zone consisting of the original granodiorite (1 – 2 % porosity) along with low porosity (0.1 %), highly oriented, mica-rich mylonite (the product of the original high pressure and temperature deformation) and fault gouge-filled fractures (MEYER et al. 1989, BOSSART et al. 1991). The fault gouge has a relatively high porosity of 10 to 30 % and the shear zone overall shows transmissivities in the order of  $2 \times 10^{-6} \text{ m}^2 \text{ s}^{-1}$  (FRICK et al. 1992, SMITH et al. 2001b).

In addition, laboratory work (BAEYENS & BRADBURY 1989, AKSOYOGLU et al. 1991) showed that the fault gouge, which is easily eroded unless treated very carefully, is the primary site of radionuclide retardation in the shear zone and thus must be preserved. The technique has also to take into account the highly inhomogeneous and friable nature of the shear zone and must further be able to enhance the structural integrity of the zone prior to excavation. Numerous attempts have been made to recover samples from the shear zone but, without some form of immobilisation, they have usually resulted in the destruction of the sample.

A further problem arises due to the fact that the granitic matrix which surrounds the mylonite has a porosity of around 1 – 2 % (OTA et al. 2003) but a low permeability of  $10^{-10}$  to  $10^{-12} \text{ m}^2 \text{ s}^{-1}$  (VOMVORIS & FRIEG 1992). It is therefore essential to find a material which can effectively penetrate the rock and immobilise it at depth without damaging the *in situ* pore structure as well as immobilising the fault gouge.

In the initial stages of the project, various alternative methods of rock immobilisation were reviewed, include freezing of pore water, resin impregnation and injection of cementitious grouts (Fig. 2.1). Although freezing works well in porous rocks such as sandstone, work performed in JNC's Kamaishi Test Site (KTS) in north-east Japan showed that freezing would probably cause considerable damage to the experimental shear zone (WATANABE et al. 1993) due to the well known increase of the porewater volume during the freezing of the water. This could involve disrupting the pore structure of the fine fault gouge and opening or extension of fractures. Grouts could penetrate the very fine-grained rock of interest in the GTS but would interact chemically with the groundwater and rock; this latter process is to be avoided at all costs in the shear zone as it may have the effect of remobilising the sorbed radionuclides. In the end, resin impregnation was the only technique that had the potential to satisfy all the various criteria described above.

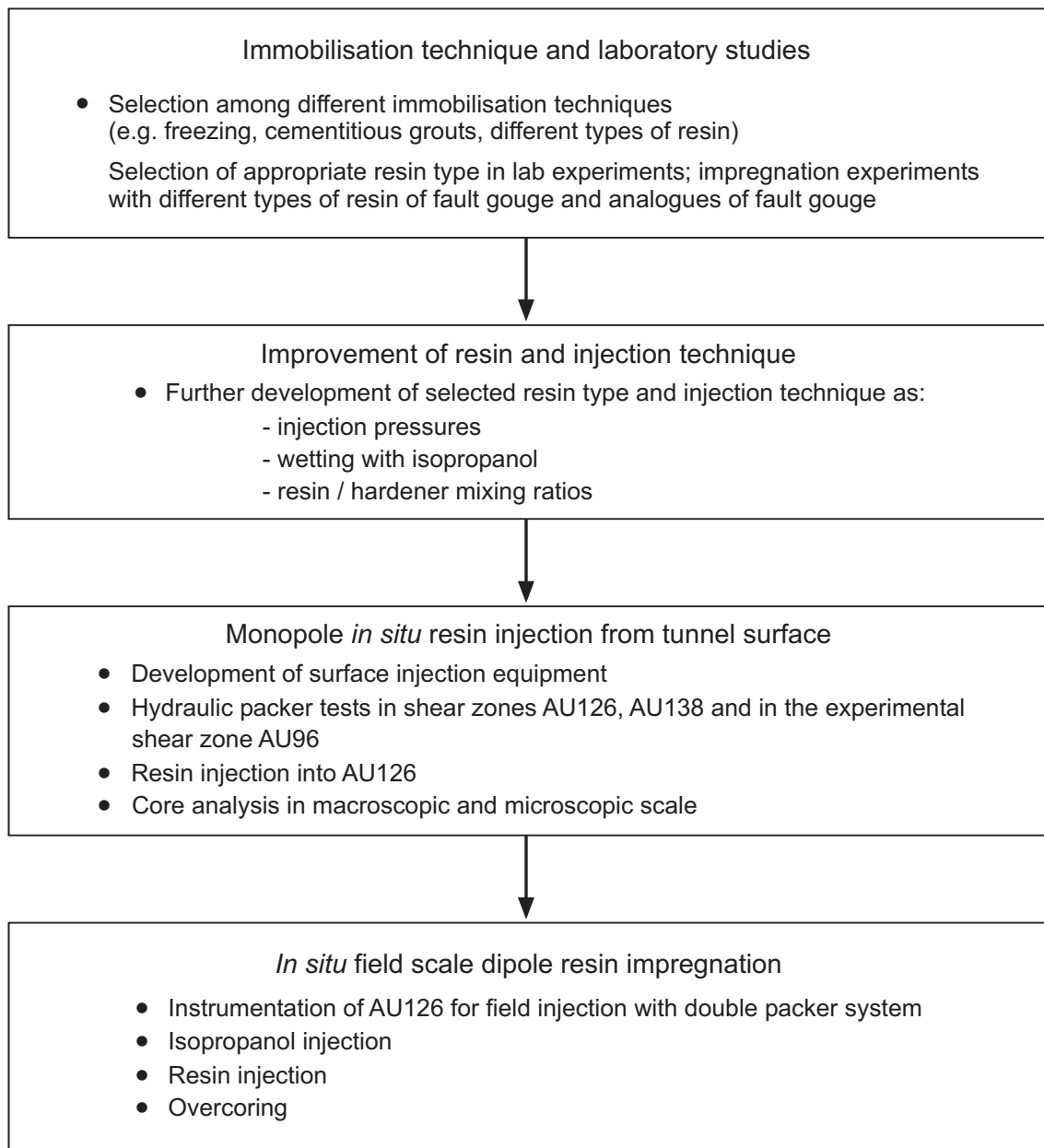


Fig. 2.1: Steps in the development of the resin impregnation technique

Although resin impregnation is a technique used routinely in geological laboratories to immobilise rock samples before sub-sampling, grinding and polishing, the requirements of its use in the shear zone were more stringent, especially with regard to chemical perturbation of the system, than is normally the case in these routine applications. Therefore, it was necessary to carry out a series of experiments to ensure that an appropriate resin was used and a predictable, satisfactory performance of the technique could be obtained.

## 2.2 Laboratory scale resin impregnation of sheared rock

*H. Dollinger, P. Bossart, Ch. Bühler and M. Mazurek*

Two types of resin (acrylic and epoxy) were investigated in the first stage of work. In liquid form, both of these resins can penetrate into a pore space and preserve the pore structures by means of polymerisation (hardening). Following polymerisation, the samples can be cored and sawn for further investigation. The following factors are of particular importance:

- 1) The suitability of acrylic and epoxy resins with respect to preserving the flowpath geometry. Weighing the advantages and disadvantages of their contrasting physical and chemical properties.
- 2) Injectability: The resin's viscosity must be low enough so that it can be easily injected into the shear zone (high pressures would erode the fault gouge).
- 3) Characterising an optimum resin in terms of physical properties (e.g. viscosity, gel time, stability, interaction with wet surfaces, etc.).
- 4) The structural quality of impregnated samples (assessed macroscopically using sawn samples and microscopically using thin sections).
- 5) The interaction of acrylic and epoxy resins with sorbing radionuclides.

In the construction industry, resins are usually used as sealants, for example by injection of resins into concrete dams or into the underlying rock formations. This is generally done by injecting two-component epoxy resins into boreholes under high pressure using special pumps. The function of the resin is to displace water and form a strong bond between materials on both sides of a crack or fracture. Widening of fractures during the injection phase is considered justifiable if this allows deeper penetration of the resin. However, in the case of the shear zone excavation project, somewhat different demands are placed on the performance of a resin. The resin has to be introduced with a minimum of perturbation and changes in the structures of the pore space are to be avoided wherever possible. The main aim is to preserve the flowpaths in the shear zone and to strengthen the entire rock mass for overcoring.

Since the requirements placed on a resin for the purposes of the excavation project are so different from those in conventional uses as sealants or in optical microscopy sample preparation, it was not possible to simply assume that available resins would be suitable. First, it was necessary to select the most suitable candidate from a number of similar resins with slightly differing physical properties. In order to ensure that the resins being investigated were exposed to similar test conditions, it was decided not to inject them directly into a shear zone at the GTS, since the geometry of the pore space in such shear zones varies from location to location, making intercomparisons difficult.

Different epoxy resins were made available by Ciba-Geigy AG (Basel, Switzerland), Sika AG (Zürich, Switzerland) and I-N Technical Lab (Osaka, Japan). An acrylic resin was provided by Rascor AG (Oberweningen, Switzerland). Tab. 2.1 summarises the physical properties (such as density, viscosity, gel time and pot-life) of the resins.

Tab. 2.1: Selected physical properties of acrylic and epoxy resins used for laboratory experiments

Resin	Density [g cm <sup>-3</sup> ]	Viscosity [mPa s]	Gel time and pot-life [min]
<i>Rascor AG</i> , Oberweningen Acrylic resin 1.1010/1	20 °C: approx. 1	20 °C: 13	approx. 180
<i>I-N Technical Lab</i> , Osaka, Japan EX 100 (epoxy resin)	20 °C: approx. 1	low (near water)	-
<i>Ciba-Geigy AG</i> , Basel Araldite PY 340-2 (epoxy resin) HZ 340 (hardener)	Epoxy resin at 25 °C: 1.19 Hardener at 25 °C: 1.04	Epoxy resin at 25 °C: 6000 – 8000 Hardener at 25 °C: 13000 – 23000 (dilute with H <sub>2</sub> O = lower viscosity)	at 20 °C: 120
Araldite BY 157 (epoxy resin) XHY 848 (hardener)	Epoxy resin at 25 °C: 1.16 Hardener at 25 °C: 1.01	Epoxy resin at 25 °C: 4200 – 5700 Hardener at 25 °C: 2500 – 5500	at 20 °C: 330
Araldite BY 158 (epoxy resin) XHY 848 (hardener)	Epoxy resin at 25 °C: 1.09 – 1.19 Hardener at 25 °C: 1.01	Epoxy resin at 25 °C: 280 – 360 Hardener at 25 °C: 2500 – 5500	-
<i>Sika AG</i> , Zürich Sikadur 53	Mixture: 20 °C = 2.0	Mixture: 20 °C = approx. 5800 10 °C = approx. 15000	1 kg resin at 20 °C: 50
Sikadur 52			
Comp. A = Sikadur 281 (epoxy)			
Comp. B = Sikadur 340 (hardener)	Mixture: 20 °C = 1.1	Mixture: 20 °C = 500 10 °C = 1000	at 20 °C: 20 at 10 °C: 55
Sikadur 52 (reference resin)			
Comp. A = Sikadur 281 (epoxy)			
Comp. B = Sikadur 341 (hardener)	Epoxy at 20 °C: 1.13 Hardener at 20 °C: 1.01	Mixture: 20 °C = approx. 200	approx. 120
Resin No. 2	approx. 1.1	Mixture: 20 °C = approx. 1700	approx. 120
Resin No. 3	approx. 1.1	Mixture: 20 °C = approx. 200	approx. 120
Resin No. 4	approx. 1.1	Mixture: 20 °C = approx. 1000	approx. 120

- = value not known

Initial tests involved immersing in resin a variety of air-dried or water-saturated samples, including partly mylonitised Grimsel granodiorite (from core BK 86.001) containing at least one section of non-cohesive fault gouge material and wet crushed Valanginian Marl (as an analogue for fault gouge material).

A second series of tests involved resin injection at laboratory ambient temperatures (approx. 27 °C) into split drill cores containing a layer of synthetic fault gouge to test the degree of impregnation of very fine-grained material. The synthetic fault gouge, as a wet paste, formed a layer between the two halves of a section of drillcore sawn longitudinally. The assembled 'sandwich' was kept together by use of a shrinkable tubing sleeve. These were then either immersed in resin or impregnated under pressure.

The synthetic fault gouges were used as insufficient natural material was available and it had the added advantage of being relatively uniform from one sample to the next. Due to disappointing results from the first test series, new epoxy resins (Resins No. 2, 3 and 4 in Tab. 2.1) were formulated (Sika AG, Zürich) and were included in these and later tests.

A further series of tests with these synthetic fault gouges was carried out in the GTS tunnels at lower ambient temperature of around 13 °C, more appropriate for gauging the viscosity and behaviour of the resins *in situ*.

### 2.2.1 Selection of resin: results and conclusions of the first stage

As shear zones are more or less water-saturated, mechanical preservation by means of resin impregnation will either have the effect of displacing water (which could have an associated transport of tracers) or water will partly be incorporated in the resin. In the latter case, there is displacement of water but to a much smaller extent.

The experiments showed that binding of water by hydrophilic resins (acrylic resins) is only temporary (as an emulsion) during the impregnation process. Subsequent evaporation of the pore-water results in a volume change leading to considerable shrinkage of the resin, which destroys the natural structures of the pore space.

Under atmospheric conditions, none of the hydrophobic resins (epoxy resins) tested impregnated the fine-grained fault gouge to a satisfactory extent. Sikadur 52 (epoxy resin Sikadur 281 and long pot-life hardener Sikadur 341) appeared to be the best of the epoxy resins tested. The physical properties of the epoxy resins change depending on ambient temperature. A particular advantage of Sikadur 52 is that wet (partially saturated) pore spaces can be impregnated and polymerisation proceeds without shrinkage. It was also found that Sikadur 52 can be mixed with the tracer fluoresceine<sup>5</sup> (fluorol yellow 088) without any problems.

Water-saturated pore spaces can only be completely impregnated with epoxy resins if the pore-water is displaced. Otherwise the water is trapped as inclusions in the resin (the implications of this to the *in situ* application of epoxy resins is discussed later).

The synthetic fault gouges did not appear to have altered significantly during the impregnation process. Locally, grain orientations due to rotation (long axis of the components parallel to the flow direction) were observed. Structural integrity before and after impregnation needed to be tested using appropriate experiments, particularly in cases where injection pressures > 2 bars had to be applied.

---

<sup>5</sup> Also known as uranine.

Properties of an ideal resin (at ambient temperature 13 °C) were found to be:

- Viscosity: 100 to 150 mPa s
- Density: 1.1 – 1.2 g cm<sup>-3</sup>
- Gel time: 5 – 10 hours
- Polymerisation time: 12 – 15 hours
- Hardening time: 1 – 2 days
- Good wetting of water-wet surfaces in the pore space
- Homogeneous mixing with a fluorescent tracer
- Weak sorption of radionuclides (e.g. <sup>235</sup>Np, <sup>134</sup>Cs).

### 2.3 Further resin development work

*H. Dollinger, K. Ota, Ch. Bühler, T. Ando, P. Bossart, M. Meier and S. Short*

The first stage defined the ideal resin for rock immobilisation and compared the properties of a series of different formulations of epoxy and acrylic resins. None, however, was found to meet these requirements due, in the case of the better performing epoxy resins, to high viscosity limiting impregnation of fine-grained fault gouge and the studies were extended to a further investigation of refined epoxy resin compositions.

Tab. 2.2 compares the physical properties and results of impregnation tests on the two new formulations, resins 5 and 6, and the best performing of the resins from the previous investigations (Sikadur 52 and resins No. 2 to 4). Initial tests were made using the same type of synthetic fault gouge in a sawn drillcore section as used in Section 2.2. However, the pressure used to impregnate the samples (carried out in the GTS tunnels at ambient temperatures, about 13 °C) was sufficiently high to disrupt the fault gouge. Therefore, in the second test series in which only the low-viscosity resins No. 5 and No. 6 were used, it was attempted to keep the injection pressures lower by making the synthetic fault gouge less dense and by more careful contraction of the shrinkable sleeve.

In order to ensure that the resin injections did not alter the structure of the fault gouges, an attempt was also made in this injection series to label the fault gouges with "markers" (Fig. 2.2b) of glass fragments with a grain diameter of 351 – 495 µm, corresponding to the mean grain diameter ( $d_{50}$ ) of the natural fault gouge. In the first step, small heaps of glass fragments (diameter around 3 mm, spacing 1 cm) were laid on each half of the split drillcores, wetted with a drop of water and placed in a freezer. Around 6 mm of synthetic fracture material was then placed on both core halves, smoothed out and frozen. A further "marker" layer was then placed on one frozen core half, the core halves were placed together and surrounded by the shrinkable sleeve.

Tab. 2.2: Selected physical properties of epoxy resins and results of test impregnations of synthetic fault gouges with these resins

Physical properties	Sikadur 52 (reference resin)	Resin No. 2	Resin No. 3	Resin No. 4	Resin No. 5	Resin No. 6
Density: Resin [g cm <sup>-3</sup> ] Hardener	1.125 0.987	(mixture ~1.1)	(mixture ~1.1)	(mixture ~1.1)	1.142 0.987	1.124 0.987
Viscosity: after [mPa s]	495 (13 °C) ~ 200 (20 °C) 713 (13 °C) 913 (13 °C)	~ 1700 (20 °C) - - - -	~ 200 (20 °C) - - - -	~ 1000 (20 °C) - - - -	83 (13 °C) 173 (13 °C) - 452 (13 °C) 781 (13 °C) -	86 (13 °C) 236 (13 °C) - 243 (13 °C) - 463 (13 °C)
Tensile strength: [MPa]	1.4 (13 °C) 7.9 (23 °C) 4.2 (13 °C) 18.0 (23 °C) 8.8 (13 °C) 22.3 (23 °C)	- - - - -	- - - - -	- - - - -	- 2.0 (23 °C) - 7.5 (23 °C) 2 (13 °C) 12.9 (23 °C) 4.9 (13 °C) - 14.6 (13 °C) -	- 1.5 (23 °C) - 5.2 (23 °C) 1.4 (13 °C) 8.8 (23 °C) 3.4 (13 °C) - 7.9 (13 °C) -
<b>Evaluation of resin injection based on study of drillcores (macroscopic) and the sections (microscopic)</b>						
Degree of filling of synthetic fracture at 13 °C (macroscopic)	very good	not tested	good	adequate to good	adequate to very good (contains unimpregnated areas)	adequate to good (contains relatively numerous unimpregnated areas)
Impregnation of near- fracture grain boundary and transgranular pores	frequent	rare	average	average	frequent	average to rare
Penetration depth of resin into rock surrounding fracture	max. 1.4 mm	max. 0.9 mm	max. 1.6 mm	max. 0.8 mm	max. 6.3 mm average 1.4 – 1.8 mm	max. 3.0 mm average 1.4 mm
Comments	at 13 °C incomplete filling of synthetic fracture	incomplete filling of synthetic fracture even at 27 °C	react with water which delays complete hardening	incomplete filling of synthetic fracture at 13 °C	chemically similar to Resin no. 1, very good results with prior injection of isopropanol	to achieve the low viscosity, some "foreign" chemical components were added to the resin

- = no measurement

As in the case of the previous injection series, resin No. 5 was initially injected with a flowrate of 10 mL min<sup>-1</sup>. As soon as the maximum permissible pressure of 5 bars<sup>6</sup> was reached, the flow was continually reduced, down to 0.2 mL min<sup>-1</sup>. The resin appeared in the overflow after around 1.5 hours.

The two injection tests with resin No. 6 were conducted with a flowrate of only 1 mL min<sup>-1</sup> from the outset. When the allowable maximum pressure of 5 bars was reached, the flow had to be reduced continuously, to 0.1 mL min<sup>-1</sup>. In both injection tests, resin No. 6 reached the overflow after approximately 70 minutes. If the fracture is saturated with a low flowrate, the resin can generally be injected at a lower pressure. Despite the lower flowrate, there does not appear to have been much delay in resin breakthrough. This information was taken into account when planning subsequent injection tests in the synthetic fault gouges and in the *in situ* experiments.

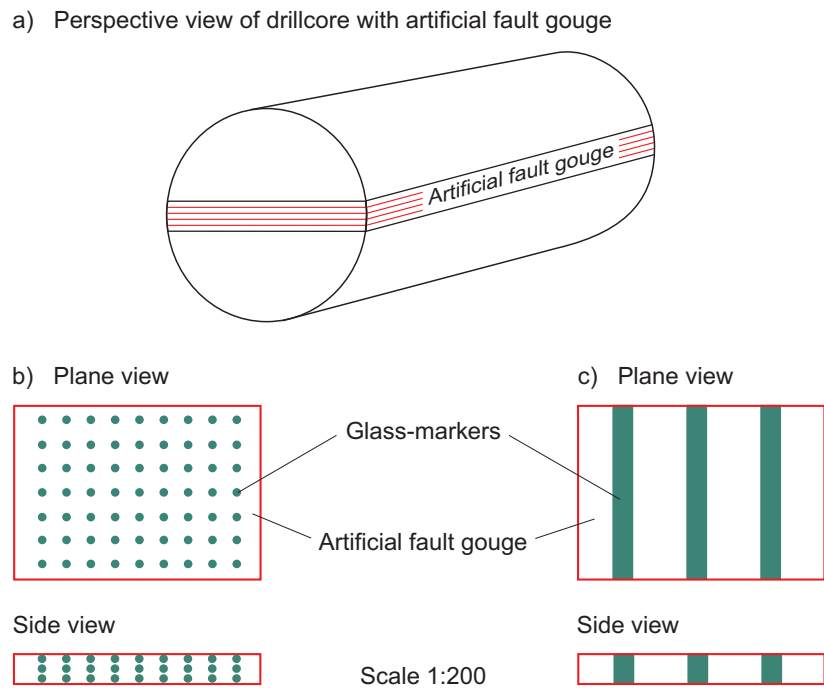


Fig. 2.2: Schematic representation of the synthetic fault gouge in the granodiorite core (a), check of structural integrity: top and side view of the glass markers distributed in a regular pattern in the synthetic fracture (b), top and side view of the three glass marker layers distributed regularly through the core perpendicular to the flow direction (c)

<sup>6</sup> Trial and error during the MI experiment indicated that injection pressures above 10 bars led to fault gouge erosion. As such, the tests were conducted at a maximum of 5 bars to include a safety margin.

### 2.3.1 Results from the second stage

The following macroscopic assessment was made of the drillcores used in the injection series described above:

- The pressures used in the first injection series for the low-viscosity resins No. 5 and No. 6 were clearly too high. Injection pressures of up to 10 bars resulted in displacement of the fracture material.

Check of structural integrity. In the synthetic fracture, three regularly spaced coloured glass markers were introduced perpendicular to the flow direction in layers through the core.

With the given resin injection pressures of 4, 7, 11 and 13 bars, macroscopic investigations of sawn-up core half 5-3 (Fig. 2.3) revealed no displacement of the fracture material<sup>7</sup>. However, a flecked pattern with well-hardened and more porous, relatively soft zones is clearly visible, representing a heterogeneity in the quality of the resin.

Since the physical properties of resins No. 5 and No. 6, such as viscosity and density, were very similar to those of water, the resins did not succeed in completely displacing the water. The synthetic fractures contained small (but sometimes larger) unimpregnated areas. Macroscopically, these areas generally appear as empty bubbles because the unimpregnated fracture material is flushed out when the cores are sawn in half. This phenomenon occurred more frequently for resin No. 6 than for resin No. 5:

- In the fractures impregnated with resins No. 5 and No. 6, there is a pattern of darker, denser, hardened zones adjacent to lighter, porous and relatively soft zones (Fig. 2.3).
- With ambient temperatures of around 13 °C, it was necessary to wait around 3 weeks in the case of cores impregnated with resin No. 5, and 4 weeks with resin No. 6, before the cores could be subjected to further investigation (e.g. minimum strengths for producing thin sections).

The following microscopic evaluation was made using thin sections:

- Impregnation of near-fracture grain boundary and transgranular pores in the Grimsel granodiorite is frequent in the cores injected with resin No. 5 and average to rare for those injected with resin No. 6.
- The two low-viscosity resins penetrated an average of 1.4 to 1.8 mm and a maximum of 6.3 mm (resin No. 5) and 3.0 mm (resin No. 6) into the rock surrounding the synthetic fracture.

Since the injected fracture material contained relatively numerous unimpregnated areas, resin No. 6 was excluded from subsequent experiments, even though it has a lower viscosity and a longer polymerisation time than resins 5 and 1. It appears that several additives in resin No. 6 were unstable and that, depending on the injection conditions, reactions which are very difficult to foresee may occur. Resin No. 5, on the other hand, has a chemical composition very similar to that of resin No. 1 (the reference resin); in this case, very satisfactory impregnation of synthetic fractures was achieved at temperatures around 20 °C.

---

<sup>7</sup> At pressures > 10 bars, however, some of the pressure was lost through the incompletely sealed silicon rubber sleeves via the water-filled space between the core and the steel tube of the impregnation cylinder.

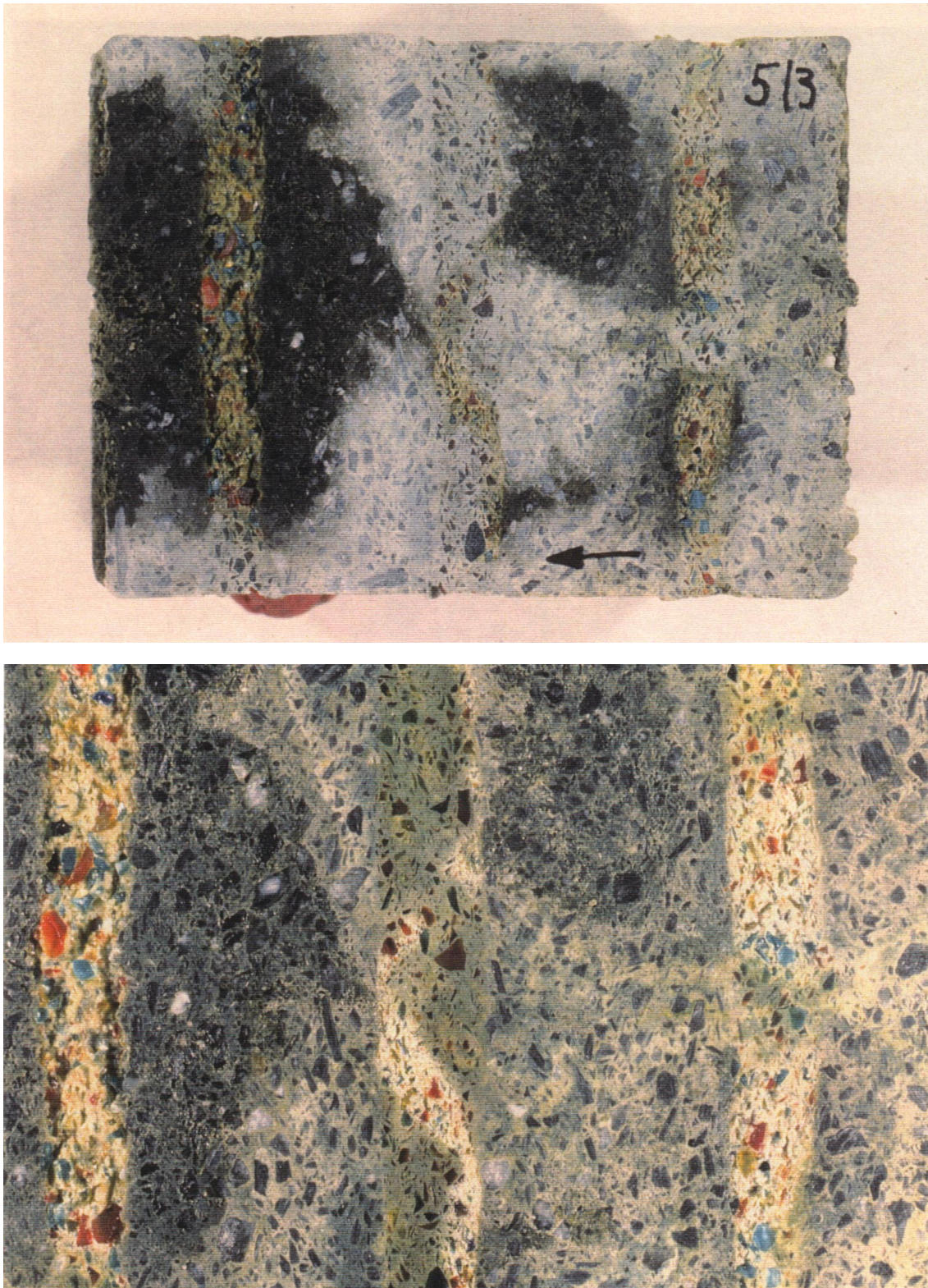


Fig. 2.3: Results of impregnation of the synthetic fault gouge with the low-viscosity resin No. 5 under GTS conditions and 7 bar pressure showing three artificial fault gouge bands, cut surface of core (above), detail of cut surface (below); note the flecked pattern representing heterogeneous resin quality

### 2.3.2 Evaluation of injection pressures

It had been noted in previous tests that injection pressures of up to 10 bars led, in some cases, to displacement of the fracture material. Therefore, it was decided to check the structural integrity of the synthetic fracture at injection pressures of 4, 6 and 8 bars. These experiments were conducted with the more suitable of the two low-viscosity resins, namely resin No. 5.

Introducing the markers into the synthetic fracture in three regular layers (Fig. 2.2c) was beset with difficulties. As was realised subsequently, it is impossible to visualise any displacements of the fracture material satisfactorily on either a macroscopic or microscopic scale. In addition, the procedure for introducing the glass marker into the synthetic fracture had to be changed in order to avoid any possible effects of freezing. In this further series of injections, the coloured glass marker was introduced in three layers distributed regularly through the core perpendicular to the flow direction (Fig. 2.2c). In a multi-step procedure, the glass and the synthetic fault gouge were filled layerwise between the two upright core halves (held apart at a distance of 10 mm) which were then pressed together. The synthetic fracture material was wetted with a small amount of water but the glass was introduced in a dry condition.

In the four injections in this series conducted with resin No. 5, the maximum permissible resin injection pressures were restricted to 4, 7, 11 and 13 bars, respectively.

A macroscopic analysis of the sawn-apart drillcores revealed the following:

- Even at injection pressures of 11 and 13 bars, no clear displacement of the fracture material could be detected. However, some pressure applied in these injection tests was lost through the water-filled space between the core and the steel wall of the impregnation cylinder because the seal provided by the silicon rubber sleeves was not completely intact.
- Even in the case of these synthetic fractures impregnated with resin No. 5, it was possible to detect a variable pattern of zones which had hardened well and zones which were still relatively soft and more porous. It was presumed that, in the zones which were more porous and still relatively soft, the optimum resin/hardener mixing ratio of 100 : 51 had been altered in such a way that it was no longer possible for the epoxy resin to harden completely. Sika AG were able to confirm this on a series of samples taken from a synthetic fracture impregnated at 13 bars.
- On a microscopic scale, no displacement of the marker in the synthetic fracture (core 5-4) impregnated under a maximum pressure of 4 bars could be detected.

All the investigations have shown that resin No. 5 is the more suitable of the two low-viscosity resins used. However, its behaviour during injection, when the resin/hardener mixing ratio may be altered in such a way that complete hardening can no longer be ensured, needed further investigation as it had not been observed with other, even very similar, resins. Consequently, a series of tests in which different proportions of resin No. 1 were added to resin No. 5 was carried out to assess the most appropriate ratio. The tests used a maximum injection pressure of 5 bars and resin No. 5 : resin No. 1 mixing proportions of 100 : 0, 90 : 10, 80 : 20, 70 : 30 and 50 : 50. The best results in terms of completeness of impregnation were obtained with a mixture of 70 % resin No. 5 and 30 % resin No. 1, but even so variable hardening was still observed in this and all the other trials.

### 2.3.3 Epoxy resin injections using isopropanol

As noted above, some of the synthetic fractures injected with the low-viscosity resins No. 5 and No. 6 showed small, and sometimes relatively large, areas which were not impregnated. The physical properties of the resins used are very similar to those of water and it would appear that the low density and, to a lesser extent, the relatively low viscosity of the resins have an adverse effect on their ability to wet the mineral surfaces and to expel porewater.

In order to avoid this effect, an attempt was made to exchange the porewater with a solvent which has a lower density than water prior to resin injection (a method long established in the soil sciences). The density difference compared with the injected resin will then be greater and more complete impregnation of the pores should be possible. At the same time, the solvent takes over the function of a solubiliser which reduces the surface tension between the water film, which adheres to the fracture material, and the somewhat hydrophobic resin. To achieve better impregnation with resin No. 5, once the pore space had been saturated, the water was replaced with isopropanol.

Injection of water was followed by injection of isopropanol (both with a flowrate of 1 mL min<sup>-1</sup>) and the pressure rose rapidly from around 3 bars to around 9 bars before a plateau was reached. This can be explained by reference to the general Darcy equation. Assuming the pumping rate and the parameters which characterise the medium through which flow occurs are the same for both fluids:

$$q = - \frac{c d^2 \rho g}{\mu} \frac{dh}{dl} \quad (\text{Eq. 2.1})$$

where:

- q : Specific flow [m s<sup>-1</sup>]
- c : Geometry constant [-]
- d : Diameter of synthetic fracture [m]
- ρ : Density [kg m<sup>-3</sup>]
- μ : Dynamic viscosity [kg (m s)<sup>-1</sup>]
- $\frac{dh}{dl}$  : Hydraulic gradient along the core [-]

If the specific flow for water and isopropanol remains the same throughout the injection phase,

i.e.  $\frac{q_{\text{Water}}}{q_{\text{Isopropanol}}} = 1$ , the following relationship can be derived from Equation (2.1):

$$\frac{dh_{\text{Isopropanol}}}{dh_{\text{Water}}} = \frac{\rho_{\text{Water}}}{\rho_{\text{Isopropanol}}} \cdot \frac{\mu_{\text{Isopropanol}}}{\mu_{\text{Water}}} \quad (\text{Eq. 2.2})$$

If the values in Tab. 2.3 are applied, then at 20 °C

$$dh_{\text{Isopropanol}} = 3.08 dh_{\text{Water}} \quad (\text{Eq. 2.3})$$

As observed, the pressure on injection of isopropanol is therefore around three times higher than in the case of water injection.

Macroscopic analysis of the sawn drillcores revealed the following:

- The synthetic fracture injected with resin No. 1 could not be completely filled with the given maximum pressure of 5 to 5.5 bars. As already observed, the viscosity of resin No. 1 at ambient temperatures of 13 – 14 °C is too high to achieve complete impregnation, although the resin would actually fulfil all the other test criteria.
- Resin No. 5 impregnated the synthetic fractures of both cores completely and it hardened fully with the exception of a few small areas.
- Microscopic analyses of thin sections gave the following results for resin injection using isopropanol:
  - Usable thin sections could be produced from all three impregnated synthetic fractures; their quality was also acceptable to good under UV light. The observations made in previous injection tests regarding impregnation of grain boundary and transgranular pores and penetration depth of the resin into the rock surrounding the synthetic fractures were confirmed.

Tab. 2.3: Dynamic viscosity and density of water and isopropanol at 15 and 20 °C

Parameter	Water		Isopropanol		Reference
	15 °C	20 °C	15 °C	20 °C	
Temperature	15 °C	20 °C	15 °C	20 °C	
Viscosity $\mu$ [kg (ms) <sup>-1</sup> ]	$1.392 \times 10^{-2}$	$1.002 \times 10^{-2}$	$2.86 \times 10^{-2}$	$2.428 \times 10^{-2}$	WEAST (1980)
Density $\rho$ [kg m <sup>-3</sup> ]	$0.999 \times 10^{-2}$	$0.998 \times 10^{-2}$	$0.789 \times 10^{-2}$	$0.785 \times 10^{-2}$	SYNOWIETZ & SCHÄFER (1984)

For injection with resin No. 5 without previous exchange of the porewater with isopropanol, the optimum resin/hardener mixture of 100 : 51 weight percent was often so radically altered that it was no longer possible in some zones for the epoxy resin to harden completely, resulting in loss of material during sample preparation. The results from Sika AG on a synthetic fracture impregnated with resin No. 5 using isopropanol (at the GTS), specifically with a view to investigating the resin/hardener-mixing ratio, confirm that this effect is minimised by the use of isopropanol. The results for five different samples taken from the core are presented in Tab. 2.4.

Tab. 2.4: Resin/hardener-mixing ratios for five selected samples taken from a synthetic fracture impregnated with resin No. 5 (with a pre-injection of isopropanol)

<b>Injection 16 with resin No. 5 (core 5-16)</b>					
Theoretical mixing ratio resin : hardener = 100 : 51 [weight percent]					
Sample	1	2	3	4	5
Actual mixing ratio resin : hardener	100 : 51	100 : 58	100 : 52	100 : 53	100 : 57

### 2.3.4 Additional resin characterisation

*K. Ota and T. Ando*

In addition to the laboratory tests with various resins as described above, JNC characterised intensively two epoxy resins and one acrylic resin: a reference Sikadur 52, a newly formulated resin No. 5 (now called Sika Injection 26) and methyl methacrylate (made available by Toa Gosei Co. Ltd., Japan) respectively. This further laboratory characterisation was made as part of JNC's KTS *in situ* experiments (OTA et al. 1999), to ensure that the resins would actually be capable of meeting the requirements for the immobilisation and recovery of intact rock *in situ* for the following laboratory investigation.

An attempt was made to define important physico-chemical properties of the resins (i.e. pH and molecular weight and size), which had not been investigated but are necessary for evaluating the performance of the resins, in particular possible chemical interactions between the resins and minerals and the penetration depth of the resins into microporosity. Ultrafiltration techniques were applied for the molecular (i.e. polymer) size measurements, which were carried out under small overpressure (0.10 – 0.49 MPa) within 60 minutes after the mixing of resin and hardener. The viscosity and the tensile strength of the resins were determined at longer times at real ambient rock temperatures of 13 – 14 °C (applicable to both the GTS and the KTS). The laboratory tests also involved reacting the resins with excess isopropanol and impregnating air-dried, water-saturated and alcohol-saturated granodiorite matrix samples collected from the KTS with the resins under reduced pressure (below 0.0080 MPa) or over pressure (0.68 – 0.88 MPa), followed by macroscopic examination, aiming at testing the feasibility of resin impregnation under various conditions. For the characterisation of the epoxy resins, the optimum resin / hardener mixing ratios in weight percent were used: 100 : 50 for Sikadur 52 and 100 : 51 for resin No. 5. On the other hand, it was necessary to heat the acrylic resin up to 80 °C to initiate polymerisation for characterisation.

Tab. 2.5 compiles all results of the laboratory characterisation of the epoxy and the acrylic resins and Fig. 2.4 and 2.5 show incremental changes of viscosity and tensile strength of the epoxy resins with time after the mixing of resin and hardener respectively.

Through the further laboratory characterisation of the resins, resin No. 5 proved to be the most suitable for the immobilisation and recovery of intact rock *in situ* for the following laboratory investigation, as discussed in the preceding sections. In particular, the molecular size of resin No. 5 is small enough (2.2 – 2.8 nm) at the beginning of polymerisation. Also the pH value of the resin is relatively high (pH = 11.4) in comparison with the acrylic resin tested (pH = 3.3), and significant interactions between the resin and minerals along porespace (e.g. dissolution of carbonates which occurred in the case of an acid acrylic resin) are not expected. In addition, resin No. 5 has a very low viscosity and a longer polymerisation time at ambient temperatures of 13 – 14 °C and even at 20 °C, as shown in Fig. 2.5. These physico-chemical properties of resin No. 5 enable it to be injected deeper into very fine porespace down to a few nm in size without chemical disturbances. Although resin No. 5 did not satisfactorily polymerise when mixed with a large amount of isopropanol, when exposed to test conditions similar to those of planned *in situ* resin injection, the resin injected could easily displace isopropanol in porespace in the rock matrix and then polymerise sufficiently.

Tab. 2.5: Results of further laboratory characterisation of epoxy and acrylic resins

Test items	Time	Unit	Sikadur 52	Resin No. 5	Methyl methacrylate	Method (temperature)
pH	After mixing	-	12.6	11.4	3.3	Potentiometry (13 °C)
Molecular weight	Resin Hardener	[Mw] [Mw]	400 180	340 180	230 -	GPC (25 °C)
Molecular size	After mixing	[nm]	2.8 – 5.0	2.2 – 2.8	1.5 – 2.2	Ultrafiltration (25 °C)
Viscosity	After mixing	[MPa s]	13 °C	13 °C	<1.5 (20 °C)	Viscometry
	10 min	20 °C	820	83	-	
	30 min	270	1200	105	-	
	60 min	395	1200	225	-	
	90 min	gelled	1200	310	-	
	120 min	polymerised	1200	240	-	
	210 min	-	gelled	500	-	
300 min	-	polymerised	1220	-		
420 min	-	-	gelled	-		
600 min	-	-	polymerised	-		
Tensile strength (fracture point)	After mixing	[MPa]	-	-	5.52 ± 0.44	
	3 days	17.9 ± 3.6	1.01 ± 0.15	-		
	7 days	20.0 ± 3.7	2.68 ± 0.30	-		
	14 days	34.5 ± 5.8	5.85 ± 0.15	-		
	21 days	37.6 ± 3.9	8.63 ± 0.10	-		
	28 days	27.9 ± 3.0	9.90 ± 0.10	-		
Reaction with excess isopropanol			Separated into upper gelled phase and hardened bottom	Suspended after mixing; separated into upper gelled phase and hardened bottom	Mostly evaporated	
Degree of impregnation	Sample		Decompressed	Decompressed	Decompressed	Decompressed
	Air-dried		Not good	Not good	Very good	below 0.0080 MPa; pressurised to 0.68 – 0.88 MPa
	Water-saturated		-	-	Good	-
	Alcohol-saturated		-	-	-	-

- = no measurement

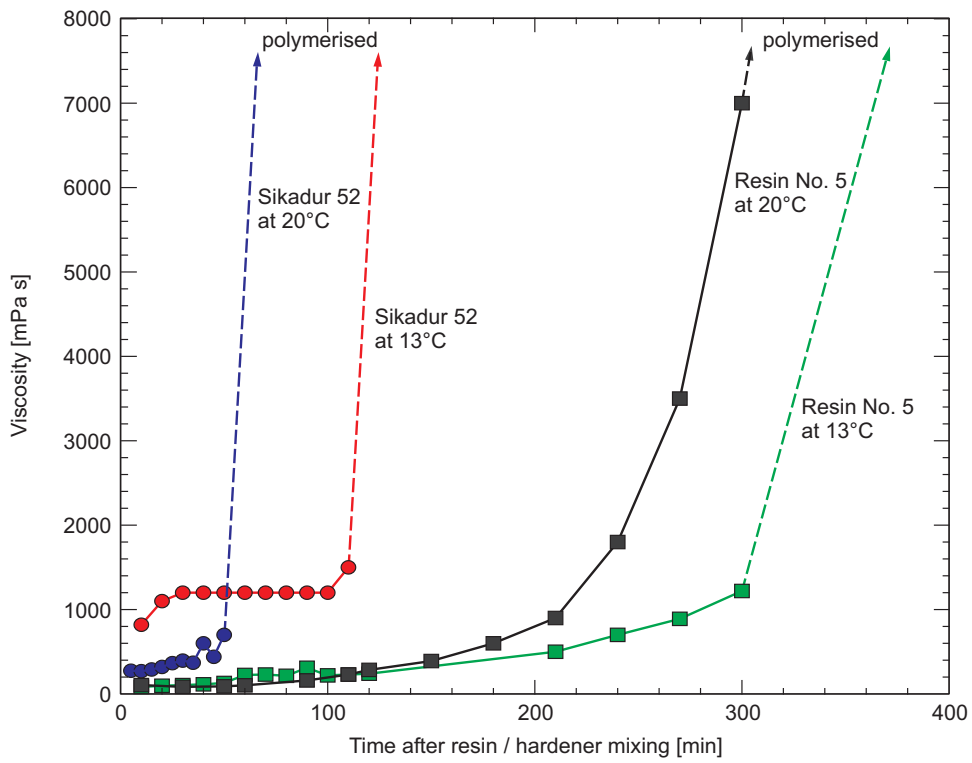


Fig. 2.4: Incremental changes of viscosity of Sikadur 52 and Resin No. 5 with time after mixing of resin and hardener

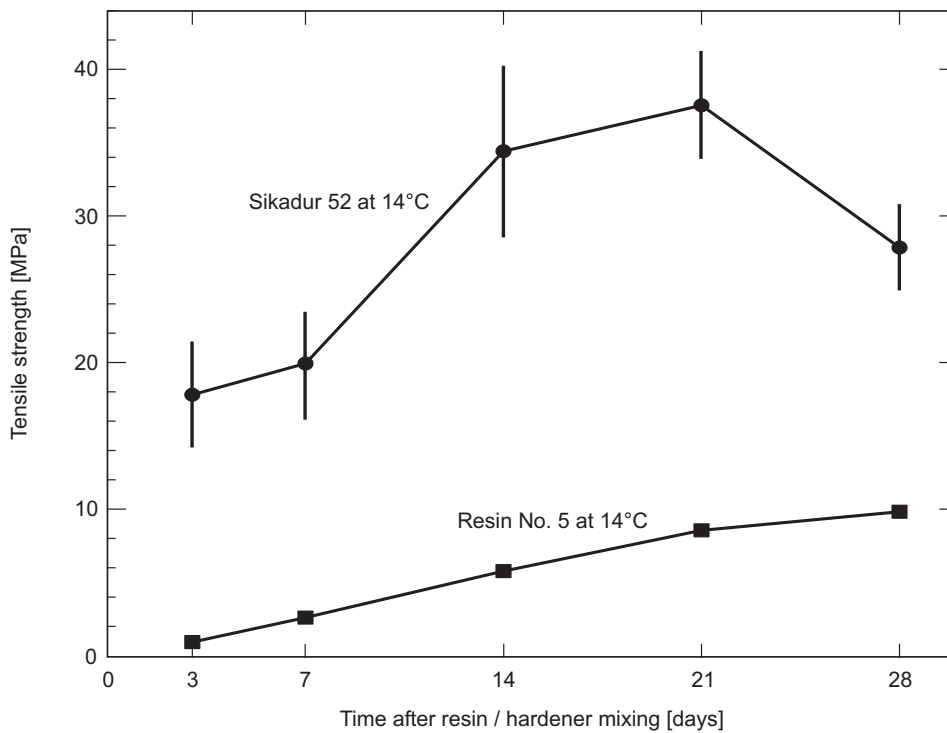


Fig. 2.5: Incremental changes of tensile strength (fracture point) of Sikadur 52 and Resin No. 5 with time after mixing of resin and hardener

## 2.4 *In situ* experiments

*H. Dollinger, Ch. Bühler and P. Bossart*

### 2.4.1 Planned procedure

The procedure selected for the *in situ* impregnation test can be divided into four steps (Fig. 2.6):

- A core between 15 and 20 cm long is drilled into the shear zone using the 200/190 mm (outer/inner diameter) drill bit of a Hilti drilling machine; the core is then removed as this zone could be decompressed and possibly weathered. The surface of the fresh exposure is made as even as possible (hammer and chisel).
- A borehole approximately 35 cm long is then drilled with a 180/172 drill bit; in this case the core is left in place in the borehole.
- A special wide drill bit (198/177) is then used to drill an about 3 cm-deep sealing surface. The empty space between the in-place core and the surrounding rock is filled with silicon rubber. The annulus is cleared of drilling dust and caved-in rock fragments and is filled with rubber from bottom to top. The equipment used for this filling process is the same as that used for the resin injection (injection cylinder and HPLC pump). Once the silicon rubber has hardened, the adaptor cap (Fig. 2.7) can be fitted onto the sealing ring. This sealing ring, which is 9.2 mm wide, is pressed hard against the rubber using a rigid PVC tube, a cross-shaped steel bar and threaded rods anchored in the drift floor. Injection takes place through one of the lines in the adaptor cap while, in the other, pressure is measured using a pressure sensor. Before the resin is injected, the shear zone is saturated with water and it can then be estimated on the basis of the pressure build-up whether or not injection of the epoxy resin is at all possible under the given conditions.
- Once the injected resin has hardened (3 weeks for resin No. 5), the impregnated core is overcored (200/190 drill bit) and recovered.

### 2.4.2 Injection test in shear zone AU138

The form and genesis of shear zone AU138 appear to be similar to those of the experimental shear zone (AU96). Both are around 10 cm thick (mylonite) and contain relatively small reactivated fracture zones (fault gouge zones). However, a significant difference is the absence of water inflow at the drift surface in the case of shear zone AU138. Two boreholes were drilled in shear zone AU138 in order to test prototypes of the adaptor caps and the sealing techniques using silicon rubber. The experience obtained in this preliminary phase was then used to design the test configuration described above. The third borehole for the hydraulic packer tests was then drilled, insulated and instrumented.

Following hydraulic packer tests which indicated very low transmissivity (see Tab. 2.6, below), well below the  $1 \times 10^{-9} \text{ m}^2 \text{ s}^{-1}$  required for successful resin injection, further impregnation tests in this shear zone were abandoned.

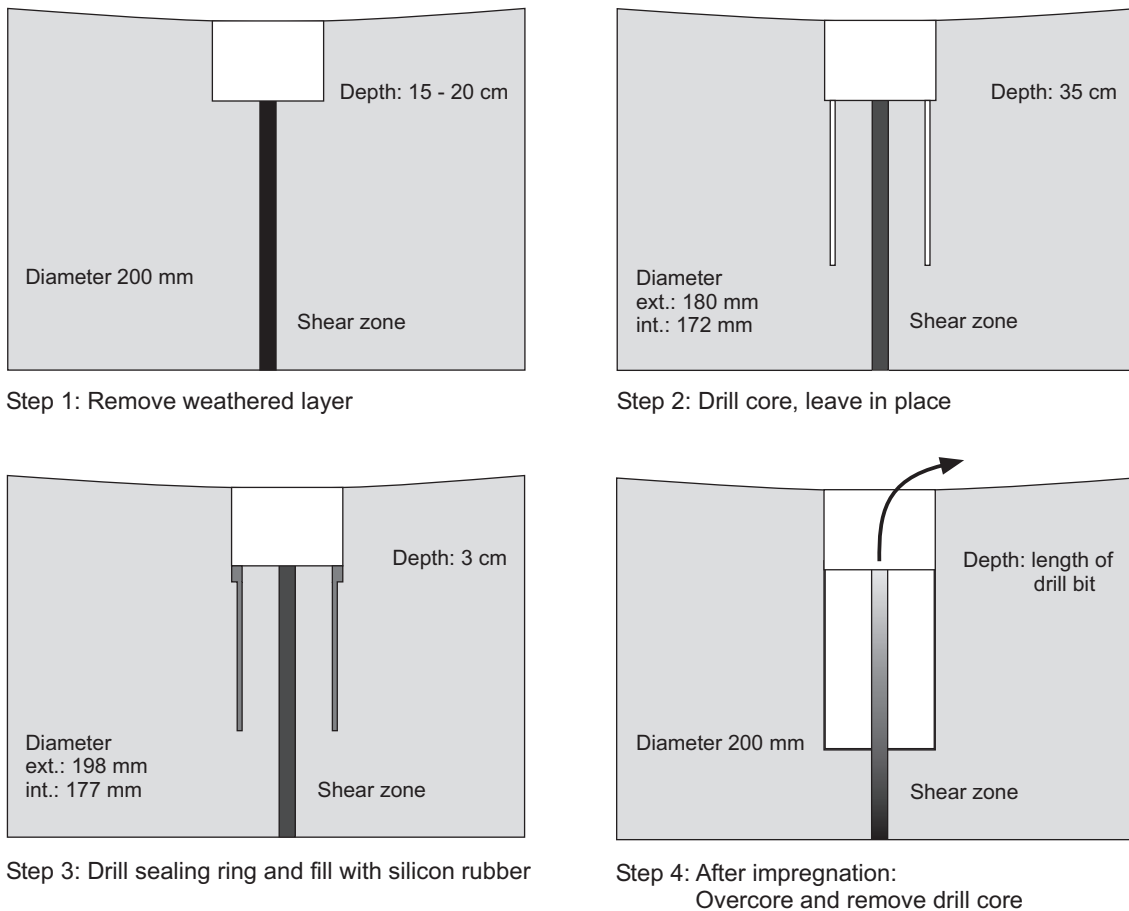


Fig. 2.6: Concept for *in situ* injection

#### 2.4.3 Transmissivities in shear zones AU138 and AU126

The pressure trends recorded during the hydraulic packer tests allow only a very rough estimation of the transmissivities of the tested shear zones. This is due to the absence of a simple conceptual model for this type of test geometry and to insufficiency of data (partly because test durations were too short).

The water injected into the adaptor cap first flows through the injection core which is sealed from the surrounding rock by the silicon rubber. Only when the lower boundary of the silicon rubber has been reached are the flowpaths no longer restricted and water can flow out of the drift wall in the vicinity of the injection borehole (see Fig. 2.6). If the test is continued for a sufficiently long period, steady-state conditions are reached.

The transmissivity of shear zone AU138 can be estimated on the basis of the trend of the pressure curve and the flowrate using the straight-line method (COOPER & JACOB 1946). In the semi-logarithmic diagram in which pressure is plotted against logarithmic time, the points indicating drawdown lie along a straight line. The transmissivity can be calculated from the gradient according to:

$$T = \frac{2.3 Q}{4 \pi \Delta H} = 0.183 \frac{Q}{\Delta H} \quad (\text{Eq. 2.4})$$

where:

- T: Transmissivity [ $\text{m}^2 \text{s}^{-1}$ ]  
 Q: Pumping rate [ $\text{m}^3 \text{s}^{-1}$ ]  
 $\Delta H$ : Difference in potential along the drillcore [m]

For  $\Delta H$ , the value of 1.32 bar/log cycle can be obtained from the log-normal diagram (Fig. 2.8). As the flux was  $3.33 \times 10^{-9} \text{ m}^3 \text{ s}^{-1}$ , taking into account injection into a half-space according to Equation (2.4), the transmissivity can be estimated as  $9.2 \times 10^{-11} \text{ m}^2 \text{ s}^{-1}$ .

For the third hydraulic packer test in shear zone AU126, a value of 0.49 bar/log cycle can be obtained for  $\Delta H$  from the log-normal diagram in the same way. With an injection rate of  $10 \text{ mL min}^{-1}$  ( $= 1.667 \times 10^{-7} \text{ m}^3 \text{ s}^{-1}$ ), taking into account injection into a half-space, a transmissivity of  $1.2 \times 10^{-8} \text{ m}^2 \text{ s}^{-1}$  can be calculated.

Tab. 2.6 presents the transmissivities estimated for shear zones AU138 and AU126 using the straight-line method (COOPER & JACOB 1946). Before epoxy resin can be injected, a shear or fracture zone has to have a minimum transmissivity of approx.  $1 \times 10^{-9} \text{ m}^2 \text{ s}^{-1}$ .

Tab. 2.6: Estimated transmissivities for shear zones AU138 and AU126

	AU138, Test 4	AU126, Test 3
Straight-line method (COOPER & JACOB 1946)	$9.2 \times 10^{-11} \text{ m}^2 \text{ s}^{-1}$	$1.2 \times 10^{-8} \text{ m}^2 \text{ s}^{-1}$

#### 2.4.4 Impregnation in shear zone AU126

Shear zone AU126 was selected for *in situ* resin impregnation in place of the low-permeability shear zone AU138. Shear zone AU126 is genetically, structurally and mineralogically almost identical to the experimental shear zone (MEYER et al. 1989) and contains several reactivated fracture zones over a width of 10 cm and water flows continually out of the shear zone. Based on these visible differences, it was assumed that shear zone AU126 would be sufficiently permeable to allow *in situ* resin injection.

Some problems were experienced due to water inflow forcing the sealing mass injected into the annulus upwards, but it proved possible to fill the annulus with silicon rubber down to a depth of around 20 cm. Following fitting of the adaptor cap, the first hydraulic packer test served mainly to saturate the injection core.

Water was injected at a rate of  $20 \text{ mL min}^{-1}$  in the second hydraulic packer test and at  $10 \text{ mL min}^{-1}$  in the third test. There was good correspondence between the results of the two tests: the pressure of 1.5 bars in the third test correlating well with 3 bars in the second test with double the water injection rate.

Following the water injection tests, isopropanol was injected prior to resin injection. Resin No. 5 was injected over a period of 1.5 hours after the space between the adaptor cap and the rock surface had been filled. The maximum permitted pressure was fixed at 4 bars; the pumping rate therefore had to be reduced from 10 to  $7 \text{ mL min}^{-1}$  approximately 40 minutes after injection began and reduced again after around 50 minutes to  $5 \text{ mL min}^{-1}$ . During the injection phase,

there were several spontaneous drops in pressure, which cannot be explained by changes in the pumping rate. It is possible that these are "frac" phenomena, i.e. fractures are opening as a response to the induced pressure.

Adaptor Cap

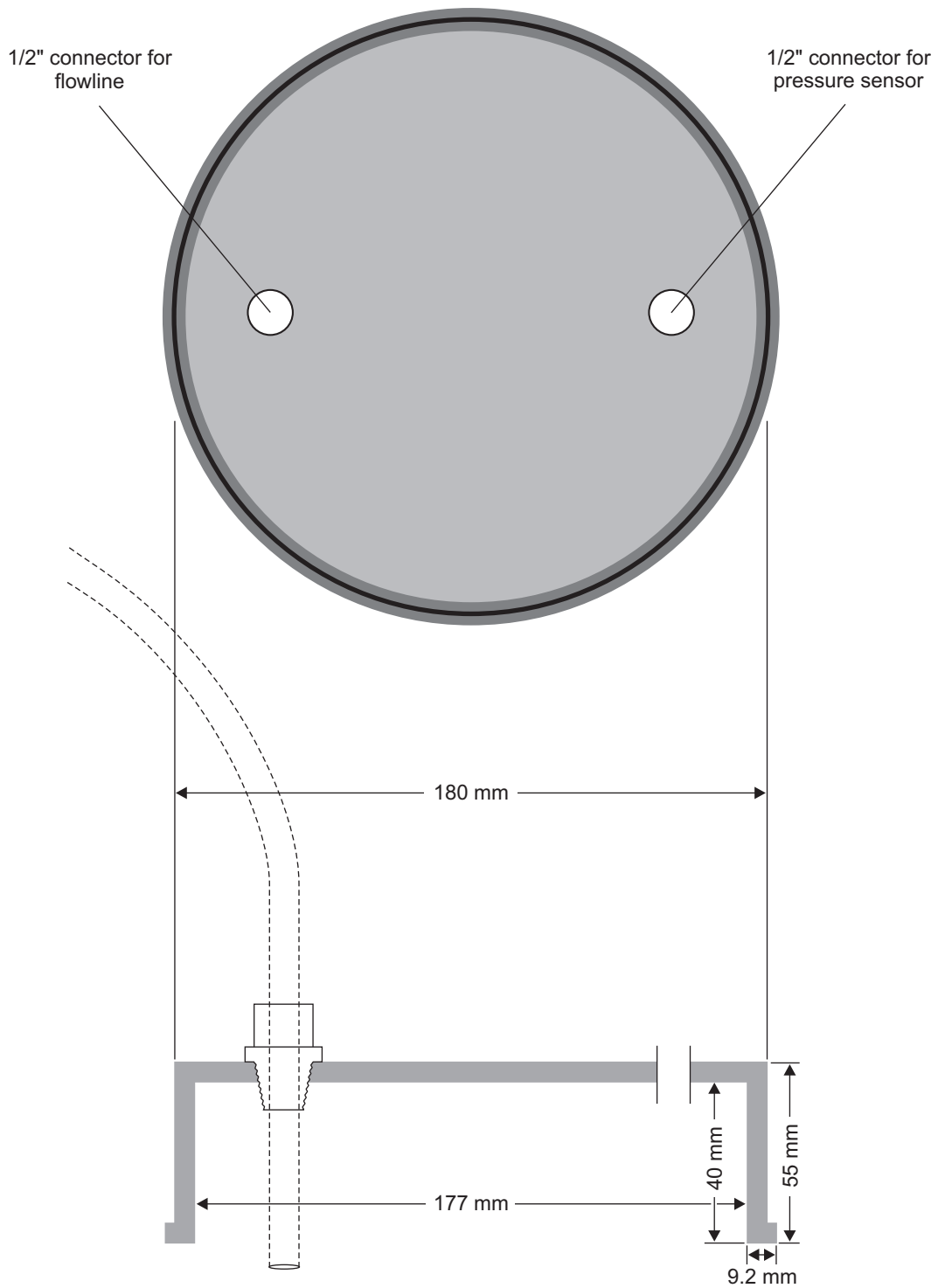


Fig. 2.7: Test adaptor

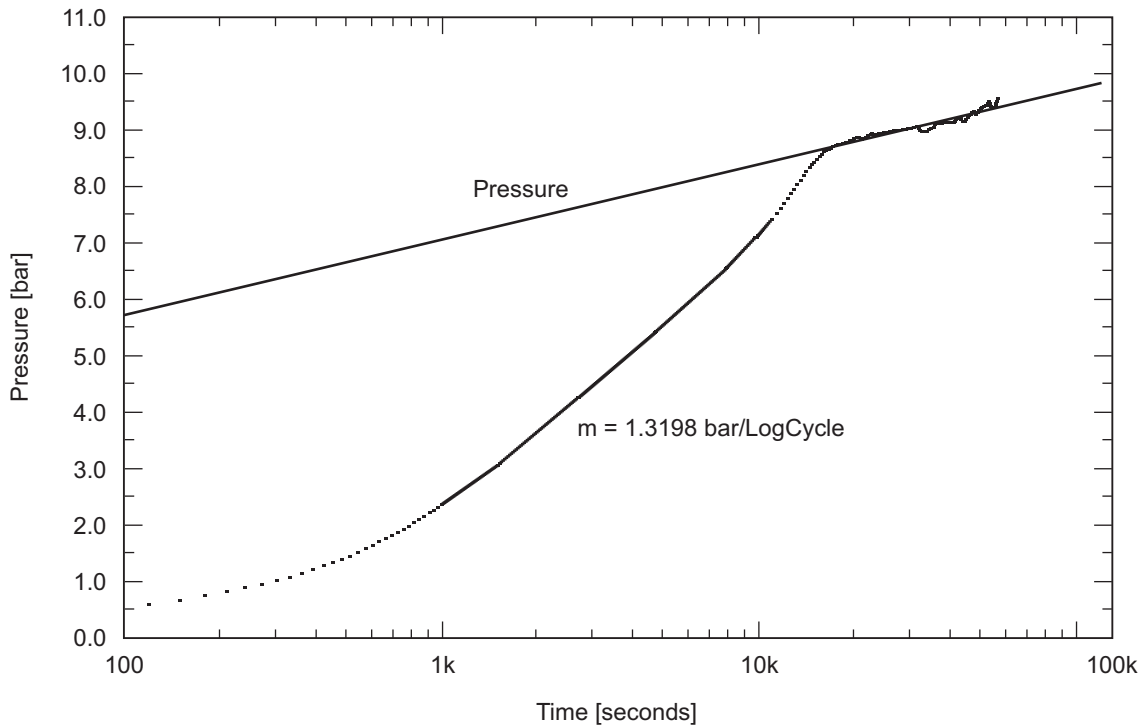


Fig. 2.8: Estimation of transmissivity from hydrotest 4 in AU138 using the straight-line method

#### 2.4.5 Rock fabric investigations of shear zone AU126

The following macroscopic observations could be made on the sawn drillcore:

- The impregnation of the pore spaces is satisfactory to good.
- Along open fractures and fault gouge zones, the resin penetrated more than 50 cm into the rock.
- Particularly noticeable is the well-filled network of narrow open fractures in the area of injection. These fractures were mostly generated artificially by drilling and chiselling out of the uppermost weathered rock zone.
- By way of contrast, the more numerous porous reactivated fracture zones (fault gouges) are only partly impregnated. It was estimated that a maximum of 10 % of this non-cohesive fault gouge material was stabilised mechanically by resin injection. Since the resin takes the path of least resistance, it has to be assumed that, although the porosity of the fault gouge is greater, the fracture apertures are smaller than those of the well-filled, synthetically generated fractures.

Microscopic observations of eleven, variously oriented, thin sections revealed the following:

- Good resin impregnation of the reactivated fracture zones (fault gouges) in the thin sections is clear. If the reactivated fracture zones for which no thin sections were prepared are taken into account, it would appear that more than 50 % of the fault gouge material has been stabilised mechanically, a marked contrast to the estimate of only 10 % impregnation, based on the sawn drillcore.

- Besides branching reactivated fracture zones, fault gouge zones were observed which contain large pieces of rock, which had not been completely cataclastically fragmented.
- A few fault gouge fractures were only marginally impregnated with epoxy resin.
- The narrow, artificially generated fractures, which generally run perpendicular to the direction of cleavage, could also be identified in the thin sections<sup>8</sup>.

#### 2.4.6 Conclusions and future procedures

The physical properties of an "ideal" resin for mechanical stabilisation of a shear zone are largely fulfilled by resin No. 5. If the porewater is first exchanged with isopropanol, a satisfactory impregnation can be guaranteed.

Comparison of the transmissivities for the three shear zones examined in the GTS shows a range of values:

Shear zone AU138:	$T \approx 9 \times 10^{-11} \text{ m}^2 \text{ s}^{-1}$
Shear zone AU126:	$T \approx 1 \times 10^{-8} \text{ m}^2 \text{ s}^{-1}$
Experimental shear zone AU96:	$T \approx 2 \times 10^{-6} \text{ m}^2 \text{ s}^{-1}$

The transmissivity of shear zone AU138 is too low to allow epoxy resin to be injected at relatively low pressures (maximum 5 – 7 bars). The *in situ* experiment was therefore carried out in the water-bearing shear zone AU126. Following exchange of the porewater with isopropanol, the shear zone was impregnated using resin No. 5. Particularly noticeable is how good is the filling of the narrow open fractures in the injection zone which were largely generated by drilling and chiselling activities. However, more than 50 % of the reactivated fracture zones (fault gouges) are also impregnated with epoxy resin. Some open fractures and reactivated fracture zones were filled with resin to a depth of more than 50 cm.

In order to prepare for the final impregnation of a fracture zone labelled with radioactive tracers, it was decided that further *in situ* resin injection experiments were required. It was decided that resin be injected in an artificial dipole field in a shear zone under fully saturated conditions allowing testing of both the technique and equipment prior to use on the experimental shear zone.

### 2.5 Field-scale resin impregnation dipole test

*H. Dollinger, Ch. Bühler, B. Frieg and P. Bossart*

In order to avoid disturbing the experimental shear zone (AU96) another shear zone of similar transmissivity was sought. Hydraulic packer tests carried out in a variety of shear zones similar to AU96 showed that:

- The permeability of most shear zones is an average of 2 to 10 times higher than that of the granitic matrix. The reason for this lack of contrast in permeability between shear zones and matrix is the presence, in the former, of low-permeability fault gouge (BOSSART et al. 1991).

<sup>8</sup> See also the discussion in Möri et al. (2003b) on the borehole disturbed zone (BDZ).

- Compared to the granitic matrix, the storativity (retention capacity) of shear zones (e.g. AU96) which have undergone brittle reactivation is significantly increased (by a factor of 10 – 30). This is seen particularly in the porosity, which is 10 – 30 % in the fault gouge and only around 1 % in the grain boundary and solution pores of the matrix<sup>9</sup>.

Based on previous experience in AU126 and core investigations, it is expected that low viscosity resins can be injected into a shear zone provided the transmissivity is greater than  $5 \times 10^{-9} \text{ m}^2 \text{ s}^{-1}$  and a maximum pumping pressure of 10 bars is utilised (in order to minimise disruption of the fault gouge material: see Section 2.2). In the GTS, however, the number of shear zones with sufficiently high transmissivity which contain reactivated fracture zones (i.e. fault gouge horizons) is limited. Since the final experiment is to be conducted in shear zone AU96 which has a transmissivity of approx.  $2 \times 10^{-6} \text{ m}^2 \text{ s}^{-1}$ , it was decided to conduct the dipole injection experiment either in the extension of the experimental shear zone in the VE drift or, if the transmissivity there was too low, in the shear zone at AU126 where the monopole injection experiment had already been performed.

Four boreholes were drilled in the VE drift but low transmissivities ( $< 10^{-9} \text{ m}^2 \text{ s}^{-1}$ ) and unsaturated conditions were found and this location was abandoned in favour of AU126.

It proved relatively difficult to set up a dipole flowfield with a sufficiently high transmissivity for epoxy resin injection. Between 28 October 1994 and 19 January 1995, six boreholes were drilled in three phases; these penetrated the shear zone more or less perpendicularly. Following each of the three drilling campaigns, the transmissivity of the shear zone was measured in hydraulic packer tests in the new boreholes. Since the measured transmissivities were consistently too low for resin injection, an attempt was made to increase the permeability of the shear zone in boreholes BOEX 94.006 and 95.003 artificially by hydraulic fracturing. This resulted in the development of satisfactory flow between boreholes BOEX 95.003 and BOEX 94.007, 0.35 m away.

However, it is probable that non-cohesive material was removed and water was able to flow along this connection (channel) without any resistance from one borehole to the other, so this artificial flowpath was not identical to the natural channels in the shear zones. It was nevertheless decided to use the BOEX 95.003 as the injection borehole and BOEX 94.007 as the extraction borehole for the experiment as previous experience suggested that finding another natural channelled system would be too costly. To ensure that the injected resin did not simply take the path of least resistance and that low-permeability fracture zones other than the artificially generated channels are also filled with resin, a counter-pressure was generated in the extraction borehole BOEX 94.007 by regulating the outflowrate with a needle valve.

### 2.5.1 Setting up the flowfield

The injection (BOEX 95.003) and extraction (BOEX 94.007) boreholes were each equipped with a mechanical double packer system (Fig. 2.9). In each case, one packer was used to seal off the borehole mouth and the other to isolate the shear zone with the fault gouge horizons up to the end of the borehole. The remaining boreholes (BOEX 94.005, 94.006, 95.001 and 95.002) were sealed off with single packers and filled with water to establish fully saturated conditions. The packer in BOEX 94.006 was installed close to the shear zone and those in the other three boreholes close to the borehole mouth.

<sup>9</sup> New data in Móri et al. (2003b) suggest that the matrix porosity may, in fact, be less than half this figure.

Before installing the double packer systems, the existing flowlines (4 mm internal diameter i.d.) to the lower intervals were replaced with lines with a larger cross-section (8 mm i.d.). This allowed the interval volume to be filled rapidly during resin injection and avoids high frictional losses.

A constant flowfield was established over a period of 4 hours by injecting water into borehole BOEX 95.003 with a flowrate of  $10 \text{ mL min}^{-1}$  and using a needle valve to create a counter-pressure of around 2 bars in borehole BOEX 94.007 (Fig. 2.10 and 2.11). The pressures in all intervals were recorded continuously.

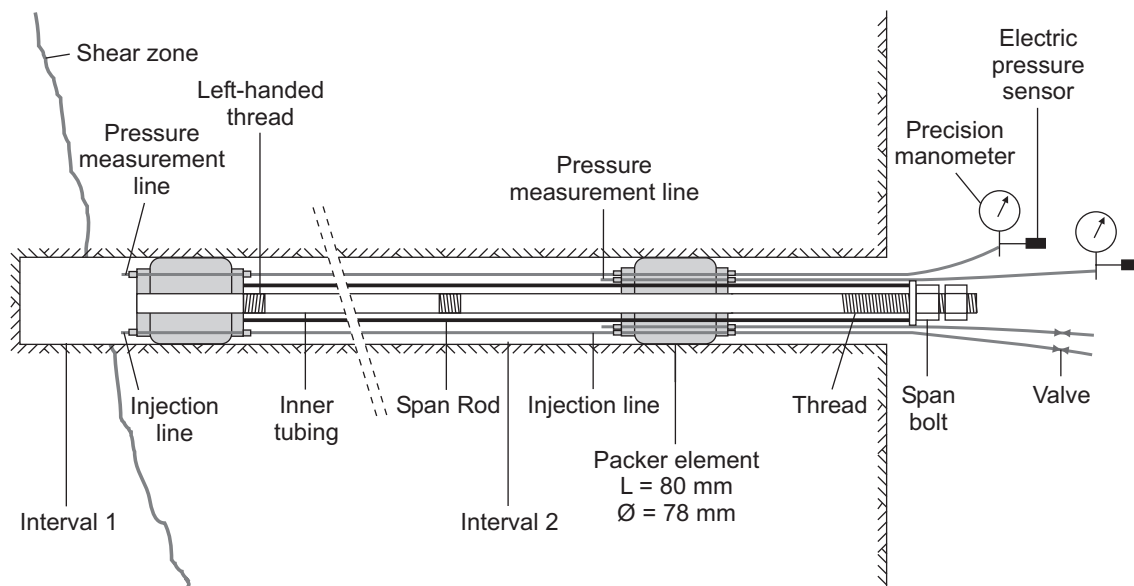


Fig. 2.9: Mechanical double packer system

### 2.5.2 Isopropanol injection

The water was replaced with isopropanol overnight (period of around 15.5 hours). Shortly before beginning the resin injection, the injection of isopropanol was terminated and the isopropanol remaining in the injection interval was extracted using a vacuum pump (Fig. 2.12 and 2.13). This avoids the resin becoming over-diluted by the presence of alcohol in the borehole interval (see Section 2.3).

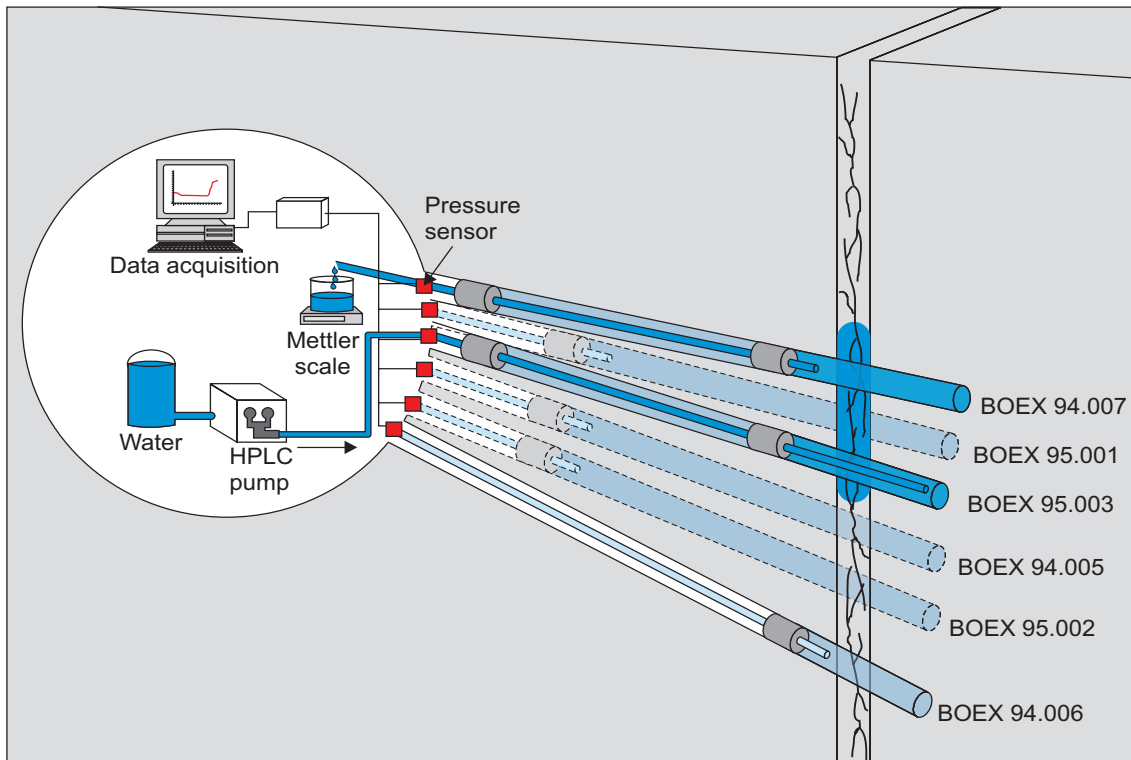


Fig. 2.10: Schematic representation of the experimental dipole (BOEX 95.003 to BOEX 94.007) and water injection

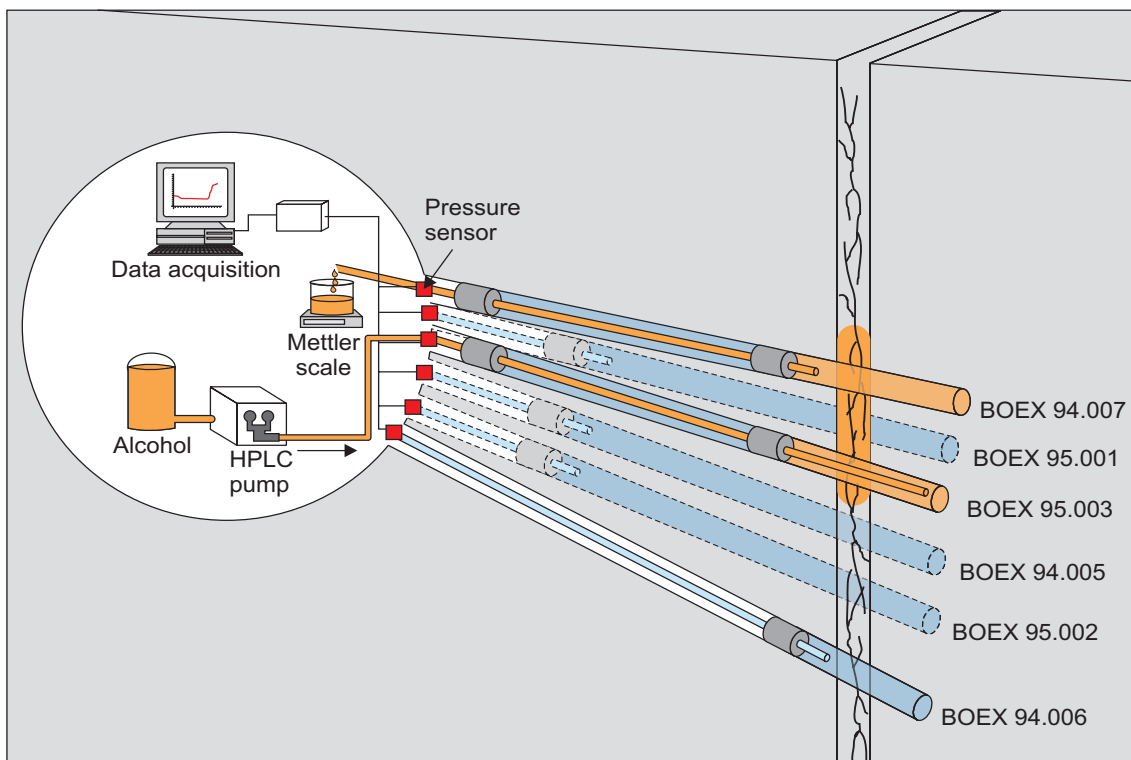


Fig. 2.11: Schematic representation of the experimental dipole (BOEX 95.003 to BOEX 94.007) and isopropanol injection

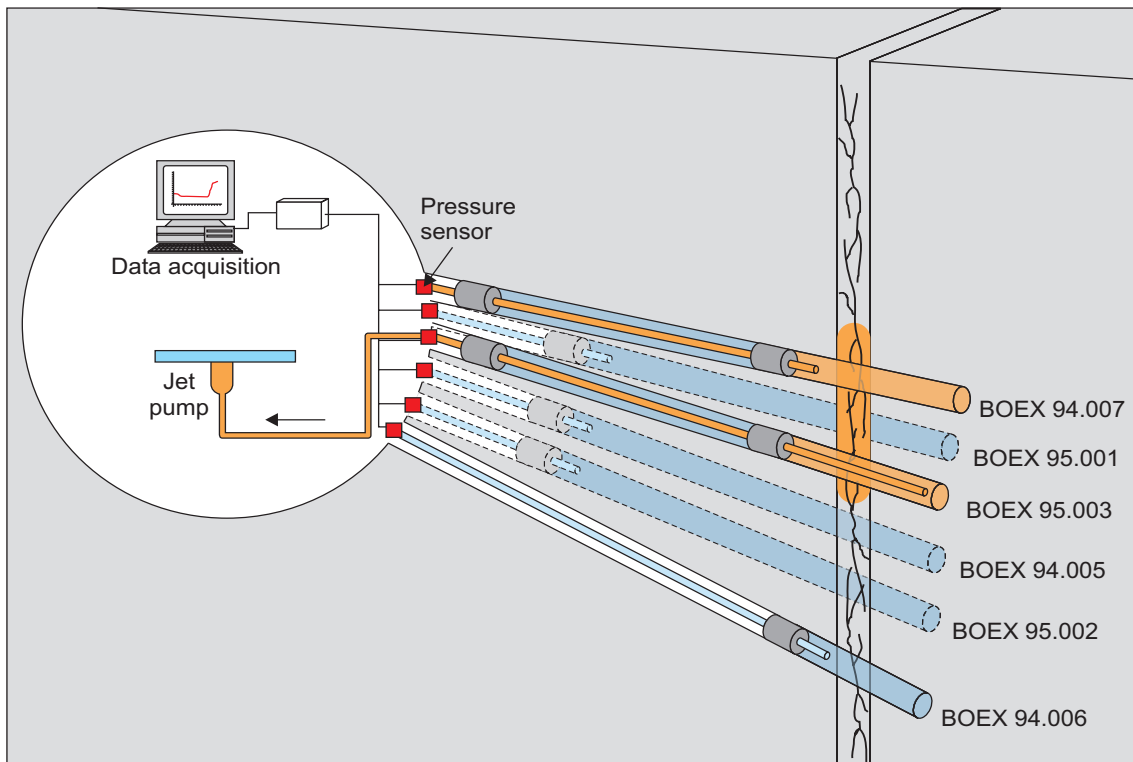


Fig. 2.12: Schematic representation of the experimental dipole (BOEX 95.003 to BOEX 94.007) and isopropanol extraction from injection borehole BOEX 95.003

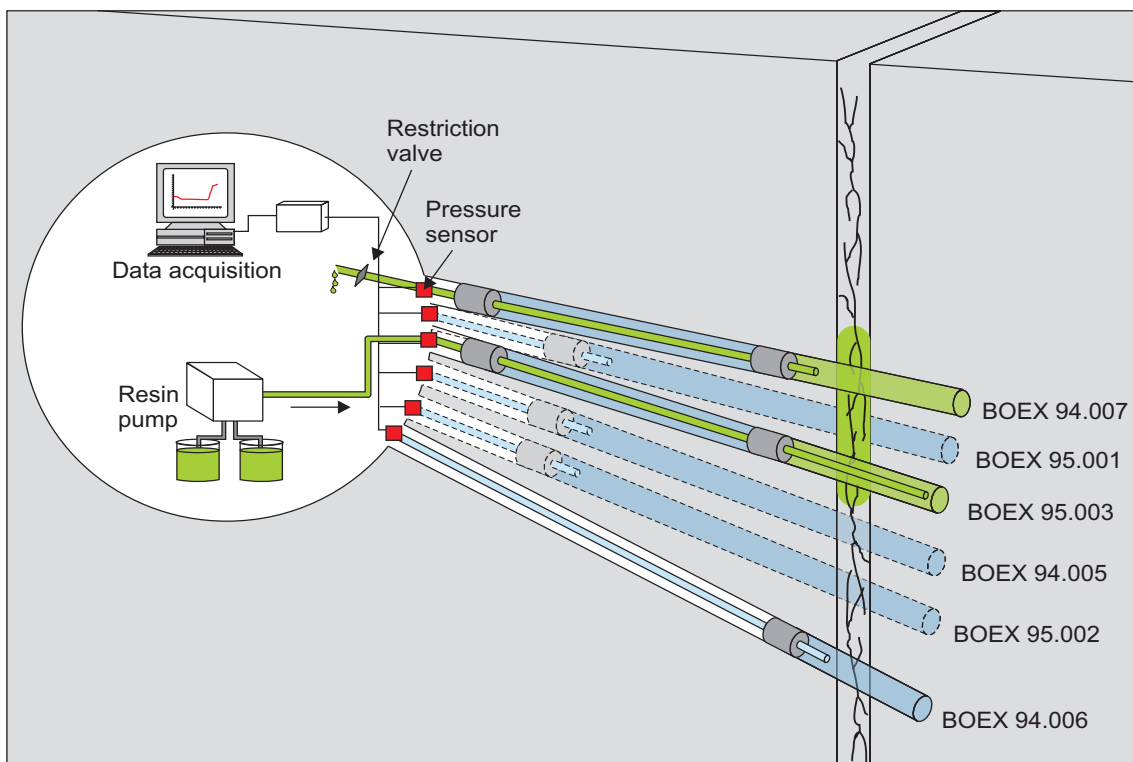


Fig. 2.13: Schematic representation of the experimental dipole (BOEX 95.003 to BOEX 94.007) and resin injection in borehole BOEX 95.003

### 2.5.3 Resin injection

Injection of the low-viscosity resin No. 5 was performed with a hydraulic two-component mixing pump (ECONO-MIX D from the company DOPAG AG in Cham, Switzerland), unlike previous experiments which used an HPLC pump. Fig. 2.14 provides an overview of the functioning of this two-component system which allows mixing the resin and the hardener either dynamically or statically. However, in the planned dipole experiment and the final experiment, low to very low injection rates will only be necessary at the end of the injection experiment, so dynamic mixing was not required.

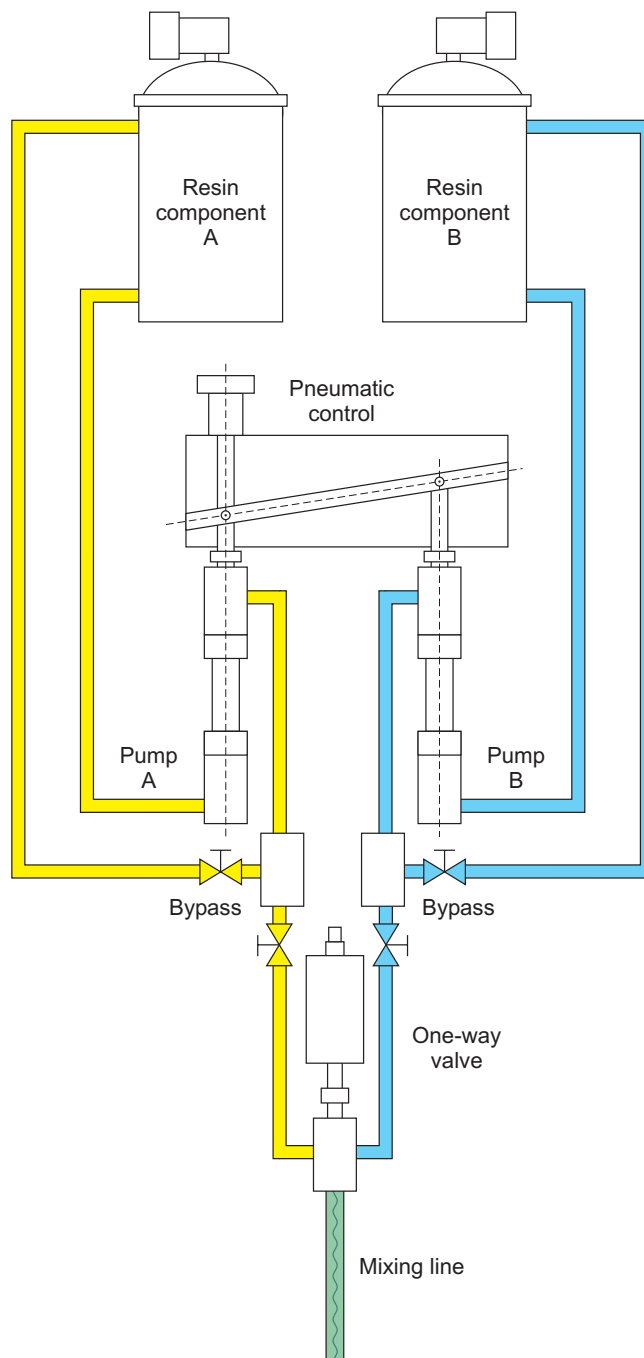


Fig. 2.14: Sketch of the DOPAG mixing pump ECONO-MIX D

The mixing and batching system was set up for the desired ideal resin/hardener-mixing ratio of 100 : 51 and then tested. Tests were performed with both high and low flowrates and resin samples were taken for the purpose of analysing the resin/hardener mixing ratios. Analyses performed by SIKKA AG have shown that a correct resin/hardener-mixing ratio can be achieved with a high flowrate of  $2.7 \text{ L min}^{-1}$ . At lower flowrates, for example between the minimum  $150 \text{ mL min}^{-1}$  and up to  $1.5 \text{ L min}^{-1}$ , the samples were underhardened by around 5 %, i.e. the hardener portion was 5 % lower than the planned optimal theoretical relationship of resin and hardener (100 : 51).

Since the viscosity of epoxy resins is highly temperature-dependent, both resin and hardener were warmed to around  $30 - 35 \text{ }^\circ\text{C}$  prior to injection.

Before the dipole experiment, a last test of the mixing pump was made by injecting resin into BOEX 94.006 where non-cohesive fault gouge material had been washed out into the drift as a result of artificially increasing the transmissivity in this borehole. After 15 minutes injecting at a flowrate of  $50 - 150 \text{ mL min}^{-1}$  (4 – 10 bar in the injection interval), the flowrate increased rapidly and a few minutes later resin appeared at the wall of the drift, suggesting that the channel was plugged.

#### 2.5.4 Resin injection into borehole BOEX 95.003 (dipole flowfield)

During the actual dipole resin injection test, the packed-off borehole interval in BOEX 95.003, from which isopropanol had been extracted, was filled with resin at a rate of approximately  $1.5 \text{ L min}^{-1}$ . After a period of 165 minutes, a total of approximately 540 mL of resin had been injected into the shear zone. Sampling of the extraction borehole indicated that about 180 mL of resin had also flowed out into this borehole. Based on core observations, it can be assumed that this resin reached the extraction borehole directly via channels. This means that the remaining 360 mL hardened in the shear zone. Tab. 2.7 gives the measured and estimated resin volumes injected into the shear zone AU126 during the dipole test.

Tab. 2.7: Volumes of resin injected in the dipole resin injection test

Volumes	Quantity of resin
Dead volume of pump, lines, etc.	approx. 710 mL (estimated by difference)
Volume of injection interval BOEX 95.003	approx. 3250 mL (calculated)
Volume flowing into extraction interval BOEX 94.007	approx. 180 mL (calculated)
Volume injected into shear zone	approx. 360 mL (measured)
<b>Total injected volume</b>	<b>approx. 4500 mL (measured)</b>

### 2.5.5 Overcoring shear zone AU126

The success of the dipole resin injection was checked by overcoring. Once the resin hardened, after around three weeks, three boreholes were drilled perpendicular to the resin-impregnated shear zone.

The first overcoring borehole (BOEX 95.004) was located between the injection and extraction boreholes, parallel to the injection borehole. An attempt to use a large diameter single core barrel was unsuccessful as the shear zone broke up and was washed out to a large extent. It was therefore decided to drill the remaining overcoring holes with a double core barrel (outer diameter 131 mm, inner diameter 108 mm). Borehole BOEX 95.005 was abandoned before reaching the shear zone as water losses prevented the drill cuttings from being removed. Despite using a double core barrel for borehole BOEX 95.006, the fault gouge horizons and mylonite zones again broke up and were washed out.

In contrast to drilling normal to the shear zone, overcoring parallel to the shear zone (c.f. also BOSSART et al. 1991) was more successful. A total of four boreholes were drilled between the injection (BOEX 95.003) and extraction (BOEX 94.007) holes. Fig. 2.15 shows locations of the overcoring boreholes relative to the injection and extraction boreholes and Fig. 2.16, the reconstructed breakthrough points of these four boreholes in the plane of the injection and extraction boreholes.

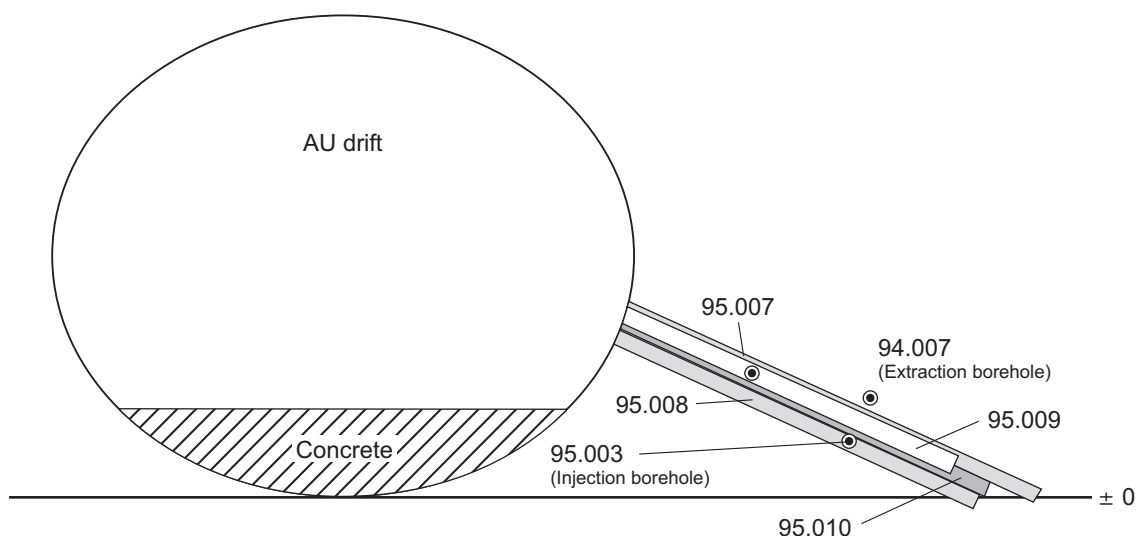


Fig. 2.15: Overcoring parallel to the plane of the shear zone AU126 (view to the South), diameter of the boreholes is 131 mm, scale 1 : 50

The four core sections from boreholes BOEX 95.007 to 95.010 containing impregnated zones were stabilised by injecting epoxy resin (without fluoresceine) into the PVC core tube. The cores were then sawn along the XZ plane into 7 to 20 mm thick discs. It was impossible to produce samples from the XY and/or YZ planes in addition to the XZ samples, because of the small drilling diameter (core diameter 108 mm). The XZ plane contains the stretching lineation (see BOSSART et al. 1991 and MÖRI et al. 2003a) and lies normal to the cleavage (c.f. also Sections 2.2 and 2.3). Thin sections and some polished slabs were prepared from selected areas.

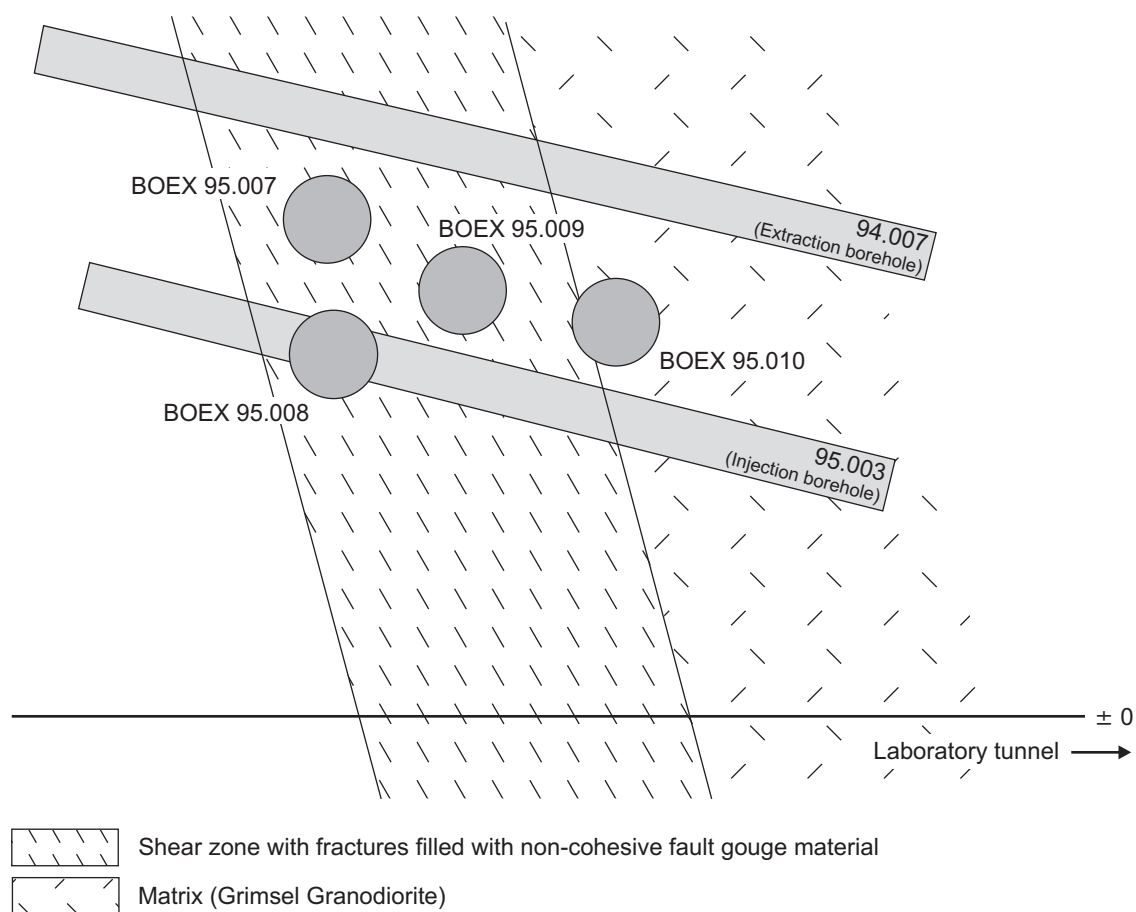


Fig. 2.16: Vertical section in the XZ plane of the injection and extraction boreholes: points of intersection of overcoring boreholes parallel to the plane of the shear zone AU126, diameter of the boreholes is 131 mm, scale 1 : 10

### BOEX 95.008

This hole was drilled through the injection borehole BOEX 95.003 in the southern section of the shear zone (Fig. 2.16). On the macroscopic scale, the following observations can be made with regard to resin impregnation:

- Around the injection borehole, a well impregnated excavation disturbed zone of about 1.5 cm thickness is clearly displayed. This was probably created by the drilling procedure causing loosening of the fabric. Other structures aligned more or less at right angles to the cleavage were probably also generated artificially by the drilling process.
- Coarse-grained quartz-feldspar aggregate also showed good impregnation. The resin appeared to have flowed mainly along transgranular fissures and grain boundary pores. Resin was observed to have penetrated at least 8 cm in the XZ sections.
- In the XZ sections, fault gouge horizons up to approx. 2.5 cm around the injection borehole are completely filled with resin.

Thin sections were prepared only from the best impregnated sections of the core, hence microscopic observations are not typical of the whole core. Despite this, producing thin sections was

still not straightforward as the rock broke up to some extent along non-impregnated cleavage surfaces.

The observations made in this study confirm those from the earlier *in situ* monopole experiment (Section 2.4):

- Impregnation of the fault gouge horizons ranges from good to very good. However, branching fault gouge horizons and horizons only marginally impregnated with resin suggest that the resin did not use all the available pore space as a flowpath and may only preserve the main water flowpaths (c.f. results in MÖRI et al. 2003a, where results indicate that the resin uses all available flowpath)
- The fissures (frequently transgranular) which commonly occur within a radius of approximately 1.5 cm around the injection borehole were presumably generated by the drilling process and were filled with resin (c.f. comments in MÖRI et al. 2003b on the BDZ).
- Narrow fissures at right angles to the cleavage also occur with reasonable frequency; these were probably also generated by the drilling process (c.f. comments above).

A resin-only sample from the injection interval in borehole BOEX 95.003 was passed to Sika AG for analysis of the resin/hardener-mixing ratio. This sample proved to be slightly under-hardened (8 %).

#### **BOEX 95.010**

This borehole was drilled in the vicinity of the injection borehole in such a way that it contained around half shear zone and half granodiorite matrix (Fig. 2.16).

An artificially generated channel oriented parallel to the cleavage could be clearly identified in this borehole. At a distance of a few millimetres from the shear zone/granodiorite matrix transition, the shear zone contains one and occasionally two fault gouge horizons. When the transmissivity was artificially increased in borehole BOEX 95.003, this weakly cohesive material was washed out into the borehole as a result of abrupt pressure relief. The channel runs more or less perpendicular to the borehole.

Rock fragments can be clearly seen suspended in the resin within this channel and probably represent the remaining fault gouge components. The epoxy resin penetrated a maximum of 1 cm from the channel into the intact fault gouge zones. The transgranular pores and the grain boundary pores in the quartz-feldspar mosaic located between the fault gouge horizons and the granodiorite matrix are better impregnated since the pores apparently have larger apertures.

#### **BOEX 95.009**

In this borehole, sections of the shear zone were removed which were between 3 and 16 cm distant from the injection borehole (Fig. 2.16). Impregnated flowpaths could only be identified after the core had been sawn up. They are restricted to only a few locations in the core and do not extend any distance in the XZ plane.

Microscopic analyses of thin sections have shown that there are both impregnated fault gouge horizons and narrow impregnated fissures which run obliquely to the direction of the cleavage and were also generated artificially by drilling the injection or extraction borehole.

**BOEX 95.007**

This borehole was drilled just below extraction borehole BOEX 94.007. Neither macroscopic nor microscopic investigations revealed flowpaths filled with resin. The reason for this could be that this borehole is located furthest away from the injection borehole (Fig. 2.16) and the resin is more or less restricted to the highest permeability channels or decompressed zone round the injection borehole.

**2.5.6 Conclusions**

From this *in situ* dipole experiment it was concluded that, provided the porewater is first replaced with isopropanol, water flowpaths can be sufficiently well impregnated with the low-viscosity epoxy resin No. 5. To obtain even better quantitative information, it is suggested that, for any further test resin injections, the injection and extraction boreholes should have a smaller diameter (e.g. 30 mm). Once resin injection is complete, the injection and extraction holes should be overcored with the double core barrel (131 mm in diameter). In order to stabilise the extraction borehole prior to overcoring, it should first be filled with a conventional epoxy resin (without fluoresceine). This should allow a complete, continuous description of the impregnated pore spaces, at least in the areas near the borehole.

Based on the experience from this dipole injection experiment, it was recommended that, for the final experiment, the resin-impregnated zone be recovered by drilling in the plane of the shear zone with large-diameter corers. Producing XZ, YZ and XY sections from the recovered cores would then allow a 3-D investigation of the pore space. The flowpath geometry can be determined using "scanned" core slices and thin sections with special databank and visualisation software (see ALEXANDER et al. 1996, for details).

### 3 Radionuclide sorption effects

In the previous chapter, the investigation of a suitable resin composition and methodology for impregnation and immobilisation of the migration shear zone was described. Besides physical immobilisation, the introduction of the resin must also chemically immobilise the components of the shear zone so that further interaction, such as between radionuclides and resin, does not take place. Further potential problems arise from the use of an organic solvent to displace the water – this may cause radionuclide distributions within the fracture zone to be disturbed or altered if the radionuclides are desorbed from the rock by the solvent. This chapter describes the results of laboratory studies into the sorption properties of the resins, sorption of tracers onto equipment and the effects of the solvent on tracer sorption. A study on the influence of kinetics in the initial sorption of radionuclides in the migration shear zone is also reported here.

#### 3.1 Evaluation of the sorption properties of resins

*J.A. Berry and M. Cowper*

As this study took place before the work on the optimum resin composition for injection had been completed, two representative resin compositions were used: an acrylic resin supplied by Rascor AG and a low-viscosity epoxy resin supplied by Ciba-Geigy AG. The epoxy resin was supplied as hardener (XHY 848) and araldite resin (BY 158). Also supplied by Nagra for use in the experiments were eight granodiorite polished thin sections, six 1 cm<sup>3</sup> granodiorite blocks with one polished face and an assortment of unpolished granodiorite offcuts.

The behaviour of the acrylic resin, in particular swelling, perturbation of solution pH and release of organics into solution, quickly made it clear that such resins would be unsuitable for the resin injection. Hence, mainly the results of the study of the epoxy resin will be described here.

##### 3.1.1 Methodology

The work was subdivided into three tasks:

##### **Reservoir Depletion Experiments**

Small blocks of cured resin were immersed in a solution containing three radionuclides for 2 – 3 months. The fall in radionuclide concentration with time was monitored in order to determine the sorptivity of each resin. In complementary experiments, small resin blocks and granodiorite samples were immersed in the same solution in order to study the competition between the two.

##### **Leaching Experiments**

Polished thin sections of Grimsel granodiorite were immersed in solutions containing two radionuclides for 1 – 3 months. Approximate surface loading could be determined from analysis of the solution after the thin section was removed. Liquid resin was then allowed to flow across the surface (and was analysed for any radionuclide removed) in an attempt to assess any potential *in situ* removal of the radiotracers from the rock surface as the resin is injected.

### Depth Profile Experiments

Polished blocks of granodiorite were immersed in solutions containing inactive radioelement simulants for 2 – 3 months. A thin layer of liquid resin was applied to the surface and allowed to cure. Any uptake of sorbed elements during the resin hardening, due to diffusion, dissolution or uptake of pore fluids, was investigated by Dynamic Secondary Ion Mass Spectrometry (SIMS).

The three radionuclides chosen for the study were  $^{237}\text{Np}$ ,  $^{137}\text{Cs}$  and  $^{60}\text{Co}$ . Inactive Cs and Co were used for the depth profiling experiments. All three were among the key elements being considered at the time for use in the final field experiment. The three elements also cover a wide range of different chemistries from alkali metals (Cs) and transition metals (Co) to actinides (Np).

The chemical composition of groundwater from the AU96 fracture within the shear zone at Grimsel is a low ionic strength ( $10^{-3}$  M), high pH (9.6) solution saturated with respect to calcite (BAJO et al. 1989). However, due to possible solubility problems with Co and Np at pH 9.6, it was decided to use ultra-high purity (UHP) water at pH 7 – 8 as the solution in all experiments. It is also well documented that Cs sorption is inhibited by the presence of other monovalent cations (BERRY et al. 1990). Modelling using the HARPHRQ code (BROWN et al. 1990) predicted that the carbonate concentration in UHP water in equilibrium with atmospheric  $\text{CO}_2$  would be  $10^{-5}$  M.

All experiments were carried out in a fume cupboard. As strongly reducing conditions were not required, nitrogen atmosphere glove boxes were not employed.

Determination of the  $^{60}\text{Co}$  and  $^{137}\text{Cs}$  concentrations was by  $\gamma$ -spectrometry.  $^{237}\text{Np}$  concentrations were determined by  $\alpha$ -spectrometry following electrodeposition of the samples using the ammonium sulphate method (TALVITIE 1972).  $^{236}\text{Pu}$  was used as a known activity tracer for Np analysis.

In case of possible sorption of any of the elements onto the vessel walls, all bottles were washed in 10 %  $\text{HNO}_3$  and the washings analysed by the methods above.

### 3.1.2 Results and Discussion

#### Reservoir depletion experiments

In experiments where epoxy resin only is present, there is little sorption of any of the three elements (Tab. 3.1). After 1350 hours, the Co concentration had fallen less than 5 % (when including  $2\sigma$  errors). Within error, no Cs or  $^{237}\text{Np}$  sorbed in either experiment. This contrasts markedly with experiments 3B and 4B where granodiorite blocks were also present (Tab. 3.1). In these there is a rapid fall in both Co and Cs concentrations in the first 400 hours after which the decrease levels off. No  $^{237}\text{Np}$  was observed to sorb in 3B but some sorption (65 % of initial concentration after 1350 hours) was observed for 4B. Unlike in the case of the acrylic resin, the pH remained within  $7.1 \pm 0.3$  during the course of the experiment and no swelling or dissolution was observed.

Acid washing of vessel walls after the experiments had finished showed that no wall sorption had occurred in either set of resin experiments.

### Leaching Experiments

No Cs was found to be desorbed from the surface of the thin section by either epoxy or acrylic resin. However, because the surface loading was quite low, two more experiments, TS5 and 6, were started. Polished thin sections of granodiorite were immersed in 100 cm<sup>3</sup> of a <sup>137</sup>Cs solution of initial concentration 40 Bq cm<sup>-3</sup>, which is equivalent to a total Cs concentration of 3.1 × 10<sup>-10</sup> M. The experiments were run for 218 and 195 hours, respectively. Even with higher loading, the uptake of Cs from the surface by either resin was less than 1 %.

Tab. 3.1: Results of the epoxy resin (+ granodiorite) reservoir depletion experiments

Time [hrs]	<sup>237</sup> Np Concentration [ $\times 10^{-8} \text{ M} \pm 2 \sigma$ ]		Total Cs Concentration [ $\times 10^{-8} \text{ M} \pm 2 \sigma$ ]		Total Co Concentration [ $\times 10^{-8} \text{ M} \pm 2 \sigma$ ]	
<b>Epoxy resin only</b>						
	Expt 1B	Expt 2B	Expt 1B	Expt 2B	Expt 1B	Expt 2B
0.00	3.85 ± 0.40	3.85 ± 0.40	4.50 ± 0.90	4.50 ± 0.90	4.95 ± 0.48	4.95 ± 0.48
75.00	3.88 ± 0.42	8.36 ± 1.09	4.36 ± 0.64	6.85 ± 2.07	4.80 ± 0.70	4.74 ± 0.71
123.00	4.04 ± 0.50	3.69 ± 0.39	4.32 ± 0.62	5.55 ± 0.69	4.62 ± 0.50	4.92 ± 0.50
169.17	4.80 ± 0.53	6.89 ± 0.80	3.45 ± 0.48	6.43 ± 0.73	4.11 ± 0.66	5.99 ± 0.75
245.67	4.97 ± 0.66	6.55 ± 0.77	3.86 ± 0.46	5.80 ± 0.52	4.72 ± 0.67	4.73 ± 0.67
339.00	4.85 ± 0.54	2.54 ± 0.28	4.04 ± 0.36	5.62 ± 0.58	4.73 ± 0.50	4.56 ± 0.48
435.08	3.53 ± 0.39	5.48 ± 0.60	3.71 ± 0.35	5.56 ± 0.58	4.67 ± 0.49	4.90 ± 0.50
630.58	2.78 ± 0.31	5.40 ± 0.70	3.40 ± 0.33	5.54 ± 0.49	4.14 ± 0.46	4.34 ± 0.46
1105.0	3.27 ± 0.39	3.74 ± 0.39	3.71 ± 0.34	5.29 ± 0.49	4.34 ± 0.47	4.73 ± 0.50
1349.5	4.72 ± 0.49	5.01 ± 0.54	3.73 ± 0.19	5.07 ± 0.26	4.13 ± 0.25	4.31 ± 0.25
<b>Epoxy plus Granodiorite</b>						
	Expt 3B	Expt 4B	Expt 3B	Expt 4B	Expt 3B	Expt 4B
0.00	3.85 ± 0.40	3.85 ± 0.40	4.50 ± 0.90	4.50 ± 0.90	4.95 ± 0.48	4.95 ± 0.50
75.00	4.89 ± 0.52	3.64 ± 0.40	3.78 ± 0.64	6.85 ± 0.81	1.87 ± 0.44	3.00 ± 0.53
123.00	5.32 ± 0.59	2.41 ± 0.26	3.23 ± 0.62	5.55 ± 0.41	1.45 ± 0.26	2.00 ± 0.32
169.17	13.46 ± 1.46	6.51 ± 0.76	3.16 ± 0.48	6.43 ± 0.36	1.23 ± 0.34	1.79 ± 0.42
245.67	3.67 ± 0.40	5.72 ± 0.63	2.09 ± 0.46	5.80 ± 0.29	0.52 ± 0.16	1.31 ± 0.32
339.00	1.56 ± 0.17	3.93 ± 0.41	1.75 ± 0.36	5.62 ± 0.27	0.72 ± 0.18	0.98 ± 0.29
435.08	5.24 ± 0.55	3.85 ± 0.41	1.81 ± 0.35	5.56 ± 0.27	0.47 ± 0.17	0.87 ± 0.25
630.58	3.41 ± 0.40	1.80 ± 0.20	1.66 ± 0.33	5.54 ± 0.25	0.64 ± 0.19	0.73 ± 0.25
1105.0	4.19 ± 0.44	1.59 ± 0.17	1.68 ± 0.34	5.29 ± 0.23	0.65 ± 0.21	0.53 ± 0.07
1349.5	4.98 ± 0.54	2.49 ± 0.25	1.54 ± 0.19	5.07 ± 0.23	0.59 ± 0.10	0.62 ± 0.10

Unfortunately, with <sup>237</sup>Np, no way was found of dissolving and analysing the resins once they had hardened.

The conclusions from the leaching experiments are that neither resin desorbs significant Cs from the surface of granodiorite.

### Depth Profile Experiments

The polished blocks of granodiorite immersed in inactive Co and CsCl<sub>2</sub> solutions were removed after 75 days. A Co-exposed block was coated with the acrylic resin and a Cs-exposed block was coated with epoxy resin. Due to the viscosity of each resin, the liquid resin was allowed to flow across each block at an angle as pipetting a drop onto the surface did not result in full resin dispersion. Both samples were sent for SIMS analysis along with the duplicates and also unexposed granodiorite blocks as blanks.

The insulating nature of each resin and the rock meant that few SIMS profile data were obtained. However, on one epoxy-coated sample, the Cs profile showed an increasing concentration as the surface of the rock is approached. This suggests that some Cs uptake from the surface during the resin curing has occurred. However, comparing the quantity (about 10<sup>4</sup> counts) with that sorbed on the surface of the uncoated block (about 10<sup>6</sup> counts), it appears that less than 1 % was taken up by the resin. This is consistent with the results from the leaching experiments.

#### 3.1.3 Conclusions

Neither resin sorbs significant quantities of radionuclides, particularly when in competition with Grimsel granodiorite. Furthermore, neither resin desorbs Cs from the surface of granodiorite after contact. However, the acrylic resin swelled considerably when immersed resulting in a drastic decrease in pH and release of organics into solution. This would be expected to alter significantly the *in situ* distribution of radionuclides along the flowpath after the migration experiment.

### 3.2 Desorption of radionuclides by propan-2-ol

*G.M.N. Baston, J.A. Berry, M. Brownsword and P. Oliver*

A study of the desorption of eight elements from rock by propan-2-ol (as an analogue of isopropanol) was undertaken in order to check the suitability of the *in situ* use of alcohol prior to the injection of resin.

#### 3.2.1 Methodology

Samples of three of the radioelements in question were available already sorbed onto crushed rock from a previous experiment. These were:

- i) <sup>95m</sup>Tc as Tc(IV) sorbed onto granodiorite,
- ii) <sup>75</sup>Se as SeO<sub>3</sub><sup>2-</sup> sorbed onto sandstone, and
- iii) <sup>233</sup>U as U(IV) sorbed onto granodiorite.

In order to provide samples of the remaining radioelements sorbed onto mylonite, duplicate samples (0.4 g) of the crushed rock were equilibrated with 20 cm<sup>3</sup> synthetic Grimsel ground-water (see Appendix A) 'spiked' with the appropriate radioelement. The species used were:

- iv) <sup>152</sup>Eu as Eu (III)
- v) <sup>237</sup>Np as Np (V)
- vi) <sup>238</sup>Pu as Pu (IV)
- vii) Inactive Mo as NaMoO<sub>4</sub>
- viii) Inactive Sn as Sn (IV) Cl<sub>4</sub>.

After centrifuging, tubes containing the damp rock samples (for all eight tracers) were dried at 60 °C and 4 cm<sup>3</sup> propan-2-ol added. The tubes were shaken and the screw tops secured. After leaving for 16 hours, an aliquot of the propan-2-ol was removed and analysed for the element. In the case of Sn and Mo, which were equilibrated together, analysis was carried out by ICP-MS. The remaining six elements were analysed using the following radiometric techniques:

- <sup>95m</sup>Tc, <sup>75</sup>Se and <sup>152</sup>Eu by gamma spectrometry, and
- <sup>237</sup>Np, <sup>233</sup>U and <sup>238</sup>Pu by alpha spectrometry.

### 3.2.2 Results and discussion

Tab. 3.2 shows the results obtained for the desorption of all of the radioelements into propan-2-ol.

Less than 0.2 % of the Se and U was desorbed, and > 2 % of the Tc. The latter effect is probably due to oxidation of some of the Tc(IV) to pertechnetate, TcO<sub>4</sub><sup>-</sup>, which is known to extract into many organic solvents (BOYD & LARSON 1983).

2 – 4 % of Eu and Pu were desorbed from the mylonite into propan-2-ol, and 0.5 % of Np.

Tab. 3.2: Results of the propan-2-ol desorption experiments with 3 rock types

Element	Species	Code	Rock	Initial activity sorbed on rock [Bq]	Activity desorbed in propan-2-ol [Bq]	% desorbed
Tc	Tc <sup>4+</sup>	TcIV B	Granodiorite	6.89 × 10 <sup>4</sup>	1.56 × 10 <sup>3</sup>	2.26
		TcIV C	Granodiorite	7.15 × 10 <sup>4</sup>	7.24 × 10 <sup>2</sup>	1.01
Se	SeO <sub>3</sub> <sup>2-</sup>	Se B	Sandstone	3.21 × 10 <sup>5</sup>	5.84 × 10 <sup>2</sup>	0.18
		Se C	Sandstone	2.98 × 10 <sup>5</sup>	9.67 × 10 <sup>1</sup>	0.03
U	UO <sub>2</sub>	UVI B	Granodiorite	1.59 × 10 <sup>2</sup>	1.43 × 10 <sup>-1</sup>	0.09
		UVI C	Granodiorite	1.69 × 10 <sup>2</sup>	9.50 × 10 <sup>-2</sup>	0.06
Eu	Eu <sup>3+</sup>	EuT1	Mylonite	4.18 × 10 <sup>3</sup>	7.23 × 10 <sup>1</sup>	1.73
		EuT2	Mylonite	3.95 × 10 <sup>3</sup>	1.62 × 10 <sup>2</sup>	4.10
Pu	Pu <sup>4+</sup>	PuT1	Mylonite	1.90 × 10 <sup>1</sup>	3.90 × 10 <sup>-1</sup>	2.05
		PuT2	Mylonite	1.90 × 10 <sup>1</sup>	3.90 × 10 <sup>-1</sup>	2.05
Np	NpO <sub>2</sub> <sup>2+</sup>	NpT1	Mylonite	4.28	2.0 × 10 <sup>-2</sup>	0.47
		NpT2	Mylonite	4.23	2.4 × 10 <sup>-2</sup>	0.57
Sn	Sn <sup>4+</sup>	SMT1	Mylonite	1.15 × 10 <sup>4</sup>	3.9 × 10 <sup>1</sup> *	0.34
		SMT2	Mylonite	1.14 × 10 <sup>4</sup>	3.0 × 10 <sup>1</sup> *	0.26
Mo	MoO <sub>4</sub> <sup>2-</sup>	SMT1	Mylonite	see footnote <sup>10</sup>	2.1 × 10 <sup>1</sup> *	
		SMT2	Mylonite	see footnote <sup>7</sup>	2.0 × 10 <sup>1</sup> *	

\* non-radioactive species used

<sup>10</sup> When attempting to 'load' the mylonite with Mo, very little Mo sorbed. This is believed to be due to the anionic speciation of the Mo and resulted in considerable uncertainty in measurement of the amount of Mo desorbed (likely maximum of only 0.5 %).

Sn sorbed moderately strongly onto the mylonite, suggesting cationic or neutral speciation under Grimsel groundwater conditions. Rd values were  $6 \times 10^3$  and  $4 \times 10^3 \text{ cm}^3 \text{ g}^{-1}$  in the two experiments performed.  $\sim 0.3 \%$  was desorbed from the mylonite into propan-2-ol.

### 3.2.3 Conclusions

From the experimental study it was concluded that desorption from rock into propan-2-ol does not occur to a significant degree for Se, U, Np, Sn and Mo. A small but significant degree of desorption occurred in the case of Tc, Eu and Pu.

## 3.3 Sorption of tracers onto experimental equipment

*G.M.N. Baston, J.A. Berry, M. Brownsword and P. Oliver*

Many of the tracers which will be introduced into the site sorb so strongly that they are liable to sorb onto the injection equipment and thus may never actually enter the experimental shear zone. Indeed, scoping experiments carried out within the MI project showed significant sorption for several tracers on parts of the injection apparatus (T. FIERZ, pers. comm. 1994). It was thus decided to carry out controlled experiments on representative samples of all of the materials used in the injection (and extraction) equipment to assess more fully the potential implications to EP.

### 3.3.1 Methodology

The five materials supplied for study were:

- i) Silicon rubber bungs
- ii) Epoxy resin cylinders
- iii) Stainless steel pipe connectors
- iv) Teflon tubing
- v) Polyamide tubing.

The tubing, resin and rubber were cut into pieces for the experiments (approximate geometric surface area per experiment:  $4.5 \text{ cm}^2$ ,  $21.8 \text{ cm}^2$  and  $29 \text{ cm}^2$ , respectively) but one complete stainless steel connector was used per experiment (approximate geometric surface area  $30 \text{ cm}^2$ ).

The above materials were washed with synthetic Grimsel groundwater (see BAJO et al. 1989, AKSOYOGLU et al. 1991 for details) and each sample mixed with  $20 \text{ cm}^3$  spiked synthetic groundwater. The experiments were carried out in duplicate and two concentrations of each radionuclide were studied.

The Tc used also contained Tc-97m, and the Se-75 contained natural Se as carrier. Care was taken to use very low concentrations to ensure that the solubility limit at pH 9.6 was not exceeded. In terms of molarity of each element studied (all isotopes), the initial concentrations were:

- |       |    |                       |     |                       |    |
|-------|----|-----------------------|-----|-----------------------|----|
| i)    | Tc | $3.9 \times 10^{-10}$ | and | $9.0 \times 10^{-11}$ | M  |
| ii)   | Eu | $1.6 \times 10^{-10}$ | and | $3.5 \times 10^{-11}$ | M  |
| iii)  | Se | $1.8 \times 10^{-7}$  | and | $3.7 \times 10^{-8}$  | M  |
| iv)   | U  | $2.7 \times 10^{-7}$  | and | $6.4 \times 10^{-8}$  | M  |
| v)    | Pu | $1.2 \times 10^{-11}$ | and | $2.3 \times 10^{-12}$ | M  |
| vi)   | Np | $3.6 \times 10^{-8}$  | and | $7.1 \times 10^{-9}$  | M  |
| vii)  | Sn | $4.9 \times 10^{-6}$  | and | $1.6 \times 10^{-7}$  | M  |
| viii) | Mo | $2.7 \times 10^{-5}$  | and | $6.8 \times 10^{-6}$  | M. |

Tc, Se and Eu were studied together, since they can readily be counted together by gamma-spectrometry. As in the desorption experiments, Sn and Mo were studied together and determined by ICP-MS, and U, Np and Pu by alpha spectrometry.

In addition to the above experiments, control experiments were also performed without experimental material in order to monitor any sorption on the experimental equipment.

All tubes were gently agitated on a shaker table for 2 months and the pH of each experiment was regularly monitored and adjusted where necessary.

At the end of the 2-month equilibration period, each tube was centrifuged and aliquots were removed and analysed. The remaining solution and sorbing substrate were then carefully removed from each tube, and the latter then rinsed with synthetic Grimsel groundwater. In order to dissolve any radioelement which may have been sorbed onto the walls of the polypropylene centrifuge tubes, 5 cm<sup>3</sup> 4 M nitric acid were added to each tube. Analysis of an aliquot of this solution then enabled a complete distribution of each radioelement to be determined.

### 3.3.2 Results and discussion

Tab. 3.3 shows a summary of the values of  $K_a$  (surface distribution coefficient) for the 8 elements on the 5 materials studied. When calculating  $K_a$  values, the vessel wall sorption was taken into account.

In the case of polyamide tubing, only Sn gave values of  $K_a$  greater than 1 cm<sup>3</sup> cm<sup>-2</sup> for both of the initial concentrations studied. Pu gave values slightly greater than 1 cm<sup>3</sup> cm<sup>-2</sup> at the higher initial concentration only.

For Teflon tubing, as for polyamide, only Sn gave values greater than 1 for both of the initial concentrations studied. One of the two Pu experiments at the higher starting concentration gave a value slightly greater than 1 cm<sup>3</sup> cm<sup>-2</sup>.

For epoxy resin, Pu and Sn again give significant  $K_a$  values, particularly at the higher initial concentrations. In addition, Eu shows stronger sorption onto epoxy resin than onto any of the other materials. One of the Tc and one of the Np  $K_a$  values are also greater than 1 cm<sup>3</sup> cm<sup>-2</sup>.

Between 31.2 % and 45.5 % of the Np sorbed onto the resin. These results contrast with the data in Section 3.1, where under similar conditions, the resin used did not sorb significant amounts of <sup>237</sup>Np, <sup>137</sup>Cs or <sup>60</sup>Co. However, the apparent inconsistency may result from higher surface areas of the small resin pieces used here.

Sn and Pu are relatively strongly sorbed onto silicone rubber at both concentrations studied. Tc and U give  $K_a$  values greater than 1 cm<sup>3</sup> cm<sup>-2</sup> at the higher initial concentration only. One of the Np  $K_a$  values is greater than 1 cm<sup>3</sup> cm<sup>-2</sup>.

Pu is sorbed more strongly onto stainless steel than any of the other materials studied. Sn, Np and U also gave  $K_a$  values in excess of 1 cm<sup>3</sup> cm<sup>-2</sup> for each concentration studied.

In all cases, Mo and Se show the least tendency to sorb. This fact may be linked to their anionic speciation. In a similar study (RABER et al. 1983), Se was significantly sorbed onto neoprene and various steels. These high  $K_a$  values may have been due to precipitation of CaSeO<sub>3</sub> (Ca concentration  $2.2 \times 10^{-4}$  M). <sup>75</sup>Se is not usually obtained carrier-free, so this Ca concentration could have been sufficient to precipitate CaSeO<sub>3</sub>.

Tab. 3.3:  $K_a$  [ $\text{cm}^3 \text{cm}^{-2}$ ] for eight radionuclides on various materials ( $\pm 2 \sigma$ , based on the statistics of analysis alone)

Radio-element	Stainless steel	Silicone rubber	Epoxy resin	Teflon tubing	Polyamide tubing
<b>Tc</b>	$0.15 \pm 0.01$	$1.41 \pm 0.04$	$1.44 \pm 0.05$	$0.52 \pm 0.01$	$0.21 \pm 0.01$
	$0.25 \pm 0.01$	$1.06 \pm 0.04$	$0.95 \pm 0.03$	$0.49 \pm 0.01$	$0.13 \pm 0.01$
	$0.35 \pm 0.06$	$0.30 \pm 0.02$	$0.30 \pm 0.02$	$0.26 \pm 0.02$	$0.20 \pm 0.01$
	$0.34 \pm 0.03$	$0.31 \pm 0.07$	$0.31 \pm 0.02$	$0.27 \pm 0.02$	$0.25 \pm 0.02$
<b>Se</b>	$0.16 \pm 0.01$	< 0.06	< 0.01	< 0.01	< 0.01
	$0.17 \pm 0.01$	< 0.06	< 0.01	< 0.01	< 0.01
	$0.12 \pm 0.01$	< 0.06	< 0.02	< 0.01	< 0.01
	$0.11 \pm 0.01$	< 0.06	< 0.02	< 0.01	< 0.01
<b>U</b>	$3.41 \pm 0.43$	$1.87 \pm 0.24$	$0.04 \pm 0.07$	$0.44 \pm 0.07$	$0.10 \pm 0.04$
	$4.58 \pm 0.58$	$3.02 \pm 0.39$	$0.54 \pm 0.08$	$0.55 \pm 0.08$	$0.64 \pm 0.01$
	$1.89 \pm 0.32$	$0.41 \pm 0.07$	$0.50 \pm 0.09$	$0.08 \pm 0.05$	< 0.01
	$1.80 \pm 0.39$	$0.46 \pm 0.07$	$0.80 \pm 0.13$	$0.22 \pm 0.06$	$0.25 \pm 0.06$
<b>Eu</b>	$0.51 \pm 0.01$	$0.41 \pm 0.01$	$4.32 \pm 0.13$	$0.17 \pm 0.01$	$0.09 \pm 0.01$
	$0.53 \pm 0.02$	$0.29 \pm 0.01$	$4.52 \pm 0.14$	$0.17 \pm 0.01$	$0.12 \pm 0.01$
	$0.90 \pm 0.06$	$0.48 \pm 0.01$	$3.02 \pm 0.14$	$0.45 \pm 0.01$	$0.45 \pm 0.01$
	$0.74 \pm 0.05$	$0.68 \pm 0.04$	$2.60 \pm 0.13$	$0.59 \pm 0.02$	$0.36 \pm 0.01$
<b>Np</b>	$10.99 \pm 1.44$	$0.53 \pm 0.11$	$0.63 \pm 0.09$	$0.18 \pm 0.04$	$0.53 \pm 0.08$
	$7.47 \pm 1.26$	$0.50 \pm 0.07$	$0.87 \pm 0.11$	$0.06 \pm 0.03$	$0.85 \pm 0.11$
	$6.41 \pm 1.82$	$0.27 \pm 0.05$	$0.52 \pm 0.08$	$0.13 \pm 0.05$	$0.60 \pm 0.01$
	$4.02 \pm 0.62$	$2.03 \pm 0.34$	$1.19 \pm 0.19$	$0.13 \pm 0.05$	$0.23 \pm 0.05$
<b>Pu</b>	$21.06 \pm 2.47$	$5.72 \pm 0.70$	$20.1 \pm 2.64$	$1.13 \pm 0.15$	$1.24 \pm 0.17$
	$26.28 \pm 2.98$	$5.27 \pm 1.09$	$7.67 \pm 1.03$	$0.75 \pm 0.10$	$1.39 \pm 0.18$
	$60.30 \pm 8.79$	$24.88 \pm 3.44$	$5.42 \pm 0.67$	$0.39 \pm 0.07$	$0.70 \pm 0.10$
	$31.75 \pm 4.36$	$17.98 \pm 2.38$	$5.74 \pm 0.72$	$0.27 \pm 0.06$	$0.48 \pm 0.08$
<b>Sn</b>	$2.46 \pm 0.27$	$3.11 \pm 0.34$	$3.73 \pm 0.40$	$1.76 \pm 0.20$	$2.79 \pm 0.30$
	$2.64 \pm 0.28$	$6.43 \pm 0.69$	$3.31 \pm 0.35$	$1.99 \pm 0.22$	$5.26 \pm 0.57$
	$2.05 \pm 0.42$	$1.44 \pm 0.29$	$1.12 \pm 0.23$	$2.93 \pm 0.61$	$3.33 \pm 0.68$
	$2.20 \pm 0.45$	$0.40 \pm 0.09$	$0.90 \pm 0.19$	$1.85 \pm 0.38$	$1.23 \pm 0.26$
<b>Mo</b>	$0.08 \pm 0.02$	$0.05 \pm 0.02$	$0.10 \pm 0.03$	$0.07 \pm 0.04$	$0.13 \pm 0.04$
	$0.04 \pm 0.02$	$0.05 \pm 0.02$	< 0.05	$0.07 \pm 0.04$	$0.07 \pm 0.04$
	< 0.05	$0.04 \pm 0.02$	$0.06 \pm 0.03$	$0.03 \pm 0.04$	$0.08 \pm 0.04$
	< 0.05	$0.04 \pm 0.02$	< 0.05	$0.05 \pm 0.04$	< 0.08

### 3.3.3 Conclusions

It is clear from the experimental results that significant retardation of some radionuclides will potentially arise from sorption on experimental equipment, especially stainless steel and silicon rubber. Pu and Sn are the most vulnerable of the radionuclides tested. These results prompted the subsequent development of a novel, down-hole injection technique (see FIERZ 1997) for use in the final field experiment.

### 3.4 Effect of sorption kinetics

*G.M.N. Baston, J.E. Berry and M. Brownsword*

During the MI experiment, it was noted that, for some tracers, there was a definite kinetic hindrance to sorption. In particular, this was noted for Cs in both the laboratory and in the field (BRADBURY & BAEYENS 1992, SMITH et al. 2001b). Scoping experiments with Tc in the migration shear zone also indicated likely kinetic effects (U. FRICK, pers. comm. 1994).

It thus seemed prudent to check the likely EP tracer cocktail for similar effects, especially as the experiment was to be conducted in the 1.7 m flowfield where residence times are around a couple of hours for non-sorbing tracers (FRICK et al. 1992, SMITH et al. 2001b). A literature review indicated little data of relevance to the short timescales of concern and it was therefore decided to carry out a few scoping experiments on the tracer cocktail to assess the potential problems of minimal tracer retention due to kinetic effects. Due to time and budget constraints, only six members of the tracer cocktail, Tc, Co, Np, U, Se and Eu, could be studied.

#### 3.4.1 Methodology

10 g samples of ground, sieved (250 µm) Grimsel mylonite (from shear zone AU126) were mixed with 1 L of 'spiked' synthetic Grimsel groundwater and agitated gently. Sodium dithionite was used to provide reducing conditions. <sup>232</sup>U and <sup>237</sup>Np were studied together in one set of duplicate experiments, and <sup>95m</sup>Tc, <sup>60</sup>Co, <sup>75</sup>Se and <sup>152</sup>Eu in another set. The pH of the groundwater was adjusted to 9.6 after addition of the spike.

For each of the experiments, sampling took place every 7.5 minutes during the first hour, every 15 minutes during the second hour, then hourly to a total of 10 hours.

When calculating  $K_d$ , allowance was made for the removal of liquid for determination of the initial activity, for the decrease in radioactivity after each sampling, and also for the small change in water-to-rock ratio following removal of 7 mL (0.45 µm filtered) liquid at each sampling.

The following formulae were used to calculate  $K_d$  [ $\text{cm}^3 \text{g}^{-1}$ ]:

$$A_t = [(C_{t-1} - C_t) V] + A_{t-1} \quad (\text{Eq. 3.1})$$

$$K_d = \frac{A_t}{C_t \cdot m} \quad (\text{Eq. 3.2})$$

where

- $A_t$ : Activity on solid after time t [Bq]
- $A_{t-1}$ : Activity on solid at time of previous sampling [Bq]
- $V$ : Volume of solution [ $\text{cm}^3$ ]
- $m$ : Mass of solid [g]
- $C_t$ : Concentration in solution [ $\text{Bq cm}^{-3}$ ]
- $C_{t-1}$ : Concentration in solution at time of previous sampling [ $\text{Bq cm}^{-3}$ ]

Note that there were suspected filter failures in one of the experiments involving  $\gamma$ -emitters (the samples taken after 7 and 8 hours – see Tab. 3.4).

### 3.4.2 Results and discussion

Tab. 3.4 shows the value of the calculated distribution ratio,  $K_d$ , obtained for each sampling period for each of the six radionuclides, and Fig. 3.1 to 3.6 plot the solution activity against time.

Tab. 3.4:  $K_d$  [ $\text{cm}^3 \text{g}^{-1}$ ] with time for six radionuclides in contact with crushed mylonite (duplicate A and B experiments for alpha and gamma-emitters)

Elapsed Time [hrs]	Tc		Co		Np		U		Se		Eu	
	$\gamma$ -A	$\gamma$ -B	$\gamma$ -A	$\gamma$ -B	$\alpha$ -A	$\alpha$ -B	$\alpha$ -A	$\alpha$ -B	$\gamma$ -A	$\gamma$ -B	$\gamma$ -A	$\gamma$ -B
0.13	120	25	0	33	85	0	70	69	5	0	0	230
0.25	150	0	78	47	140	0	81	150	46	0	300	290
0.38	0	0	67	45	220	0	95	110	2	0	360	330
0.50	0	0	68	49	270	0	120	120	12	0	390	370
0.63	86	8	86	47	100	0	110	100	35	0	440	420
0.75	15	140	75	47	63	0	130	140	17	1	470	470
0.88	180	78	99	52	15	79	150	150	64	3	520	500
1.00	100	110	99	54	6	6	150	150	42	0	550	530
1.25	97	69	100	51	63	0	160	150	31	0	600	580
1.50	30	0	90	56	3	110	170	170	25	0	670	620
1.75	26	53	100	65	11	77	180	180	17	0	740	740
2.00	28	73	100	67	220	26	200	190	17	1	800	740
3.00	58	8	130	67	11	26	220	210	26	0	1000	910
4.00	26	0	130	80	0	16	220	240	17	0	1200	1000
5.00	12	0	130	80	210	0	230	230	10	0	1400	1100
6.00	0	0	140	120	260	0	240	240	0	0	1600	1700
7.00	0	a)	150	a)	260	0	250	250	0	a)	1700	a)
8.00	0	a)	150	a)	260	100	270	280	0	a)	2000	a)
9.00	0	0 <sup>b)</sup>	140	130 <sup>b)</sup>	63	0	250	290	57	0 <sup>a)</sup>	2200	1700 <sup>b)</sup>
10.00	0	0 <sup>b)</sup>	150	104 <sup>b)</sup>	63	0	430	280	0	0 <sup>a)</sup>	2300	1700 <sup>b)</sup>

$K_d$  corrected for small change in water-to-rock ratio and small reduction in radioactivity as samples were removed (complete raw laboratory data see BASTON et al. 1995)

a) Suspected filter failure in  $\gamma$ -B experiment.

b)  $K_d$  uncorrected due to above.

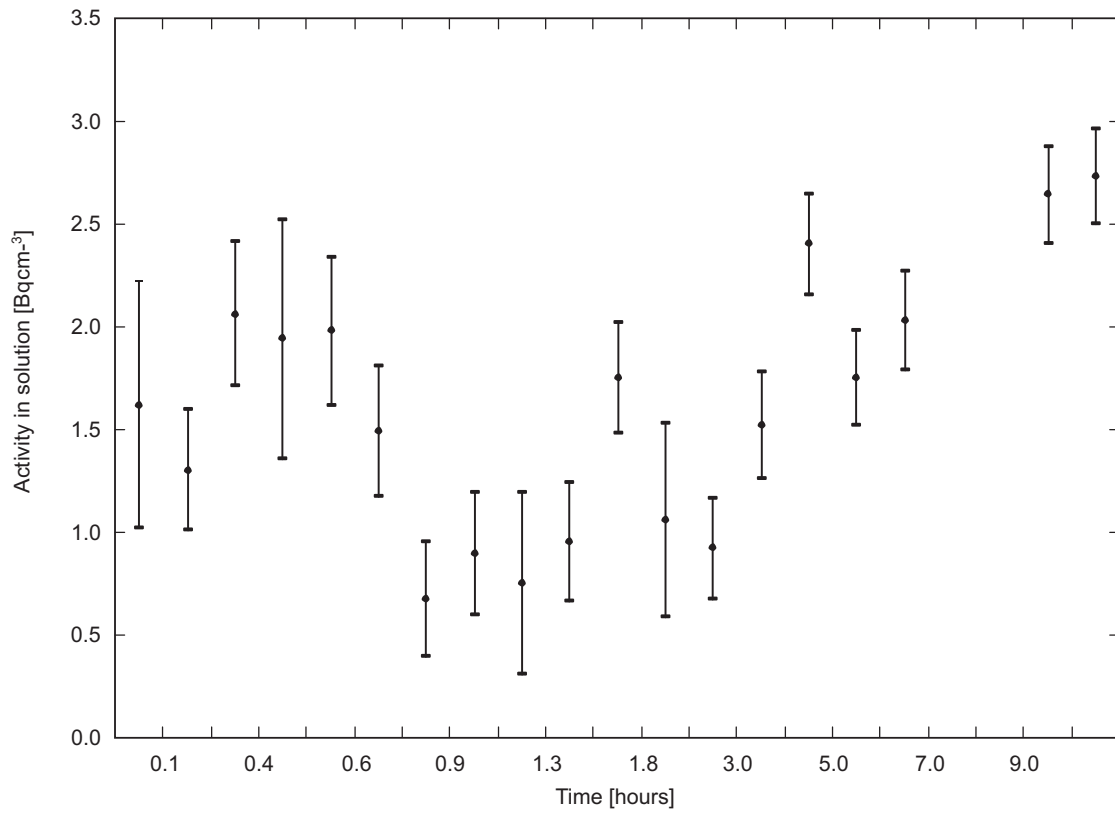


Fig. 3.1: Technetium sorption kinetics

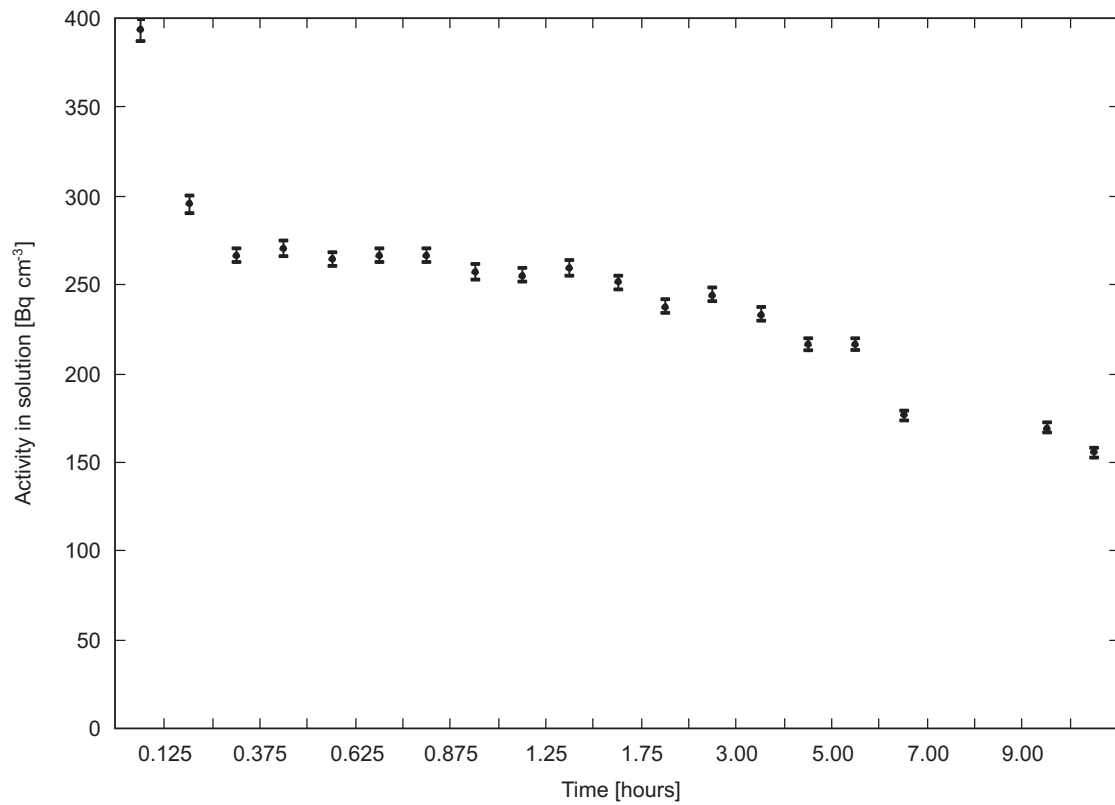


Fig. 3.2: Cobalt sorption kinetics

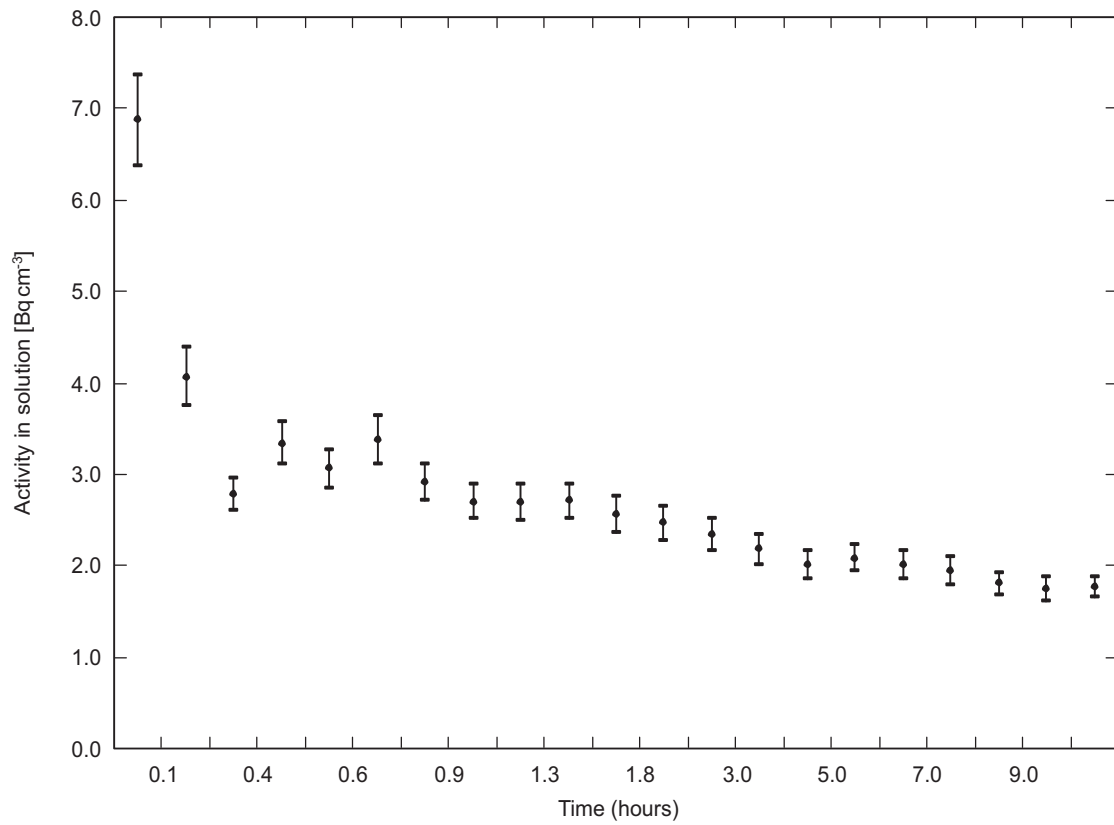


Fig. 3.3: Uranium sorption kinetics

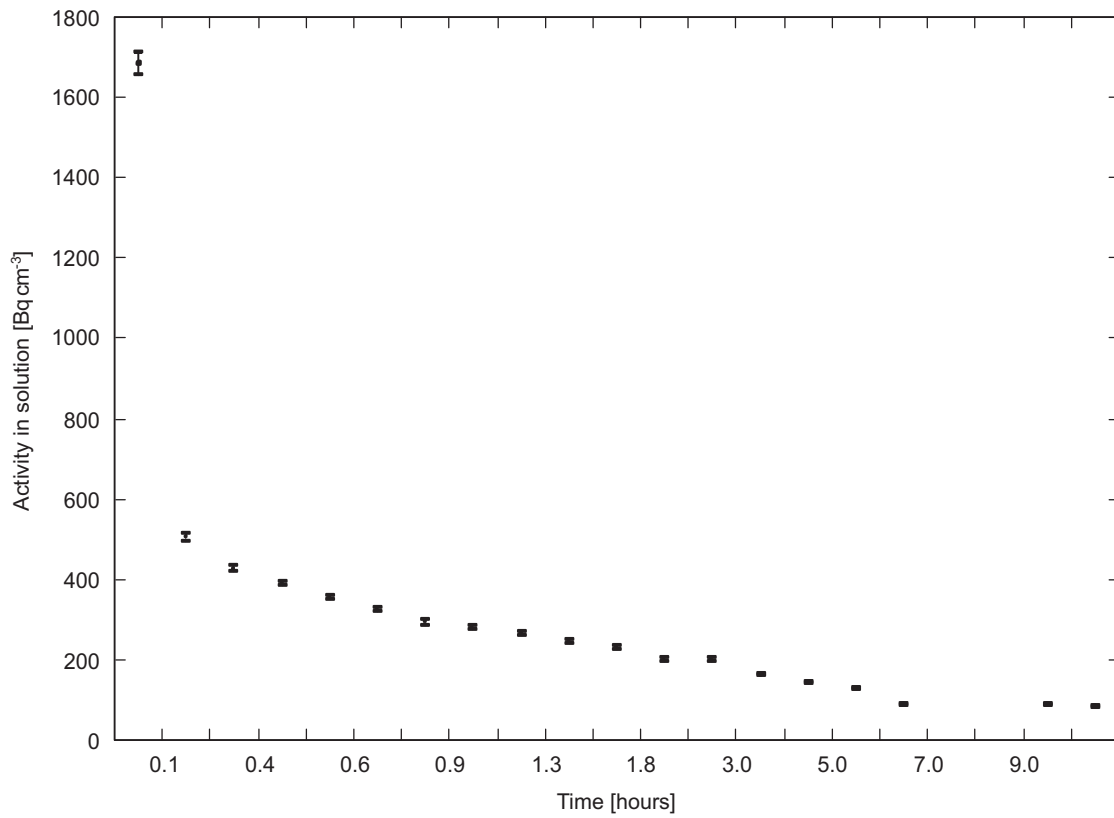


Fig. 3.4: Europium sorption kinetics

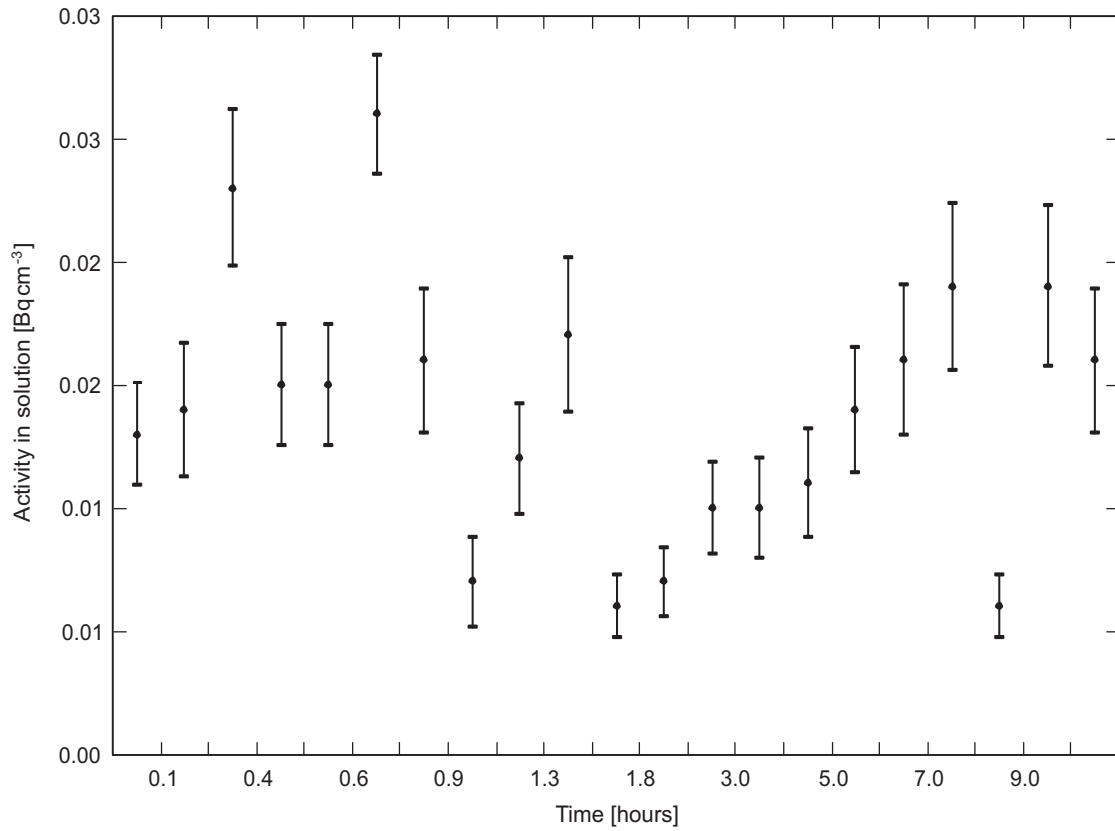


Fig. 3.5: Neptunium sorption kinetics

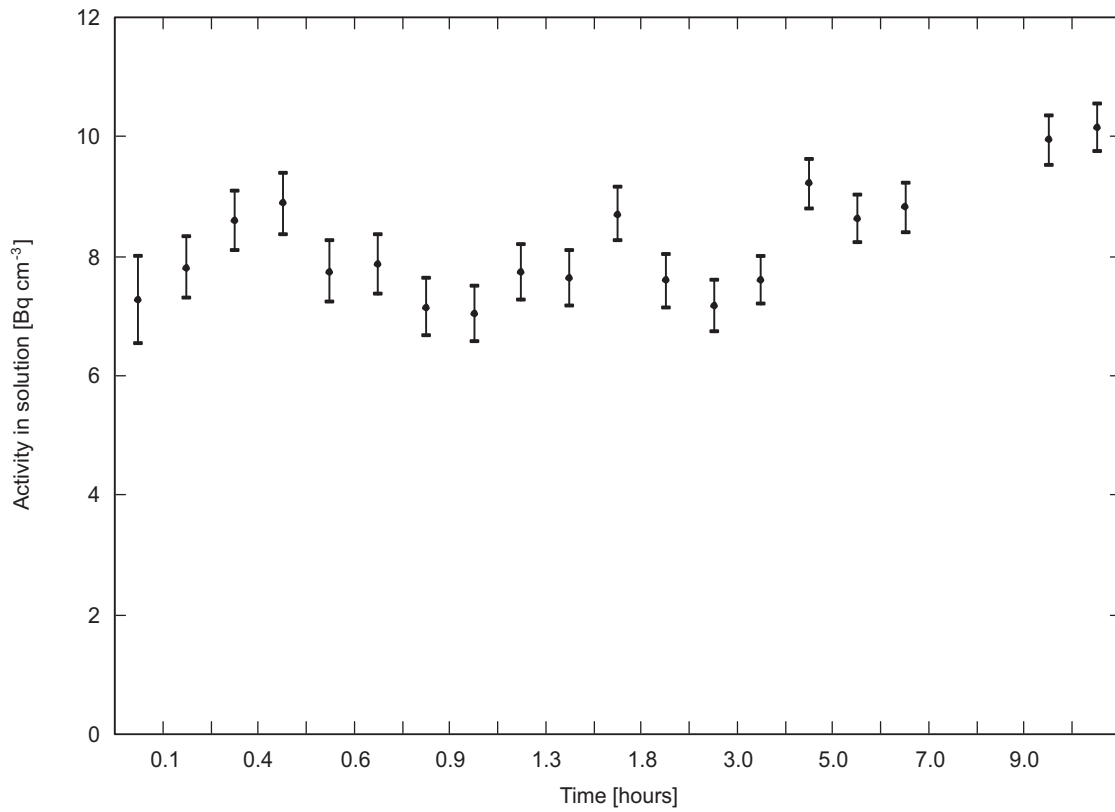


Fig. 3.6: Selenium sorption kinetics

Steady increases in  $K_d$  were observed for Co, U and Eu over the 10-hour experiments (Tab. 3.4). In the case of Tc, there was an apparent decrease in sorption in the last 5 or 6 hours of the experiment. The activity remaining in solution was apparently higher than the initial activity in both of the experiments (Fig. 3.1). One possible explanation of this is that the Tc was present in a colloidal form where the particles were small enough to pass through the 0.45  $\mu\text{m}$  filters. A further complication was the low initial concentration of  $^{95\text{m}}\text{Tc}$  used. The short timescales for these experiments meant that the existing limited stock of  $^{95\text{m}}\text{Tc}$  (half-life 60 days) had to be used but despite this, the initial concentration was still less than ten times the detection limit in both experiments.

Measurement of Np sorption was hampered by the necessity of using a starting concentration of  $^{237}\text{Np}$  (half-life  $2.14 \times 10^6$  years) below its solubility limit despite the low specific activity. This meant the use of a solution containing only tens of mBq of  $^{237}\text{Np}$  per mL. Even after a 20-hour count, the  $^{237}\text{Np}$  peak is only just discernible above the background.

For Se, as was the case for Tc, there is experimental scatter in the results. The general conclusion concerning Se is that there was no significant sorption.

### 3.4.3 Conclusions

Co, U and Eu show clear sorption kinetics (Fig. 3.2, 3.3 and 3.4 respectively) but all approach equilibrium within the timescale of concern (2 – 3 hours) of the field experiment. Indeed, as the majority of the observed uptake occurs in the first 15 minutes<sup>11</sup> or so, it is unlikely that any significant kinetic hindrance to sorption is to be expected under field conditions.

Se and Np show no obvious trends (although this may be partially due to experimental restrictions in the case of Np) and the Tc data suggest the presence of Tc colloids in solution.

---

<sup>11</sup> Sorption half-times were calculated at 5 – 6 minutes for Eu, 20 – 45 minutes for U and 1 – 5.5 hours for Co.

## 4 Assessment of analytical techniques

Following excavation of the experimental shear zone, it is intended to define the radionuclide tracer distribution by means of a suite of surface analytical and radiochemical techniques. Although none of the techniques which may be employed are novel, many of the specific applications are somewhat unusual and thus it was deemed prudent to carry out initial scoping tests to check the suitability of the various methods (see Fig. 4.1). Two surface techniques were identified as candidates for chemical analysis: SIMS and LAM-ICP-MS.

### 4.1 SIMS analysis of Grimsel rock samples

*A. Brown*

At this period in the project, the form of shear zone immobilisation was still under consideration and it was therefore important to assess different types of rock samples. The overall aim was to provide information on the potential for using secondary ion mass spectrometry (SIMS) to obtain elemental distributions from mineral grains with surfaces of various degrees of roughness as, at this stage, there was no guarantee that polished specimens would be available.

Several aspects of the use of SIMS were examined:

- Broad area SIMS analysis
- Investigation of the limits for broad area rastering of the primary ion beam during elemental mapping to facilitate identification of points of high elemental yield for subsequent analysis
- Surface roughness
- Examination of the effects of varying surface roughness by a comparison of the secondary ion emission from rock powder samples
- Charge neutralisation
- Assessment of the relative ease of charge neutralisation between rock powder and rock face surfaces
- Sample requirements
- Assessment of the requirements for sample mounting and preparation prior to analysis, including consideration of the suitability of fluoresceine-containing epoxy resin for the dispersal and stabilisation of rock samples
- Outgassing of samples
- Investigation of outgassing properties of the epoxy resin prior to analysis.

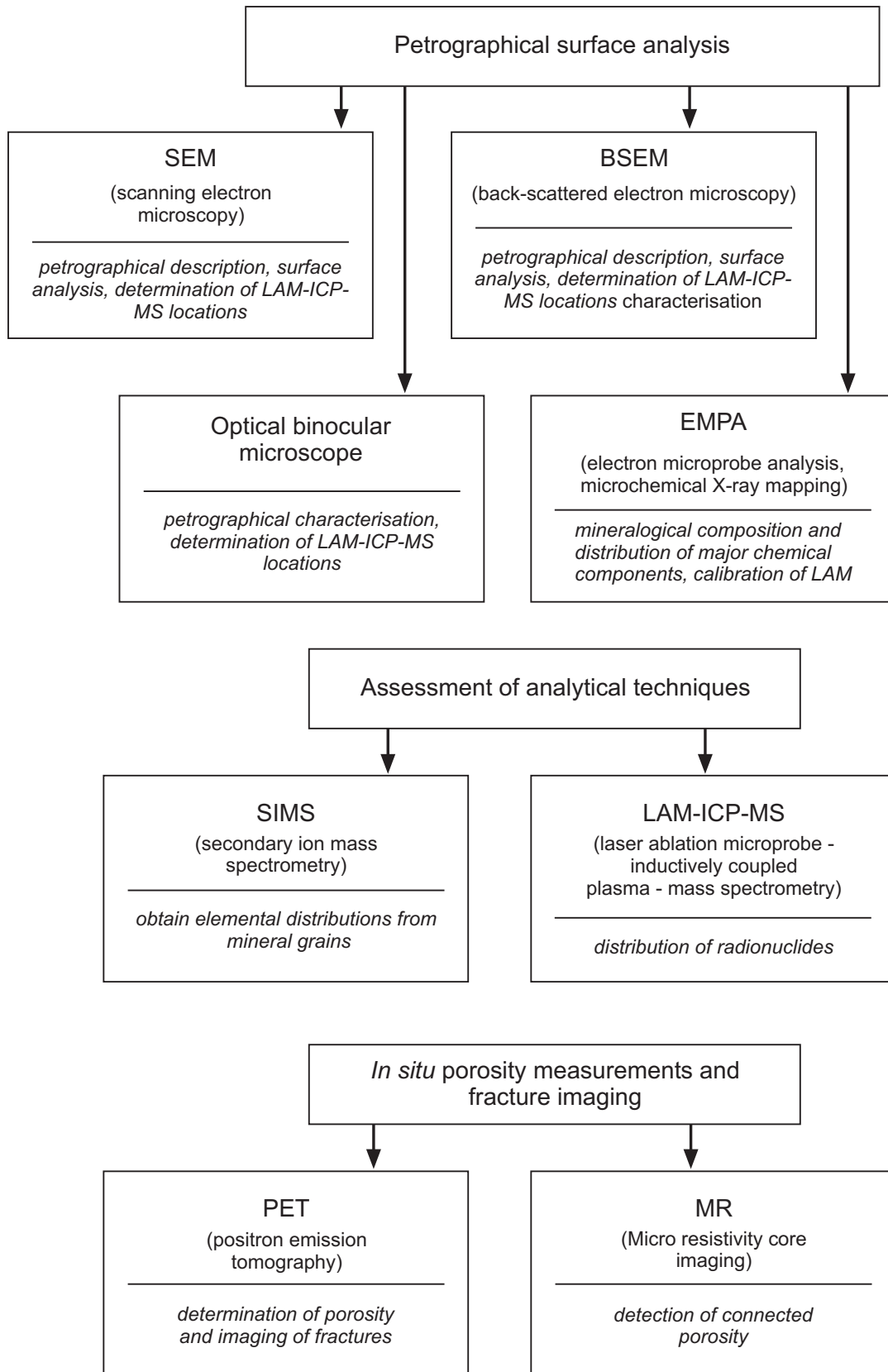


Fig. 4.1: Overview of the analytical techniques tested within the project

#### 4.1.1 Samples

Four samples were used in the study:

- Mylonite M2 – solid rock sample
- Granodiorite G2 – solid rock sample
- Synthetic fault gouge S2 – powdered rock sample
- Natural fault gouge N2 – powdered rock sample.

All samples were in the form of a 1 cm<sup>3</sup> cube encapsulated in epoxy resin on five sides, with the surface of interest left resin-free.

The significant odour associated with the epoxy resin, particularly with the fault gouge samples, suggested that outgassing problems would arise in the instrument vacuum chamber.

After surface cleaning with a jet of dry nitrogen to remove loose surface particles and adventitious material from handling and sawing, the samples were examined under an optical microscope. From this it was clear that the synthetic fault gouge material (S2) had an extremely rough surface which would potentially cause problems during analysis due to the relatively large number of macroscopic topographic features. The natural fault gouge (N2) had a more uniform surface, topographically, and the mylonite (M2) and granodiorite (G2) appeared to have large areas of relatively flat surface giving potentially better surfaces for SIMS analysis.

As anticipated, outgassing caused a higher than normal pressure in the instrument vacuum chamber ( $1 \times 10^{-6}$  mbar compared to ideal conditions  $< 1 \times 10^{-8}$  mbar) and it is recommended that future samples be loaded at least 12 hours prior to analysis in the entry lock to minimise outgassing in the analysis chamber.

#### 4.1.2 Results and discussion

##### M2 – mylonite

The main species of interest were found from the initial SIMS spectrum to be Li<sup>+</sup>, Na<sup>+</sup>, Mg<sup>+</sup>, Al<sup>+</sup>, Si<sup>+</sup>, K<sup>+</sup>, Ca<sup>+</sup> and Fe<sup>+</sup>. In secondary ion images recorded over large areas (about 2 mm × 2 mm), there are clear differences, for example, between the distribution of Na<sup>+</sup> and Li<sup>+</sup>. However, it must be noted that, for SIMS analysis, there is no direct relationship between secondary ion intensity and concentration of a species; samples of broadly similar composition allow semi-quantitative comparisons, particularly if secondary ion intensity ratios are used. A band-like feature across the centre of the large field of view is most probably related to a topographic feature.

The relationship between two or more species can be investigated by the use of overlays of secondary ion images where the two species are denoted by different colours. There is some evidence with this technique of large mineral grains (about 100 – 200 µm) containing Al<sup>+</sup>, Si<sup>+</sup> and K<sup>+</sup> but grain boundaries are indistinct.

##### G2 – granodiorite

The images of the key species (Na<sup>+</sup> and K<sup>+</sup> most intense secondary ions with Al<sup>+</sup>, Si<sup>+</sup>, Mg<sup>+</sup>, Ca<sup>+</sup>, Fe<sup>+</sup> and Li<sup>+</sup>) taken from a 500 µm area showed a very high degree of secondary ion

contrast with the individual grains clearly recognisable along with differences in chemical composition. Some positive correlation could be seen between various species e.g. Na<sup>+</sup>, Al<sup>+</sup> and Si<sup>+</sup>, or K<sup>+</sup> and Fe<sup>+</sup>. There was a tendency towards a negative correlation of Na<sup>+</sup> and K<sup>+</sup> in some areas.

### **N2 – natural fault gouge**

The mass spectrum for N2 showed the presence of the same species as for M2 and G2 but with some differences in relative intensities. For example, Li<sup>+</sup> was significantly more intense than in G2 while Na<sup>+</sup> was relatively less intense.

The Na<sup>+</sup>, Mg<sup>+</sup>, Al<sup>+</sup> and Si<sup>+</sup> secondary ion images (500 µm) all showed the mineral grains clearly defined. Al<sup>+</sup> and Si<sup>+</sup> showed very similar distributions and Fe<sup>+</sup> and Mg<sup>+</sup> also showed areas of positive correlation. As seen previously, there was a negative correlation of Na<sup>+</sup> and K<sup>+</sup> to a certain extent.

Additional images acquired for small fields of view (250 and 125 µm) illustrated the greater difficulty of obtaining satisfactory SIMS signals from this powder sample. Areas of very low secondary ion count are probably caused by severe topographic effects leading to difficulties in obtaining adequate charge neutralisation.

### **S2 – synthetic fault gouge**

The SIMS spectrum of S2 indicates a reduced count rate across the whole region compared to the spectra of the other samples. No significant Li<sup>+</sup> peak is seen and the ratio of Na<sup>+</sup> to Mg<sup>+</sup> is higher than in N2.

The images acquired for 500 µm and 250 µm areas were characterised by large areas of very low signal produced by topographic effects leading to ineffective charge neutralisation. The optical microscope examination of this surface revealed severe topographic features which were predicted to cause problems. In order for the SIMS analysis to be more successful on powder samples, the surface physical structure would need to be flatter and to consist of close packed crystallites. Searching around on the surface of a sample to locate the best, flattest areas is necessarily time-consuming and ensuring better sample preparation is more efficient.

## **4.1.3 Conclusions**

- **Sample requirements**

The size of samples should ideally be 1 cm × 1 cm × 0.2 cm. The initial samples were too thick and subsequent thinning increases the handling and chances for artefacts. Likewise, the use of plastic containers and mounts can cause contamination due to mould release agents.

The presence of the epoxy resin stabilising the samples had no deleterious effect on sample analysis.

- **Outgassing of sample**

The presence of the epoxy resin caused serious problems with outgassing, future samples will require at least 12 hours loaded in the instrument load lock to facilitate outgassing before loading into the analysis chamber.

- Broad area SIMS analysis

Analytical information in the form of mass spectra and secondary ion images can be obtained from areas of at least 2 mm × 2 mm. This facility is dependent on the instrument used.

- Surface roughness

Optical microscopic examination of sample surfaces indicated mylonite and granodiorite had potentially the best surfaces for analysis with natural fault gouge and, particularly, synthetic fault gouge likely to experience problems due to macroscopic topographic features. Subsequent SIMS analysis confirmed these observations: M2 and G2 yielding satisfactory data while N2 and S2 were less successful. Preparation or selection of flatter surfaces is recommended for further work on powder samples.

- Charge neutralisation

Charge neutralisation of samples M2 and G2 was relatively straightforward with no problems encountered decreasing field size from 2.5 mm down to 125 µm. In contrast, powder samples were restricted by the presence of topographic features which inhibited satisfactory charge neutralisation, especially at smaller areas.

In summary, non-polished samples will almost certainly be problematic to analyse whereas epoxy impregnated samples, while difficult, will be possible if outgassed before analysis.

## 4.2 Evaluation of LAM-ICP-MS analysis of doped rock samples

*M.T. Styles, A.E. Milodowski, S.R. Chenery, D.J. Bland and M.R. Gillespie*

As mentioned previously, the intact, cored, shear-zone will be examined in detail to determine and quantify the distribution of the various tracer elements. As part of the evaluation of potential analytical techniques, the use of the laser ablation microprobe – inductively coupled plasma – mass spectrometry (LAM-ICP-MS) technique to determine the distribution of tracer elements in laboratory-doped test samples was investigated. In addition, it was decided that the samples examined here should be non-standard (i.e. non-polished surfaces) to assess the effect on analysis. The study was undertaken in three stages: first a general petrographical characterisation of the samples by optical and electron microscopes, second, examination and analysis by electron microprobe and finally, LAM-ICP-MS was carried out.

### 4.2.1 Samples

Four types of material were prepared, either based on samples taken from representative parts of the experimental shear zone in the GTS or simulated material representing shear zone rocks. The test materials prepared include:

- Natural fault gouge
- Synthetic fault gouge
- Natural mylonite (orientated mylonite)
- Grimsel Granodiorite

Test materials were prepared as rough-cut cubes of rock with approximately 1 cm dimensions. The blocks of granodiorite and natural mylonite were encased, apart from the surface to be studied, within epoxy resin and mounted with epoxy resin within a small plastic pot with a removable cover. The friable natural and synthetic fault gouge samples were prepared as approximately 1 cm cube blocks, after initially impregnating the materials with one of the epoxy resins (Resin no. 5, see Chapter 2) which were under assessment for the final field experiment. Each block was encased in epoxy resin and mounted as the granodiorite and mylonite samples.

After preparation, the exposed surface on each of the test samples was doped (by PSI – see Appendix A) by immersion in solutions containing various mixtures of the following:  $^{242}\text{Pu}$ ,  $^{233}\text{U}$ ,  $^{99}\text{Tc}$ ,  $^{237}\text{Np}$ , Sn, Eu, Mo and Se.

#### 4.2.2 Petrographical characterisation

Each sample was observed and photographed under an optical binocular microscope. The photographs subsequently were used to locate analysis areas for LAM-ICP-MS. With additional information from electron microscope observation, the mineralogy of the surfaces was also determined.

##### Granodiorite

The accessible surface of most of the blocks was composed mainly of quartz and K-feldspar, with lesser amounts of albite, and minor to major amounts of biotite and muscovite. Trace amounts of chlorite, apatite, magnetite, ilmenite, zircon, sphene and, rarely, epidote were also observed. However, only quartz, feldspar, biotite and muscovite were exposed in sufficient quantity and with a large enough grain size, for them to be reliably identified and located under the high-power reflected light optics system of the LAM-ICP-MS (which has only a very limited optical depth of field) in any practical manner, given the very high surface relief of most samples. Whilst all of the samples examined are mineralogically similar to the granodiorite blocks, the exposed surfaces vary significantly between samples. The exposed surfaces are clearly unrepresentative of the granodiorite as whole. This is because the block size (typically 2 – 2.5 cm cubes) used is comparable to the grain-size of the granodiorite – i.e. in some blocks, the quartz, biotite and K-feldspar crystals are up to 1 – 2 cm across. In extreme cases, block surfaces are virtually all feldspar with minor quartz and micas (e.g. Sn-doped sample: Sn4G17; see Appendix A for details of the samples), whilst other samples may expose virtually only quartz (e.g. Pu-doped sample: Pu4G4) and others have surfaces which expose large areas of biotite or muscovite (e.g. U-doped sample: U4G22). Consequently, since all the granodiorite samples provided were individually 'spiked' with a single tracer, it was not possible to make any meaningful comparisons of the total element loading on sample surfaces, or interpret tracer uptake from solution. In addition to variations in surface mineralogy between the blocks, some block surfaces were heavily contaminated with epoxy resin.

The particular solid-state back-scattered electron detector used appears to work reasonably well with these materials and, despite the extreme sample topography, has proven very useful in identifying the distribution of mineral phases in the sample surface. BSEM observations revealed that the surface mineralogy is far more complex than could be discerned from optical microscopic study of the rough surfaces. An area of one granite block surface (Tc-doped sample Tc4G14) appeared, from optical examination, to be a relatively homogeneous, single K-feldspar crystal. However, the BSEM photomicrograph quite clearly distinguished the presence of coarse K-feldspar with quartz and albite, further complicated by the presence of exsolution blebs of albite within the K-feldspar. BSEM also showed that the biotite and muscovite crystals exposed

in the sample surfaces are often finely intergrown and interlaminated admixtures of both minerals, rather than discrete single mineral grains.

SEM analysis showed that most mineral surfaces were contaminated with fine (< 5  $\mu\text{m}$ ) mineral dusts of the host granodiorite, and were presumably derived from the granodiorite during sample preparation. However, the presence of these particles on the sample surface will complicate any interpretation of tracer uptake, since the tracers could be sorbed onto these particles as well as onto the intact rock surface. Since LAM-ICP-MS ablation areas/volumes are larger than these particles, ablation data will inevitably include trace element contributions from both these particles and the underlying mineral. SEM also revealed that exposed mica grains (biotite and muscovite) were extensively exfoliated along the basal (001) cleavage. The exfoliated mica sheets are distorted and the deformation is probably the result of mechanical damage during sample handling and this will have exposed internal mineral surfaces (001-cleavage surfaces) to the tracer solutions during the experiments.

Fractured feldspars displayed stepped surfaces developed by fracturing along intersecting cleavage planes. These surfaces usually display some microporosity with pores occurring as pits and cavities in the surface. Pore sizes range from < 0.1 to 2  $\mu\text{m}$  in diameter, but are volumetrically less significant than the internal cleavage surfaces displayed by mica crystals. However, sorption on these surfaces would also have to be taken into account in interpreting SIMS depth profiles for tracer elements, since SIMS analysis generally consider broad areas (typically 20 – 100  $\mu\text{m}^2$ ) of the mineral surface rather than point analyses. Quartz surfaces appear to be very simple and typically display conchoidal fracture surfaces and crystal grain boundaries. In general, little surface porosity was visible.

The mineral intergrowth, surface dust contamination and internal porosity (in micas) will complicate interpretation of any LAM-ICP-MS. It is envisaged that this problem would similarly affect the use of other techniques such as secondary ion mass spectrometry (SIMS) which also rely largely on optical microscopy for mineral location and identification.

### **Mylonite samples**

Most mylonite blocks were prepared by cleaving (splitting) along the foliation plane of the rock. The exposed surface of the block therefore represents the cleavage / foliation plane. Despite the development of mineralogically distinct bands parallel to the foliation, most of the mylonite surfaces exposed on the samples are dominated by intergrowths of muscovite and biotite because the samples have preferentially split along the weaker micaceous bands. Consequently, most sample surfaces comprise intergrown flakes of biotite and muscovite presenting 001-cleavage planes to the sample surface. As in the case of the granodiorite samples, the micas have been mechanically damaged and display significant exfoliation and this will therefore have exposed internal cleavage surfaces to the tracer solutions during doping experiments.

Two samples (Pu-doped sample Pu2M2 and Np-doped sample Np2M2) presented surfaces which were perpendicular to the foliation of the rock. In these samples, quartz- and feldspar-rich regions were more readily located and distinguished.

### **Natural fault gouge samples and synthetic fault gouge samples**

Both of these materials appeared to be very similar in character. In all cases, the surface relief was severe. This created major depth-of-focus problems for optical microscope observation and made location of analysis points under the LAM-ICP-MS virtually impossible, except for very

large quartz grains. SEM observation was severely hampered by the very loose, open porous nature of these materials. Despite impregnation with epoxy-resin, these samples contained much loose or friable surface material which could not be adequately coated with carbon for SEM/BSEM observation. As a result, imaging of the samples was hampered by electrical charging of the surface. This also caused charged fragments to 'fly' off the surface during observation. SEM imaging was further hampered by the instability of the epoxy-resin under the electron beam. The resin vaporised, causing further instability of the sample surface, and movement of grains in the surface during observation. This thermal instability could also be a major problem during LAM-ICP-MS. Physical movement of the sample surface during laser ablation, coupled with the problems of precisely identifying the nature of the material being ablated, made any sensible interpretation of LAM-ICP-MS data from these materials impossible.

#### **4.2.3 Electron microprobe characterisation**

Electron microprobe analysis (EMPA) characterisation was carried out for two purposes:

- Microchemical X-ray mapping of selected samples to investigate mineralogical complexity and distribution of major chemical components to give an indication of the representativeness of other investigations.
- Quantitative point analyses of the minerals present to be used in the calibration of the LAM-ICP-MS analyses.

Electron microprobe studies are normally carried out on flat polished specimens and all established techniques and correction procedures are based on this assumption. The samples used in this study were fracture surfaces that are neither flat nor polished which introduced various errors and difficulties.

All the work described in this section was carried out using a Cameca SX50 computer controlled electron microprobe fitted with three wavelength-dispersive (WD) spectrometers.

##### **4.2.3.1 Microchemical X-ray mapping**

Microchemical X-ray mapping was carried out by making qualitative analyses on a matrix of  $512 \times 512$  points with the distance between points selected according to the area of sample to be studied. Three elements (one per spectrometer) can be collected simultaneously, with several passes made if more elements are studied.

The data are displayed as single element colour images where the number of counts in a pixel is represented according to a rainbow colour scale, the lowest intensities are magenta and the highest are red. The data in each image are normalised to utilise the colour range and hence the colour scale is a relative scale for each image and the absolute intensity varies from one to another.

The WD spectrometers used have a small depth of focus, much less than the topography on some of the samples which means that the counts from areas out of focus are much lower than normal. This caused a contour-like banded effect on the images due to the high surface relief of most of the samples.

#### 4.2.3.2 Results of microchemical X-ray mapping

Two samples were selected for X-ray mapping: the granodiorite Eu4G6 and the mylonite Eu2M15. Results for one area of Eu4G6 are described in some detail as an example but other samples and analyses confirm these results (see Appendix B). For all samples, maps were made for 8 elements, Na, K, Mn, Mg, Ca, Fe, Si and Ti along with a backscattered electron image. In addition the mylonite samples were also mapped for Al and P. All the natural and synthetic fault gouge samples had major charging problems and therefore X-ray mapping of samples of these types was not continued after an initial, unsuccessful attempt.

##### Granodiorite sample Eu4G6

Two high magnification X-ray maps covering an area of approximately 1 mm square were made. From optical microscopic examination of the surface, the first area map 'a' appears to be a single large crystal of feldspar but BSEM imaging (Fig. 4.2a) and X-ray mapping indicated that it is not monomineralic and that it has a very complex nature. The map for Si showed that several silicate minerals are present. The highest Si values (reds and yellows, Fig. 4.2b) also correspond to high Na (Fig. 4.2c) or K concentrations (Fig. 4.2d), and are due to albite or orthoclase. The intermediate Si concentration levels (green/yellow colour) correspond to high K, Fe and Mg, and are due to biotite. The areas in the bottom right and centre left of each map of area 'a' (typically showing blue colours) are lower in intensity due to a topographic effect in the sample surface. There are one or two small grains containing only Si (shown as bright red in Fig. 4.2b), which are probably quartz.

The map for Ca showed an abundant mineral with high Ca (yellow/red colours). This mineral also shows moderate levels of Fe but low K and Mg, and corresponds to epidote. The grain size, similar to that of albite, is mostly around 10 – 50  $\mu\text{m}$ .

The maps for Mg and Fe show considerable small-scale variation indicating that there is a fine intergrowth of biotite (high Fe and Mg) and muscovite (lower Fe and Mg). The map for Ti locates numerous small Ti-bearing grains with low Ti contents – these correspond with high-Mg and high-Fe and represent biotite.

BSE and X-ray mapping for the second area, which appeared from optical examination to be largely quartz, also indicated considerable mineralogical complexity. Maps for the different elements allowed identification of component minerals, including fine intergrowths as described in area 'a'.

Maps of both areas demonstrated that the grain size is much finer than appears on optical or visual examination and the actual mineralogy of mineral grains exposed in the fractured surfaces of the granodiorite is very complex. The grain size of quartz is around 100  $\mu\text{m}$ . There are areas of mica with a grain size of around 50 – 100  $\mu\text{m}$ . The coarse K-feldspar crystals with grain size around 500  $\mu\text{m}$  have a complex internal variation and peripheral alteration to epidote and muscovite. The grain size of these secondary minerals and inclusions is around 20  $\mu\text{m}$ . These characteristics will make the interpretation and assignment of surface tracer element analytical data, to a specific mineral phase, very difficult.

##### Mylonite sample Eu2M15

The mylonite sample has a marked schistosity and compositional banding consisting of layers rich in quartz and feldspar alternating with layers rich in micas. Quartz and feldspars were clearly detectable from Si and Al maps. The map for K showed the distribution of K-feldspar

forming many fine grains intergrown with the quartz and albite. The albite distribution showed up very clearly on the Na map which also illustrated the strongly shear-banded fabric of the mylonite sample very clearly. The maps for Fe and Mg showed clearly the distribution of the micas. The dominant mica is biotite (Fe- and Mg-rich) with lesser amounts of muscovite. The maps for Ca, P and Ti identified apatite and sphene grains.

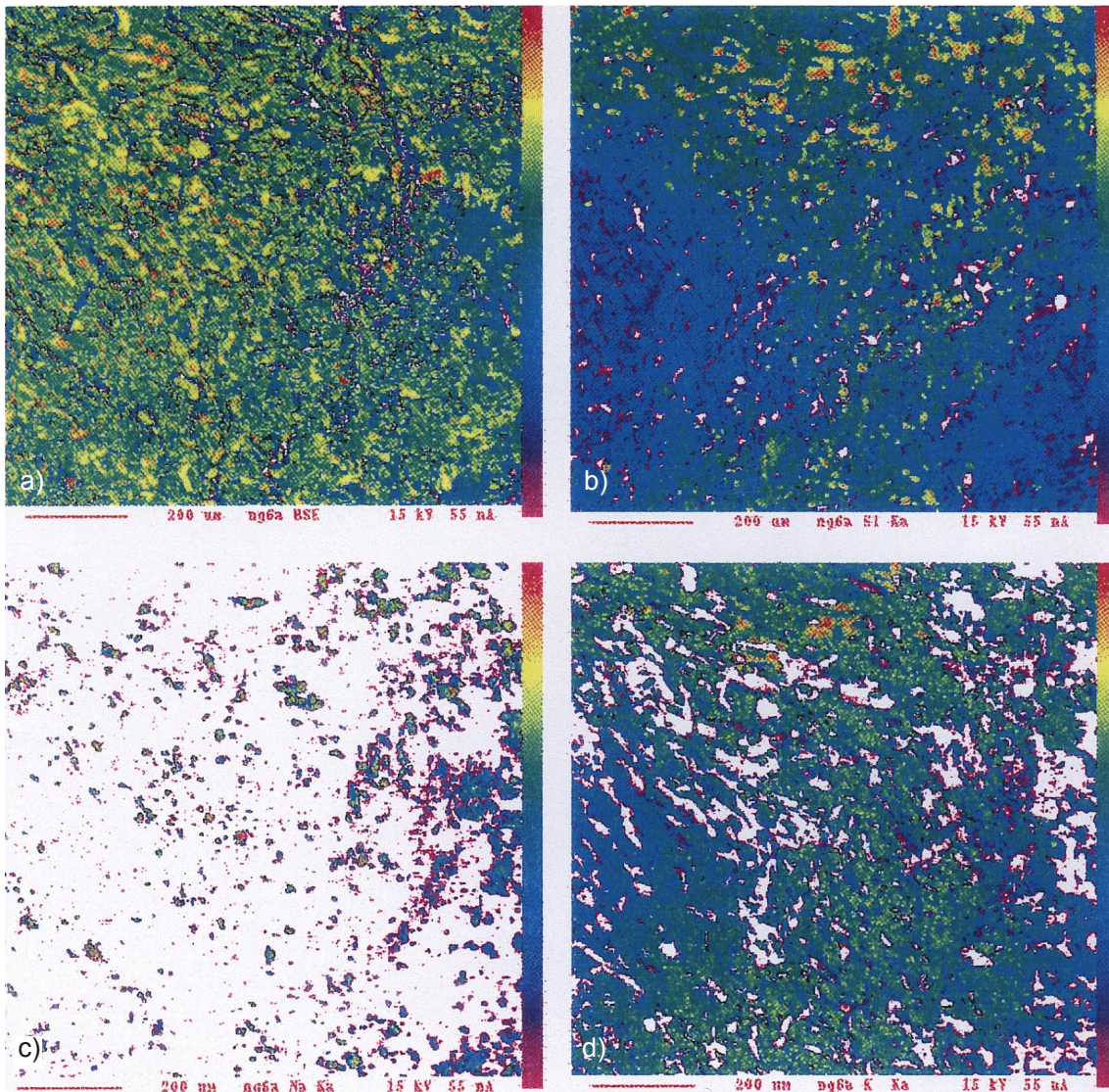


Fig. 4.2: X-ray maps for granodiorite sample Eu4G6, area 'a' – (a) BSEM, (b) Si, (c) Na, (d) K

#### 4.2.3.3 Results of quantitative electron probe point analysis

Quantitative electron microprobe (EMPA) point analyses were made on the mineral phases present in the samples Eu4G6 and Eu2M15 – which represent typical mineral surfaces seen on the granodiorite and mylonite blocks. Since other granodiorite and mylonite test samples were derived from the same original parent material mineral, mineral-chemical data from these two test samples should be valid for the purpose of calibrating the LAM-ICP-MS analyses of all the other samples of these materials.

A number of potential problems have to be considered with regard to EMPA carried out on the samples. These results are adversely affected by the samples being rough rather than flat and polished. This causes the analysis totals to vary from that expected, but careful selection of analysis points enabled reasonably good EMPA results to be obtained in many instances.

A major problem of charging and thermal instability of the sample surfaces under the electron beam (which also combined to produce significant beam-wandering during analysis) was encountered with the natural and synthetic fault gouge test materials. Consequently, no meaningful EMPA point analyses could be obtained from these materials.

### **Granodiorite sample Eu4G6**

The biotite shows little variation in composition and analyses are relatively rich in Fe as is expected for a granodiorite-hosted biotite. The muscovites also show little compositional variation but do have significantly high contents of Fe and Mg.

The feldspars (albite and orthoclase) are close to end-member compositions. In contrast, the one calcic plagioclase analysed has quite high contents of both Na and K.

The epidote group mineral contains around 14 % FeO, which is close to end-member epidote: a typical low-temperature hydrothermal alteration product.

No other elements other than Si were detected in quartz by EMPA and consequently, the quartz is considered to be essentially pure SiO<sub>2</sub>.

### **Mylonite sample Eu2M15**

The biotites in this sample show little variation in composition but are much richer in Mg than those from the granodiorite. This trend is also shown by the muscovites. The only feldspar analysed in this sample was albite, and like the granodiorite, is close to end-member albite.

#### **4.2.4 LAM-ICP-MS analysis**

The principal behind this technique is that the trace elements in the material to be examined are determined by placing the sample in an ablation cell and removing a small sub-sample with the laser ablation microprobe (LAM). The ablated material is transferred to the inductively coupled plasma-mass spectrometer (ICP-MS) in a stream of argon. Further details of the technique, instrumentation, analysis procedure and data handling techniques are given in Appendix B and references therein.

The only requirements on the sample are that the test material will fit inside an ablation chamber (about 10 cm diameter and 2 cm deep) and has a flat enough surface on which to focus the optical microscope and laser. However, the preferred sample types are a thin section at least 30 µm thick, a polished block or single grains mounted on a slide with double-sided sticky tape. The samples examined during this study were not ideal for the best results.

#### **Data quality**

For samples Eu4G6 and Eu8N20, only Eu from the stable isotopes of interest was determined. Sm was also determined to give some indication as to possible Eu levels that would be expected from chondritic abundances. Assuming no Eu anomaly existed, the expected Eu value should be

0.38 times that of Sm. The measured Eu levels in Eu4G6 and Eu8N20 were typically 10 – 100 times that of Sm indicating a very significant uptake on all measured phases.

After analysis of these two samples it was decided to determine all the stable isotopes of interest in the remaining samples, whether they had been doped or not. This gives background levels for the elements that had not been doped in a given sample. For example, Eu levels in sample Sn8N21 and Se8N16, where Sn and Se were doped, do not exceed 10 ppm and a majority are less than 1 ppm. Measured levels in Eu8N20 where Eu was doped are 10s to 1000s ppm.

Only one Se doped sample, Se8N16, was analysed and as expected no Se was observed. Se has a high first ionisation potential and suffers from high polyatomic backgrounds resulting in very poor detection limits.

Sn and Mo occurred in observable amounts in all samples studied and distinguishing doped Sn from natural Sn and Mo is difficult. The high background levels of Sn and Mo may not be real and could possibly be polyatomic interferences. In a full-scale study, careful observation of the isotopic ratios could be used to check for this potential problem. These elements demonstrate both an advantage and a disadvantage of ICP-MS, as both have several isotopes, and if one isotope is prone to an interference another may be chosen. However, multiple isotopes also mean lower isotopic abundance and poorer detection limits. Additionally, where the multiple isotopes occur, they could have been utilised for the interaction of fluids spiked with artificial isotopic ratios. It would then have been possible to measure Sn and Mo isotope ratios and determine if Mo and Sn were of natural or artificial origin.

As part of the quality control (QC) scheme, a reference material was analysed at the beginning and end of every analytical session. Eu and Mo showed reproducibilities and accuracies better than 20 %. Sn was somewhat worse and Se was not considered to be of reportable quality. In over 36 samples from 6 separate analytical sessions, the reproducibility for Mg at the 500 ppm level is 12 %. U at the same level is, however, somewhat worse at 58 %. This is because U is at the extreme mass range of the system and is therefore not so stable from beginning to end of the day.

#### **4.2.4.1 Results of LAM-ICP-MS study**

A descriptive summary of the results is given below and Appendix B should be consulted for the full data tabulation. Although EMPA data were obtained for the minerals being examined by LAM-ICP-MS, there was a major difficulty in precisely identifying individual mineral phases during analysis. Therefore, a 'default' concentration of 100,000 ppm Al (i.e. 18.9 %  $\text{Al}_2\text{O}_3$ ) was used against which the LAM-ICP-MS data were normalised. EMPA data have demonstrated that typically  $\text{Al}_2\text{O}_3$  contents are: biotite 16 %, epidote 23 %, albite 20 %, orthoclase 18 %, plagioclase 18 % and muscovite 30 %. Therefore, except for muscovite, errors in trace element calculation will be small and comparable within an order of magnitude – even with muscovite the error will be less than a factor of 2.

#### **Samples spiked with $^{99}\text{Tc}$ (samples Tc8N15, Tc4G14 and Tc2M5)**

$^{99}\text{Tc}$  was not detected in any of the silicate phases on any of the samples. However, a large amount of  $^{99}\text{Tc}$  was found on the surface of the resin, > 100 times background, in all three samples. Scans for  $^{24}\text{Mg}$  and  $^{44}\text{Ca}$  show that no significant major elements were present in the ablated resin material indicating that this  $^{99}\text{Tc}$  was not due to contamination from included mineral material in the resin.

### **Samples spiked with $^{237}\text{Np}$ (samples Np4G8, Np8N11 and Np2M22)**

$^{237}\text{Np}$  was found on all silicate phases in the natural fault gouge at 10s ppm level. Time resolved analysis (TRA) demonstrated the removal of the  $^{237}\text{Np}$  at the same time as the major elemental components  $^{24}\text{Mg}$  and  $^{27}\text{Al}$ .  $^{237}\text{Np}$  was only found on the K-feldspar in the granodiorite. The TRA (Fig. 4.3) showed a rastered ablation across the surface of the feldspar. From this it can be readily seen that the  $^{237}\text{Np}$  is not distributed in the same way as the  $^{24}\text{Mg}$  and  $^{57}\text{Fe}$  major elements. This suggests that the  $^{237}\text{Np}$  had been inhomogeneously absorbed. No  $^{237}\text{Np}$  was detected on the quartz in the granodiorite. Some  $^{237}\text{Np}$  was detected on the resin from the granodiorite, none on the resin in the natural fault gouge and up to 9 times the maximum found on the granodiorite silicates in the mylonite.

### **Samples spiked with $^{233}\text{U}$ (samples U4G22, U2M13 and U8N12)**

$^{233}\text{U}$  was found on all silicate phases in the natural fault gouge at the 1 to 10s ppm level and on some biotite and K-feldspar in the granodiorite at the 1 to 10s ppm level. The quartz contained no detectable  $^{233}\text{U}$ . In the mylonite,  $^{233}\text{U}$  was found on both the K-feldspar and the biotite at levels up to 1000 ppm. Despite these high levels, the resin was found to have levels 10 times greater than any found in the silicate phases. TRA from the mylonite demonstrated that the  $^{233}\text{U}$  has no association with natural concentrations of  $^{233}\text{U}$  and, by comparison of profiles, that the  $^{233}\text{U}$  response decays with time quicker than  $^{27}\text{Al}$ , suggesting that the  $^{233}\text{U}$  is only present on the surface of the minerals.

### **Samples spiked with $^{242}\text{Pu}$ (samples Pu4G4, Pu2M20 and Pu8N23)**

$^{242}\text{Pu}$  was not found in any of the silicate phases on any of the samples. No  $^{242}\text{Pu}$  was found on the resin in M20 and N23 but only in one of the resin analyses in G4.

### **Samples spiked with Mo, Sn, Eu, Se, $^{99}\text{Tc}$ , $^{233}\text{U}$ and $^{237}\text{Np}$ (sample C6M17)**

- Mo: Occasionally detected at ppm levels on silicate phases. High levels detected on resin.
- Sn: 10 – 100s ppm determined on all silicate phases. High levels, similar to silicates, determined on resin.
- Eu: 10s ppm determined on all silicate phases. Similar levels detected on resin.
- $^{99}\text{Tc}$ : None detected in any silicate phases. High levels, approximately the same as Mo, detected on resin.
- $^{233}\text{U}$ : Occasional ppm levels determined in silicates. Very high levels observed on resin > 1000 times that in silicates.
- $^{237}\text{Np}$ : Only detected once on silicates. Also only once detected on resin at very low level.
- Se: Se was not determined for this sample because studies on other samples revealed that Se could not be detected by LAM-ICP-MS.

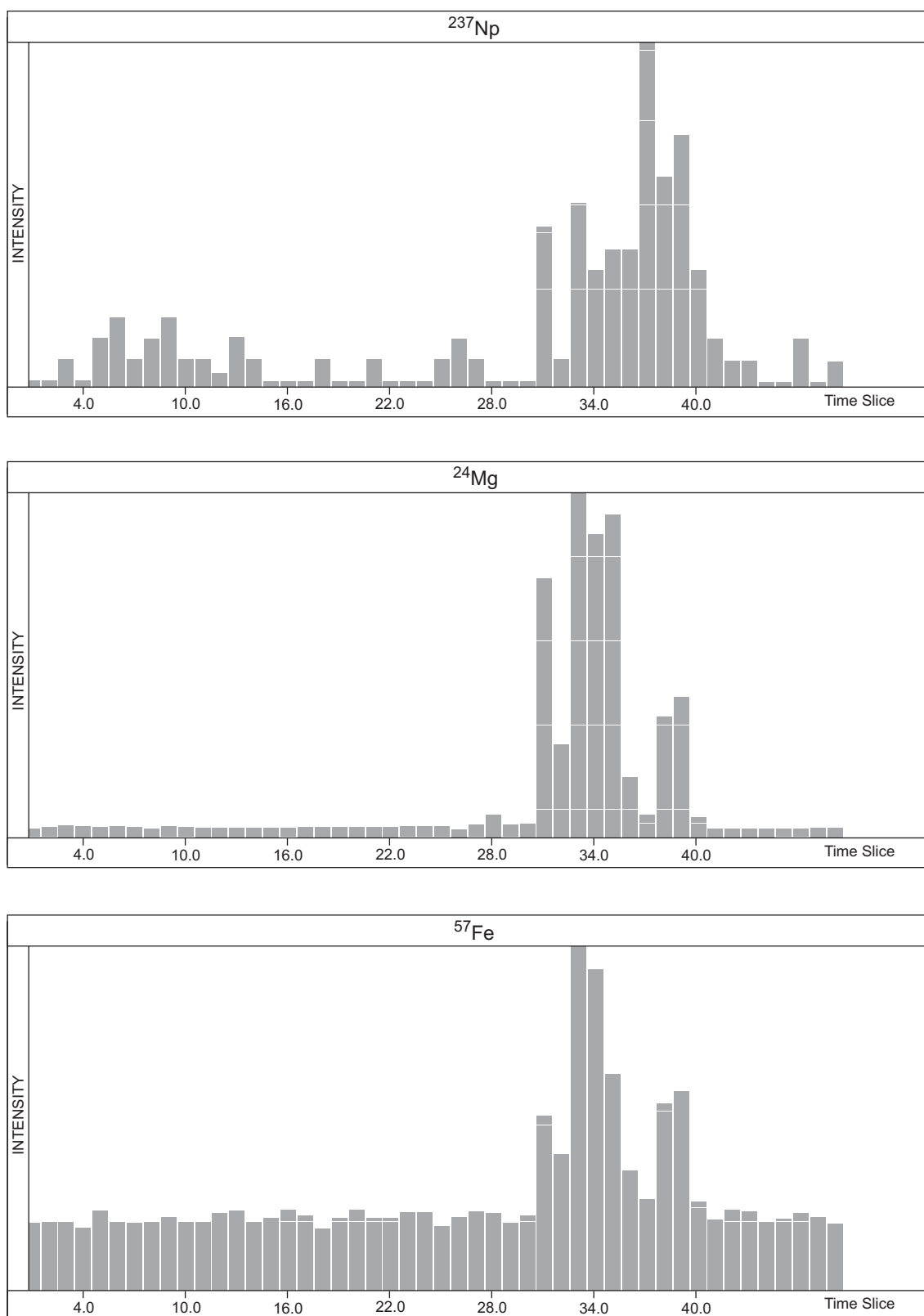


Fig. 4.3: TRA scans for masses  $^{237}\text{Np}$  (top),  $^{24}\text{Mg}$  (middle) and  $^{57}\text{Fe}$  (bottom) during LAM-ICP-MS analysis of K-feldspar in granodiorite sample Np4G8

### **Samples spiked with Mo, Sn, Eu, Se, <sup>99</sup>Tc, <sup>233</sup>U and <sup>237</sup>Np (sample C4M9)**

- Mo: Variable amounts found in both silicate phases and resin. Resin contained 10 – 30 times the maximum amount in the silicate.
- Sn: 100s ppm found on all the silicate phases. Maximum on silicate greater than that found on the resin.
- Eu: 100s ppm found on all the silicate phases. Much greater amount (10 – 100 times greater) found for silicates compared to resin.
- <sup>99</sup>Tc: None found in silicates or on resin
- <sup>233</sup>U: 10s ppm found in silicates but more than 10 times as much found on resin.
- <sup>237</sup>Np: Variable amounts (0 – 10s ppm) detected in the silicate phases, particularly on the muscovite. None detected on the resin.
- Se: Not determined for this sample.

### **Samples spiked with Eu (samples Eu2M15, Eu4G6 and Eu8N20)**

Eu was detected in biotite and muscovite at levels up to 70 ppm and at lower levels in feldspar in the mylonite. Biotite in granodiorite contained Eu up to 2300 ppm, which could be due to the presence of REE mineral inclusions, while Eu in feldspar was measured up to 400 ppm. The fault gouge all contained Eu up to 1100 ppm but most less than 200 ppm. Eu was not found in the resin.

### **Samples spiked with Mo (samples Mo2M11, Mo4G12 and Mo8N9)**

Mo was detected at low levels (up to 70 ppm) in roughly half the analyses of biotite and muscovite in the mylonite M11 and K-feldspar in the granodiorite G12. It was detected at similar levels in all analyses on the natural fault gouge N9. Mo was not detected in the resin.

### **Samples spiked with Sn (samples Sn2M12, Sn4G17 and Sn8N21)**

Sn was detected at levels around 50 ppm in all analyses of biotite and muscovite and most K-feldspars. It was detected at slightly higher levels (up to 360 ppm) in the matrix of the fault gouge N21. Sn was not found in the resin.

## **4.2.5 Discussion and conclusions**

### **SEM and BSEM studies**

The study showed that careful characterisation of the surface is required to interpret any LAM-ICP-MS data. BSEM and SEM have proved particularly useful in identifying surface mineralogy, mineral distributions and surface topography.

SEM studies have shown that many of the minerals do not present simple planar surfaces, and mineral surfaces may contain significant internal microporosity. The surfaces of these pores potentially will have interacted with the tracer solutions during the doping experiments.

Consequently, the uptake of tracer elements within the microporosity will need to be considered in any interpretation of element-depth profiles. The minerals most likely to be affected by significant internal microporosity are biotite and muscovite (porosity present along 001-cleavage which persists for tens of microns into the interior of grains) and feldspars (porosity present as small pits and cavities in the grain surface).

BSEM proved invaluable in providing maps of mineral distribution in the sample surfaces. These were essential for location of mineral grains during subsequent LAM-ICP-MS analysis. BSEM also revealed the complexity of the mineral surfaces: revealing complex intergrowths between muscovite and biotite, and between albite and K-feldspar in surfaces of grains/crystals that superficially appeared to be monomineralic based on observation under the optical microscope.

### **Electron microprobe studies**

Normally, EMPA requires the sample surface to be presented as a flat polished surface. This is required to allow for normal X-ray fluorescence and absorption and X-ray path criteria to be accounted for during analysis. However, despite the rough nature of the surfaces of the samples examined in this study, it has been shown that digital X-ray microchemical mapping can still provide very useful information on the surface mineralogical and textural features of these materials. Furthermore, it is possible to obtain reasonable quantitative EMPA major element point analyses of individual minerals. As a result of EMPA characterisation, the following points can be made which will be relevant in any interpretation of LAM-ICP-MS data (as presented here), or data from other techniques such as SIMS which might be applied to the characterisation of the same materials.

- Quantitative analysis shows that most minerals have simple compositions with little variation within a sample and should be a good internal standard for the laser ablation studies.
- Microchemical mapping shows that the granodiorite has been affected by low temperature alteration and associated recrystallisation, which gives an effective grain size around 50 – 100  $\mu\text{m}$ .
- Microchemical mapping shows that many fine-grained accessory minerals (zircons, apatite, monazite, Ti-Fe oxides) are present which could be important natural hosts of the elements (e.g. Eu, Mo, Sn) in question. They are too small to identify for laser analysis.

### **Laser ablation studies**

LAM-ICP-MS of the materials examined was problematic. One very major problem that was encountered was the difficulty in precisely locating and identifying individual mineral grains during LAM-ICP-MS. The instrument relies on high-magnification optical microscope to locate grains/points for analysis. Because the samples provided have very high surface relief, the limited depth of focus of the optical microscope hampered the precise location and identification of mineral grains. In any case, a detailed characterisation of the mineralogy and surface morphology of the sample surface by BSEM and SEM is an essential pre-requisite for LAM-ICP-MS. This was important both for providing 'maps' of the sample surface to aid location of mineral grains for analysis and for understanding the precise nature of the material being ablated. Many of the difficulties experienced here will also be significant in the interpretation of data obtained from the same materials by surface analytical techniques such as SIMS.

With respect to the present study, the following conclusions can be drawn from the LAM-ICP-MS examination:

- Stable isotopes are present on the majority of mineral grains analysed at levels of a few tens of ppm. There does not appear to be any preferential take-up by any particular mineral species, bearing in mind the problems of mineral recognition during laser analysis.
- The distribution of active isotopes is more complex. U and Np were found on most silicate phases whilst Pu and Tc were not detected on any. All active elements were detected in the resin, particularly 'high' levels of U and Tc and to a lesser extent Np. However, as noted in Section 3.1, there is no appreciable uptake of radionuclides in resin when it is added to the rock subsequent to radionuclide / rock interaction and, as such, this observation is of no relevance to the field experiment (discussed further below).
- The TRA profiles show that the elements are only present in a thin surface layer. This makes quantification difficult as this is based on an internal standard for the whole ablation.
- LAM-ICP-MS is unsuitable for determining Se due to problems of interference, resulting in very poor detection limits for this element.

#### **Problems encountered and recommendations for future work**

The samples had considerable surface topography which creates many problems for electron probe and LAM-ICP-MS. If the sample has a maximum relief of  $\pm 100 \mu\text{m}$ , this would allow more accurate identification of mineral types, mineral boundaries and would ensure that the amount of material sampled by the laser was relatively constant for a given laser energy. This problem will also affect other techniques that might be considered, such as SIMS and ion microprobe which similarly utilise optical microscopes to select analysis points.

Several of the samples were prepared so that an essentially planar fracture surface was mounted with a substantial slope. This means that extensive refocusing is required to bring the sample to the correct height for study. Mounting the samples so that the surface is parallel to the base would have saved considerable time and effort and improved the quality of results.

Many mineral surfaces were heavily contaminated with resin, this leads to uncertainty as to what is being analysed. This was particularly problematic with the natural and synthetic fault gouge samples. Also in some cases the resin absorbs the dope elements and confuses results.

Many of the samples were covered with a fine 'mineral dust', which makes analysis of single mineral phases impossible. This was particularly problematic in the study of the natural and synthetic fault gouge materials. These samples provided further difficulties because much of the material comprises complex aggregated masses of fine-grained minerals which individually, were beyond the spatial resolution of the LAM-ICP-MS technique.

#### **4.3 Feasibility of the use of PET (Positron Emission Tomography) to determine porosity and image fractures in granodiorite**

*R.P. Maguire, J.H. Missimer and K.L. Leenders*

The work described here and in the following section (4.4) attempted to assess techniques which would allow definition of porosity and presence of channels etc. non-destructively, as compared to traditional, destructive techniques such as thin section petrology. There were two reasons for this: first it was initially thought that the material excavated from the migration shear zone

might be too unstable to transport and thus an preliminary examination of the pore structure of the sample would have to be carried out immediately in the GTS. Second, it was felt worthwhile comparing non-destructive techniques with the standard (destructive) technique to assess any artefacts inherent to the latter method.

The goal of the feasibility study was to investigate, with positron emission tomography (PET), the imaging of fractures in a cylindrical core of granodiorite and the determination of their porosity.

The study consisted of scanning a cylindrical core of granodiorite (the phantom) into which five holes of varying diameters were drilled to simulate fractures. Glass tubes, containing a mixture of resin and granodiorite particles with resin-filled porosities of between 20 % and 35 %, were then placed in the holes. Tab. 4.1 gives the dimensions and activities of the eight tubes used. The phantom and tubes were prepared in collaboration with P. Bossart and H. Dollinger of Geotechnisches Institut AG in Berne.

Tab. 4.1: Tube dimensions, porosity, activities

<b>Tube</b>	<b>Inner diameter [mm]</b>	<b>Active length [mm]</b>	<b>Activity [kBq]</b>	<b>Porosity [%]</b>
1	20	120	155	20
2	15	147	120	23
3	8	147	23	20
4	9	144	38	20
5	9	144	62	35
6	8	144	45	35
7	8	147	25	20
8	8	140	23	20

The principle of PET is the coincident detection of the two 511 keV photons emitted in the annihilation of an electron in the object under study and a positron from a radioactive tracer. Since the positron and electron have little momenta, the photons emerge at almost exactly 180°. They are detected by crystals of bismuth germanate (BGO) arranged in a cylindrical array around the object; BGO is efficient at detecting photons but can discriminate their energy only within about 120 keV. The coincidences in each pair of opposing detectors are counted electronically before being processed by a computer to yield an image of tracer activity. The scanner used in this study featured a ring diameter of 84 cm and an axial length of 15.4 cm (TOWNSEND et al. 1993). The resolution of the scanner was measured before the phantom study: transaxial resolution is 5.9 mm at the centre of the field-of-view and 6.2 mm (tangential) and 7.5 mm (radial) at 10 mm from the centre, degrading to 8.1 mm and 9.3 mm respectively at 20 mm from the axis. Mean axial resolution is 6.3 mm.

Before shipment to the study instrument in Pittsburgh, the tubes were scanned with the CTI scanner of PSI for which the calibration factor is known thoroughly (MAGUIRE & MISSIMER 1993). The activity concentrations and porosities determined by the scans were in good agreement with independent measurements made with a well counter and scales during filling of the

tubes. Comparison with equivalent scans made in Pittsburgh yielded a calibration factor for that scanner.

Five scans of the rock phantom were made. Two scans of 3-hour duration and one of 15 hours were made of the tubes in various configurations of porosity and depth of insertion in the phantom. One transmission scan lasting 15 hours was made in which the phantom was imaged by a plane source, containing about 1 mCi of  $^{68}\text{Ge}$ , shaped to follow the curvature of the detector array. Comparison with a 3-hour scan in which the phantom was absent yielded the attenuation factor describing the loss of photons due to absorption as they traverse the granodiorite. Finally, a Ge-rod source placed in the largest of the holes closest to the centre of the phantom was scanned for 21 hours; evaluation provided the fraction of photons scattered but not absorbed on the way to the detector as well as the response function of the rock, describing the distortion and smearing of the image due to scatter.

#### 4.3.1 Results and Discussion

The following describes, first, the analysis and interpretation of the attenuation and scattering measurements, which leads to an estimate of the signal-to-noise ratio (SNR), a quantity reflecting image quality. Second, the sensitivity of the scanner to porosity is estimated. An essential aspect of the analysis is the dependence of image quality and porosity measurement on the diameter of the rock core to be extracted from the experimental shear zone.

Analysis of measurements: The definition of the linear attenuation coefficient yields the relationship between the intensity of photons in the absence of attenuating material and the intensity of non-interacting photons after passage through the attenuating material, granodiorite in this case.

The analysis yielded the attenuation coefficient,  $\mu = 0.26 \text{ cm}^{-1}$ , which is about 10 % larger than the attenuation coefficient of concrete used in the estimate of activity and radiation dose (see Appendix C) and corresponded to the mass attenuation coefficient of water,  $0.1 \text{ g cm}^{-2}$ . This was a reasonable result since the mass attenuation coefficient, which can be expressed as the ratio of density to the linear attenuation coefficient, was almost independent of material. However, the absorption coefficient,  $\mu_a$ , was twice as large as the value predicted for the pencil beam set-up, indicating the importance of geometry in determining the coefficient.

Signal-to-noise ratio: calculation of the signal-to-noise ratio, the ratio of true photons (passed unperturbed from the emitting tracer) to scattered and random photons in pixels exhibiting activity, required the subtraction of scattered photons from the sum of true and scattered photons. An estimate of the true photons remaining after this correction is incorporated in the quantity designated Noise Equivalent Counts NEC (STROTHER et al. 1990).

In contrast to NEC, which characterises the total number of true photons, SNR is a local property. It is proportional to the square root of NEC:

$$\text{SNR} \approx (s / D)^{3/2} \text{ NEC}^{1/2}$$

where  $s$  is the pixel size and  $D$  the diameter of a tube filled with activity in the centre of the granodiorite cylinder. The threshold for perception of an image is conservatively estimated to lie between 3 and 5 (BARRETT & SWINDELL 1981), i.e. the signal must be three to five times more intense than the noise for it to be recognised.

In order to illustrate the concepts of NEC and SNR, assume an activity concentration of  $4 \text{ Bq mL}^{-1}$  in a tube of cross section  $1 \text{ cm}^2$  and length  $15 \text{ cm}$  placed at the centre of a granodiorite core of diameter  $21.5 \text{ cm}$ . This corresponds to that of resin with an activity concentration of  $20 \text{ kBq mL}^{-1}$  dispersed in granodiorite of  $20 \%$  porosity as in the actual phantom studies. The combined geometrical and electronic efficiency of the RPT-2 was determined to be about  $1 \%$ . Thus, the count rate in the absence of attenuation  $I_0$  is  $70 \text{ cps}$ , yielding a total rate for trues and scattered of  $2.2 \text{ cps}$ . Taking the ratio of true to total photons of  $0.13$  from the Ge-rod scan gives:

$$\text{NEC} \approx 0.037 \text{ and (with pixel size of } 0.42 \text{ cm) } \text{SNR} \approx 0.37 t^{1/2}$$

where  $t$  is scan time. Thus a minimum SNR requires a scan time of  $6600 \text{ s}$  or  $1.8 \text{ hours}$ . However, crude estimates of signal to noise ratio in the  $15 \text{ hour}$  phantom scan indicated an SNR between  $2$  and  $3$  suggesting that the simple calculation underestimates the required time. The estimate assumed a granodiorite cylinder of  $21.5 \text{ cm}$ . Tab. 4.2 shows the scan time as a function of diameter.

Tab. 4.2: NEC rate and measuring time in hours as function of granodiorite core diameter in pencil beam model

Diameter [cm]	NEC [cps]	Time (SNR > 3) [hrs]	Time (SNR > 10) [hrs]
10	2.07	0.033	0.37
21.5	0.037	1.9	2
25	0.011	6.4	7
30	0.002	37	407
35	0.0003	210	2344
40	0.0001	1214	13491

Sensitivity to porosity: the noise equivalent counts and signal-to-noise ratio figure prominently in the determination of porosity. In terms of activity concentrations, porosity is the ratio of the concentration in the rock  $a_{ro}$  to that in the resin  $a_{re}$ :

$$p = a_{ro} / a_{re}$$

The activity concentration in resin can be measured at injection; the concentration in the rock was measured by the scanner.

The accuracy of the determination of activity concentration in the resin is likely to be the limiting term in determining porosity. Obtaining a homogenous distribution of activity in the resin and measuring the distribution were both demanding tasks in the feasibility study; obtaining an accuracy of better than  $1 \%$  would be a major technical challenge. If this and other sources of inaccuracy (arising from NEC determination etc.) can be held to the  $1 \%$  level, measuring porosities of  $10 \%$  with an accuracy of  $10 \%$ , i.e.  $\delta p / p < 0.1$ , can be achieved for  $\text{SNR} > 10$ , implying a scan time of  $21 \text{ hrs}$  for the core of  $21.5 \text{ cm}$ , if the estimate above for the minimum SNR is correct. Tab. 4.2 shows measuring times needed to obtain the required accuracy as a function of core radius in the pencil beam model used above. These estimates of the errors imply a lower limit on the accuracy with which porosity can be determined of about  $3 \%$ , requiring a scan time of almost  $19 \text{ hrs}$  for a core  $10 \text{ cm}$  in diameter.

An additional consideration in the measurement of porosity is the resolution of the scanner and the consequent partial volume effect. Scans in the phantom indicated that the resolution of the scanner was degraded by the granodiorite from about 7 mm to about 10 mm. This should be improved by the scatter subtraction. However, the resolution increased the apparent size of the activity distribution and decreased the apparent activity concentration. Thus, for regions of less than about 2 cm in any dimension, the partial volume effect implied a significant overestimate of the special extent and an underestimate of the porosity. Whether corrected by deconvolution or by hand, the partial volume effect represents an additional source of inaccuracy in measurements of porosity in small regions of activity.

#### **4.3.2 Conclusions**

PET was demonstrated to be a promising method for imaging activity distributions in granodiorite. Tab. 4.2 demonstrates that determination of the porosity with an acceptable accuracy is possible, if time consuming, as long as the diameter of the core does not exceed 22 cm. Since increasing the activity in the resin reduces the scanning time by the square root of the factor of increase, even the maximum activity permitted by radiation safety can reduce the scan times by only a factor of 5. The optimal activity in the resin is still to be determined.

Measurement of the porosity will require accurate determination of the activity concentration in resin, measurement and control of the scanner efficiency over the field-of-view occupied by the core and a quantitative understanding of the attenuation and scattering in the granodiorite core. In addition, subtraction of the scattered photons from the image must be implemented; a procedure for performing the subtraction has been developed for medical imaging studies (BAILEY & MEIKLE 1994), but its application to the core from the experimental shear zone needs to be explored.

#### **4.4 Feasibility of the use of micro-resistivity core imaging to determine connected porosity in granodiorite**

*P.D. Jackson, R.C. Flint and J.K. Ball*

A feasibility study was undertaken to assess the suitability of the micro-resistivity imaging technique as a means of assessing open porosity, impregnated with non-conducting resin, in fully saturated mylonite within a fractured granodiorite host.

A series of numerical and practical experiments were used to determine whether micro-resistivity measurements can detect and characterise the presence of 'resin' and mylonite when there is granodiorite between them and the electrode array. While mylonite samples were provided fully-saturated, granodiorite slabs were obtained dry and were subsequently saturated at the British Geological Survey (BGS) using de-ionised water. Air gaps were used to simulate the presence of resin in these practical experiments. The study describes practical measurements on simple 'synthetic' structures, and shows numerical simulations of them.

#### **Resistivity of granodiorite**

The resistivity of granodiorite is expected to be extremely high and almost at the limits of detectability of current technology.

The following factors control the electrical resistivity of granites and other similar crystalline rocks (BRACE et al. 1965, PARKHOMENKO 1967, EVANS 1980):

- 1) Pore fluid resistivity
- 2) Surface conduction
- 3) Connected or effective porosity
- 4) Tortuosity of the pore channels
- 5) Temperature
- 6) Frequency of alternating current flow.

Laboratory measurements of electrical resistance of cores from intact crystalline rock samples will be degraded by the alteration caused by the sampling process and it will be difficult to predict *in situ* values from laboratory measurements. In this particular case, impregnation with resin while maintaining the sample-structure, replaces pore fluid with a non-conductor and hence changes the electrical resistivity of the sample. However if the distribution of the insulating, impregnating resin can be identified using resistivity measurements, then the open connected porosity can be identified by this method.

PARKHOMENKO (1967) gives a vast collection of data for moisture-containing crystalline rocks including granites, diabases, andesites, and crystalline limestones. The porosities considered are in the range 0.01 to 3 % (i.e. 0.0001 to 0.03 fractional porosity). Resistivities are given as  $10^7 - 10^8$  ohm-m for dry granites in the temperature range 20 – 600 °C and 0 to 1.5 kbar pressure. For water saturated rocks, Parkhomenko gives values of  $10^3 - 10^7$  ohm-m depending on fluid resistivity and porosity.

Taking the work of BRACE et al. (1965), a simplified equation relating the rock resistivity to effective porosity  $n$  is:

$$\rho_{\text{rock}} = \rho_{\text{water}} / (10 n^2)$$

Here  $n$  is connected porosity and the factor 10 represents the surface conduction effect in an approximate way.

Using this formulation, it can be seen that:

$$\rho_{\text{rock}} = 2 \times 10^4 \text{ to } 2 \times 10^6 \text{ ohm-m for porosity} = 0.01 \text{ to } 0.0001$$

given a pore fluid resistivity of 20 ohm-m. Thus for unfractured granite of 0.1 % porosity, a resistivity in the region of  $10^6$  ohm-m may be expected in laboratory samples. These samples will have been de-stressed and disturbed, so there will always be uncertainties in these laboratory measurements due to the difficulty of returning the sample to its *in situ* state.

#### 4.4.1 Micro-resistivity core imaging

Measurements are made on slabbed core samples having flat upper surfaces  $70 \times 270$  mm onto which a multi-electrode pad is placed. The pad can be sealed to the flat surface of the core and pore fluids passed through. The electrode pad consists of 576 electrodes ( $12 \times 48$  grid at an

electrode separation of 5 mm, each electrode having a diameter of 0.5 mm) that can be configured to pass current or to measure potential differences, under automatic computer control. The current passed is DC switched at a frequency of 100 Hz and measurements made during the latter half of each half cycle in order to eliminate electrolysis and AC coupled transient signals.

The samples were two granodiorite slabs ( $15 \times 70 \times 240$  mm) and a smaller 'triangular' shaped sample of mylonite (9 mm thick). The slabs were received already cut to a size that would suit the core imaging system.

A series of numerical experiments were made, as shown in Fig. 4.4, with the aim of evaluating the performance of the core imaging technique to the particular geometries imposed by the samples. A 3-D finite difference resistivity modelling technique (JACKSON et al. 1990), similar to DEY & MORRISON (1982) was used. In addition, a technique which solves for 'one dimension at a time' using a modified tri-diagonal matrix algorithm was employed.

Six cases in all were simulated covering the permutations of a granodiorite / mylonite / resin / granodiorite 'stack' as shown in Fig. 4.4. As described earlier, the resistivity of the granodiorite was expected to be in the region of  $10^5$  ohm-m and was modelled accordingly.

Case 1 is a low resistivity 'bar' of mylonite ( $1 \times 10^6$  ohm-m) in between two granodiorite slabs of a higher resistivity ( $2.5 \times 10^6$  ohm-m), the 'rest' being 'resin' which has an infinite resistivity (the 'resin' is simulated by air in the experiments).

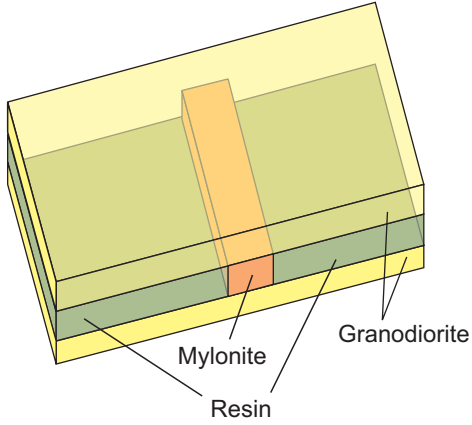
The technique used allowed the production of an image downwards into a slab at gradually increasing depths of investigation. The depth of investigation increases with the separation of the current electrodes with 50 % of the current flowing beneath a depth of  $AB/3$  for a homogeneous medium (e.g. the shallowest depth of investigation has  $AB/3 = 5.08$  mm when  $AB = 3$  units and 1 unit = 5.08 mm).

The numerical simulations show the response of different AB spacings to a bar of lower resistivity. The results for  $AB = 3$  units (15 mm) show a response almost entirely due to the top-most 'granodiorite' slab, while the  $AB = 9$  units (45 mm) has its values of apparent resistivity almost doubled at positions above the infinitely resistive 'resin'. Further increase in AB caused even higher values either side of the conductive bar, indicating the presence of a relative non-conductor (i.e. 'resin').

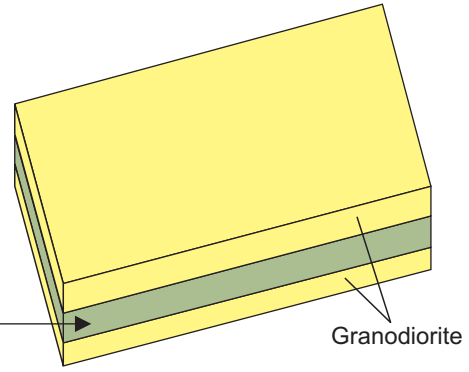
The position and shape of the 'mylonite' bar and surrounding 'resin' have been determined by the measurements with  $AB > 3$  units (15 mm), but overestimate its resistivity. Measurement sets were designed that depict structure realistically without further processing but require 3-D inversion, as described above, to correct the resistivity values.

It was concluded that the micro-resistivity imaging technique is capable of detecting the location of mylonite and 'resin' in the 9 mm thick space between two 15 mm thick slabs of granodiorite when the ratio of resistivities between the two rocks is at least 2.5. Furthermore the series of 2-D images would provide a suitable detection system for connected open porosity in which resin has displaced pore-water. The current gathering correction to the 'whole core image' provided 'realistic' 2-D images when the mylonite does not extend across the whole of the space between the granodiorite slabs, giving added information regarding the connectivity of the porosity (i.e. 'resin').

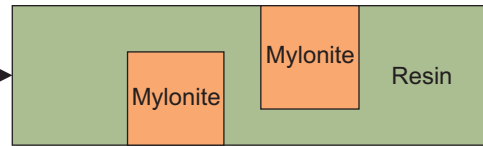
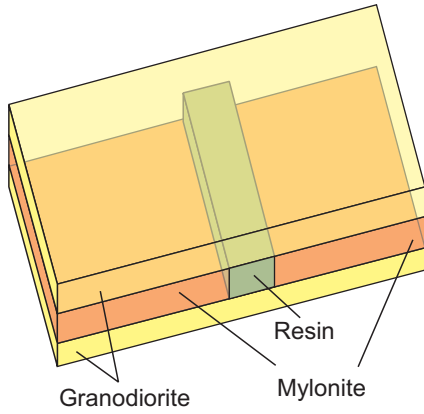
Case 1:  
Bar of lower than background resistivity completely across centre of the 'sandwich' structure



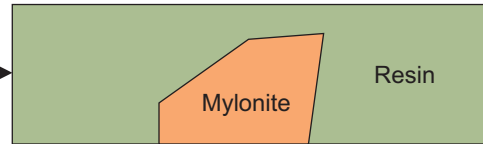
Case 4:  
Two bars of lower than background resistivity arranged within the 'sandwich' structure



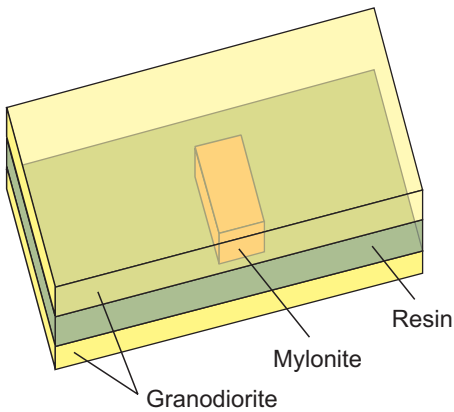
Case 2:  
Resin of infinite resistivity completely across centre of the 'sandwich' structure



Case 5:  
Simulation of laboratory measurements 'triangular' shaped object



Case 3:  
Bar of lower than background resistivity at the centre of the 'sandwich' structure



Case 6:  
Simulation of laboratory measurements 'rectangular' shaped object

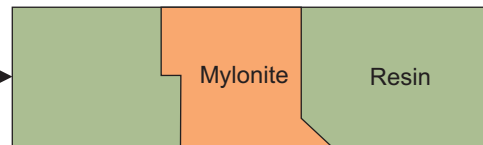


Fig. 4.4: Diagrams of experimental set-up used in the numerical simulations

#### 4.4.1.1 Practical micro-resistivity core imaging

The experiment utilised an array of 576 electrodes arranged in a  $12 \times 48$  grid on 5.08 mm centres. The experiment attempted to detect mylonite targets sandwiched between granodiorite slabs by 'imaging through' the top slab with various measurement electrode configurations to probe to various depths. This technique has been successfully used on sandstone reservoir rocks to build up a three dimensional resistivity and porosity image (JACKSON et al. 1994) and is an ideal starting point for 3-D inversion of the data as recommended below.

To make a measurement, four electrodes are selected electronically under computer control to act as current and potential electrodes (C1, C2, P1 and P2). Current, in the form of a switched DC waveform is passed between C1 and C2 whilst the amplitude of the waveform is measured between P1 and P2. This amplitude is proportional to the electrical resistance between P1 and P2 and is converted into a resistivity value by simple mathematical techniques.

The granodiorite slabs were dry on arrival and so had to be re-saturated. This was done by placing them in a pressure cell with de-ionised water at a pressure of 10 bar. This pressure was maintained for a period of 10 days. The imaging experiment consisted of scanning the entire sample with different measurement array configurations. These scans start with the four electrodes in line (C1, P1, P2 and C2) known as AB = 3 due to the 3 electrode separation between the current electrodes. This is then repeated four further times with AB values of 6, 9, 12 and 15 as described above.

The first images were taken within 2 hours of the samples being removed from the saturating chamber and used the AB = 12 configuration as it was thought that this would best show the mylonite target. The results indicate that the resistivity of the sample had generally increased by 10 % over this two-hour period, while changes to the 'structure' of the resistivity image were hardly discernible.

Two full measurement sets were then undertaken using all five electrode configurations. They were performed both on the 'sandwich' of granodiorite-mylonite-granodiorite and on a single granodiorite slab positioned on an insulating rubber sheet. Although individual measurements were repeatable the results were very different to those made previously.

By this stage a serious problem became apparent. The granodiorite slabs proved very fragile and cracked spontaneously. A thin diagonal band of higher resistivity was consistent with a crack opening in the 24-hour period between the two sets of measurements.

The results were in agreement with the numerical modelling and indicated electric current passed through the granodiorite slab and into the mylonite beneath. It was not possible to be more quantitative as the resistivity of the granodiorite slabs changed continually as they appeared to disaggregate.

#### 4.4.2 Conclusions

Micro resistivity imaging has been possible on granodiorite slab samples. A series of 2-D measurements were made on a single granodiorite slab that agree with 3-D numerical simulations, indicating that a series of 2-D slices correspond with the 3-D model in terms of structural information and are an ideal starting point for 3-D processing designed to invert the values of apparent resistivity into true resistivity.

Numerical simulations showed that the technique has the potential to characterise mylonite when placed beneath granodiorite. In practice, the granodiorite was found to be unstable resulting in an unexpected change in resistivity with time that masked investigations of the mylonite. The use of resin-saturated granodiorite slabs from the experimental shear zone should reduce the time-varying nature of the resistivity observed and would be more representative of 'post feasibility' conditions.

The results showed that the micro-resistivity technique has the potential to image mylonite beneath granodiorite and is able to distinguish between granodiorite, mylonite, and resin (infinitely resistive 'air' in the experiments). Thus the technique could be developed to characterise the connected flowpaths where resin had displaced the pore water within the shear zone (assuming that resin-impregnated granodiorite is not an insulator).

Additional work to test whether an electrical current can be passed through a resin-impregnated granodiorite slab was recommended. If this were successful, the experiments described in the report should be repeated using resin-impregnated slabs of granodiorite. Without this additional information, it is not possible to assess the performance of micro-resistivity imaging on resin-impregnated samples from a GTS shear zone.

3-D inversion of the resistivity data would be required to provide more accurate estimates of resistivities, although the tomographic data sets provide realistic structural information. 3-D estimates of resistivity would enable the disposition of each of the components of the system (resin-impregnated granodiorite / mylonite / resin) to be identified which, in turn, would define fluid pathways in the *in situ* state, as the distribution of the resin corresponds to the open porosity that has been impregnated. Pore-fluid within microcracks and unconnected or 'dead-end' pores would modify the rock resistivity.

## 5 Conclusions

*F.B. Neall and W.R. Alexander*

The experimental studies in support of the Excavation Project have demonstrated that:

- A suitable resin composition can be used to immobilise the experimental shear zone, providing sufficient mechanical strength to allow subsequent overcoring and sub-sampling. A low viscosity epoxy resin provides adequate penetration at low injection pressures, which ensures minimal disruption of the fine structure of the friable fault gouge material, while still giving reasonable injection rates. Hardening is also sufficient to allow preparation of normal petrographic thin sections and other samples for subsequent analysis.
- The potential effects of water displacement by the resin on the existing radionuclide distribution or water/resin immiscibility preventing penetration of the fine-grained material is avoidable by injection of a range of alcohols into the shear zone prior to resin injection.
- The use of the immobilisation and overcoring techniques *in situ* is certainly feasible.
- Injection of resin into the shear zone will have no effect on the sorption of radionuclides as it did not significantly compete with the mineral surfaces<sup>12</sup>. Likewise, the alcohol has little tendency to desorb most radionuclides used (Se, U, Np, Sn and Mo), although a small effect was detected for Tc, Pu and Eu.
- Sorption of radionuclides on equipment is a factor which will have to be taken into account as significant sorption of radionuclides on several materials was found with Pu and Sn being worst affected, particularly by silicone rubber and stainless steel surfaces.
- A small kinetic effect in the sorption of several radionuclides (Co, Eu and U) is also a factor which will have to be taken into account in designing the EP experiment. Se was found not to show significant sorption and experimental problems were encountered with Np and Tc so that the effect of kinetics on these radionuclides is still uncertain.
- Scanning electron microscopy (SEM) and back-scattered electron microscopy (BSEM) are useful techniques for surface characterisation with regard to mineralogy and topography, and for preparation of maps of mineral distribution for location of LAM-ICP-MS and SIMS analysis areas. SEM also showed that the surfaces of some minerals, particularly biotite, muscovite and feldspars, are not simple planes but contain significant microporosity which may affect the apparent distribution of radionuclides associated with a mineral grain.
- Electron microprobe analysis (EMPA) was useful as a technique for mapping element distribution (microchemical X-ray mapping) and was potentially a quantitative tool, despite some analytical difficulties with surface topography on the unpolished samples. This spatially resolved analysis also indicated that fine-grained accessory minerals (e.g. zircon, apatite, monazite, Fe-Ti oxides), which are natural hosts to radioactive elements, might give problems in LAM-ICP-MS as they would be below its spatial resolution.
- In unpolished samples, the laser ablation microprobe – inductively coupled plasma – mass spectrometry (LAM-ICP-MS) technique encountered problems with precise location of mineral grains identified for analysis by EMPA/BSEM, due to the significant surface topography. Analyses were also hindered by resin on the surfaces of minerals and a surface layer of very fine dust particles, which confused the analysis of single mineral grains. The fault

---

<sup>12</sup> Note, however, that in Section 4.2.4.1 it was reported that polymerised resin had taken up radionuclides from solution, indicating different resin behaviour following hardening. As this scenario is not foreseen for the *in situ* experiment, these results are of no relevance to the final experiment.

gouge samples presented problems due to their fine-grained nature – individual clasts and minerals were generally below the limit of resolution of the technique. In general, however, the results suggest that this technique can make a significant contribution to the aims of the EP, so long as care is taken with sample preparation and preliminary analysis by SEM/BSEM and EMPA.

- Secondary ion mass spectrometry (SIMS) had similar problems with surface topography of samples, in this case preventing surface charge neutralisation. However, the technique proved useful for broad area analyses on solid rock samples. Fine-grained powder samples were less successful.

A number of recommendations for sample preparation, based on the experience of these studies, were made:

- Samples should have as near flat surfaces as possible, although it is acknowledged that cleaved planes of rock samples will need to be analysed. Care should be taken that samples for SIMS are not too thick.
- Handling of samples should be minimised to avoid contamination with dust.
- For SIMS, outgassing from the resin caused problems, so samples should be loaded into the instrument loading chamber at least 12 hours before analysis.

The results to date from the study of positron emission tomography (PET) and micro-resistivity (MR) for measurement of *in situ* porosity suggest that neither technique is of strict relevance to the EP. PET requires the use of rather high activities and will require a significant development programme before being easily applied to rock samples. Nevertheless, PET shows promise for laboratory-based studies of porosity and flow, especially where the flow must be examined in real time. The micro-resistivity technique is probably of more relevance to EP (and already has a proven track record for visualising porosity in sandstones etc.) but clearly requires further development for use in fractured, low porosity crystalline rock. At the moment, however, changes in the sampling methodology of EP mean that no further work is needed on either technique within the confines of the project as, first, the stability of the excavated material is no longer a concern and, second, assessment of artefacts in porosity determination by destructive methods is being studied in another, related, GTS project (see MÖRI et al. 2003b).

## **6 Acknowledgments**

Many people have contributed to the ideas contained in this report and to the further development of these ideas. In addition to the authors of the individual chapters, the editors would like to express their thanks to I.G. McKinley and A. Gautschi (Nagra) and H. Umeki (JNC, now NUMO) for their support and patience, H. Kawamura (Obayashi) for his initial collaboration, T. 'Dusch' Fierz (Solexperts) and M. Mazurek (University of Berne) for general support and inspiration, SIKa AG (Zürich) for their patient co-operation at all times during resin development, A.E. Milodowski (BGS) for BGS liaison, C. Degueldre and S.A. Short (PSI) for PSI liaison and F.B. Neall (Neall Consulting) for general editorial assistance. Finally, thanks to Nagra/GNW and JNC for funding the work described here.



## 7 References

- AKSOYOGLU, S., BAJO, C. & MANTOVANI, M. (1991): Batch Sorption Experiments with Iodine, Bromine, Strontium, Sodium and Caesium on Grimsel Mylonite. Nagra Technical Report NTB 91-06. Nagra, Wettingen, Switzerland.
- ALEXANDER, W.R. & KAWAMURA, H. (eds.) (1992): Grimsel Test Site – The Grimsel migration experiment, Phase I of the excavation project: Feasibility study. Unpubl. Nagra Internal Report. Nagra, Wettingen, Switzerland.
- ALEXANDER, W.R., BRADBURY, M.H., MCKINLEY, I.G., HEER, W., EIKENBERG, J. & FRICK, U. (1992): The current status of the radionuclide migration experiment at the Grimsel Underground Rock Laboratory. *Sci. Basis Nucl. Waste Manag.* XV, 721-728.
- ALEXANDER, W.R., FRIEG, B., OTA, K. & BOSSART, P. (1996): The RRP Project – Investigating radionuclide retardation in the host rock. *Nagra Bulletin* 27 (June, 1996), 43-55. Nagra, Wettingen, Switzerland.
- ALEXANDER, W.R., OTA, K., MÖRI, R. & MCKINLEY, I.G. (2003a): Synthesis of the results of the 15 year Nagra-JNC Radionuclide Migration Programme. *Geochem. Trans.* (*in prep.*).
- ALEXANDER, W.R., SMITH, P.A. & MCKINLEY, I.G. (2003b): Modelling radionuclide transport in the geological environment: a case study from the field of radioactive waste disposal. Chapter 5 *in*: Scott, E.M. (ed.): *Modelling radioactivity in the environment*. Elsevier, Amsterdam, The Netherlands (*in press*).
- BAEYENS, B. & BRADBURY, M. (1989): Selectivity coefficients and estimates of *in-situ* sorption values for mylonite. *In*: Bradbury, M. (ed.): *Grimsel Test Site – Laboratory investigations in support of the migration experiments*. Nagra Technical Report NTB 88-23. Nagra, Wettingen, Switzerland
- BAILEY, D.L. & MEIKLE, S.R. (1994): A Convolution Subtraction Scatter Correction Method for 3D PET. *Phys. Med. Biol.* 39.
- BAJO, C., HOEHN, E., KEIL, R. & BAEYENS B. (1989): Chemical characterisation of the groundwater from fault zone AU 96m. *In*: Bradbury, M. (ed.): *Grimsel Test Site – Laboratory investigations in support of the migration experiments*. Nagra Technical Report NTB 88-23. Nagra, Wettingen, Switzerland.
- BARRETT, H.H. & SWINDELL, W. (1981): *Radiological Imaging: Theory of Image Formation, Detection and Processing*. Academic Press, New York.
- BASTON, G.M.N., BERRY, J.A. & BROWNSWORD, M. (1995): GTS-RRP(EP): Batch experiments to define the degree of kinetic hindrance to tracer sorption in the MI experimental shear zone, GTS – The case for Co, Eu, Np, Se, Tc and U. Unpubl. Nagra Internal Report. Nagra, Wettingen, Switzerland.
- BERRY, J.A., COWPER, M.M., GREEN, A., JEFFERIES, N.L. & LINKLATER, C.M. (1990): Sorption of Radionuclides on Mineral Surfaces. *Proceedings of the 3rd International Conference on Nuclear Fuel Processing and Waste Management (RECOD 91)*, Sendai, Japan, 988-993.

- BISCHOFF, K., WOLF, K. & HEIMGARTNER, B. (1987): Hydraulische Leitfähigkeit, Porosität und Uranrückhaltung in Bohrkernproben von Böttstein und Grimsel – Bohrkern-Infilitrationsversuche. Nagra Technical Report NTB 85-42, Nagra, Wettingen, Switzerland, also published as EIR Bericht No. 628, Paul Scherrer Institute, Villigen, Switzerland.
- BOSSART, P., MAZUREK, M., HELLMUTH, K.-H., SCHNEEBELI, M. & SITAARI-KAUPPI, M. (1991): Grimsel Test Site – Structural geology and water flow paths in the migration shear zone. Nagra Technical Report NTB 91-12. Nagra, Wettingen, Switzerland.
- BOYD, G.E. & LARSON, Q.V. (1983): Solvent extraction with complex-forming agents of Tc in lower oxidation states. *Gmelin Handbook of Inorganic Chemistry – Tc Technetium, Supplement Vol. 2, Metal. Alloys. Compounds. Chemistry in Solution, System Number 69*, 270-273.
- BRACE, W.F., ORANGE, A.S. & MADDEN, T.R. (1965): The effect of pressure on the electrical resistivity of water saturated crystalline rocks. *J. Geophys. Res.* 70, 5669-5678.
- BRADBURY, M.H. & BAEYENS, B. (1992): Modelling the sorption of Cs – Application to the Grimsel Migration Experiment. PSI Annual Report 1992, Annex IV, 59-64. Paul Scherrer Institute, Villigen, Switzerland.
- BROWN, P.L., HAWORTH, A., SHARLAND, S.M. & TWEED, C.J. (1990): HARPHRQ – A geochemical speciation program based on PHREEQE. Nirex Report (NSS/R188). Nirex, Harwell, UK.
- CHENERY, S. & COOK, J.M. (1993): Determination of rare earth elements in single mineral grains by laser ablation microprobe-inductively coupled plasma mass spectrometry. *J. Anal. Atom. Spectr.* 8, 299-303.
- COOPER, H.H. & JACOB, C.E. (1946): A generalized graphical method for evaluating formation constants and summarizing well-field history. *Am. Geophys. Union Trans.* 27, 526-534.
- DEY, A. & MORRISON, H.F. (1982): Resistivity modelling for arbitrarily shaped three-dimensional structures. *Geophys.* 44, 753-780.
- EVANS, C.J. (1980): The seismic and electrical properties of crystalline rocks under simulated crustal conditions. Ph.D. Thesis, Univ. of East Anglia, 293 pp.
- FIERZ, TH. (1997): GTS-EP – Design and construction of a triple packer system with integrated tracer injection. Unpubl. Nagra Internal Report. Nagra, Wettingen, Switzerland.
- FRICK, U., ALEXANDER, W.R., BAEYENS, B., BOSSART, P., BRADBURY, M.H., BÜHLER, CH., EIKENBERG, J., FIERZ, TH., HEER, W., HOEHN, E., MCKINLEY, I.G. & SMITH, P.A. (1992): Grimsel Test Site: The radionuclide migration experiment – Overview of the investigations 1985-1990. Nagra Technical Report NTB 91-04. Nagra, Wettingen, Switzerland.
- GOLDSTEIN, J.I., NEWBURY, D.E., ECHLIN, P., JOY, D.C., FIORI, C. & LIFSHIN, E. (1981): Scanning electron microscopy and X-ray microanalysis – A text for Biologists. Materials Scientists and Geologists. Plenum Press, New York & London.

- JACKSON, P.D., BUSBY, J.P., RAINSBURY, M., REECE, G. & MOONEY, P. (1990): The potential of electrical resistivity methods to detect hydraulically connected fractures. *In*: Baria, R. (ed.): Hot Dry Rock. Camborne School of Mines International Conference, Robertson Scientific Publications, 520-532.
- JACKSON, P.D., FLINT, R.C. & BALL, J.K. (1994): A feasibility study on the use of micro-resistivity core imaging to detect connected porosity in granodiorite from the GTS. *In*: The Grimsel Test Site Radionuclide Retardation Project (sub-project Excavation Project), Part 2. Unpubl. Nagra Internal Report. Nagra, Wettingen, Switzerland.
- KICKMAIER, W., ALEXANDER, W.R., VOMVORIS, S. & MCKINLEY, I.G. (2001): Grimsel 2000 – Status of international projects at the Grimsel Test Site (GTS). *Sci. Basis Nucl. Waste Manag.* XXIV, 893-900.
- MCKINLEY, I., ALEXANDER, W.R., BAJO, C., FRICK, U., HADERMANN, J., HERZOG, F.A. & HOEHN, E. (1988): The radionuclide migration experiment at the Grimsel Rock Laboratory, Switzerland. *Sci. Basis Nucl. Waste Manag.* XI, 179-187.
- MAGUIRE, R.P. & MISSIMER, J.H. (1993): PET Scanner and Blood Count Calibration Factors. PSI Unpubl. Internal Report. Paul Scherrer Institute, Würenlingen and Villigen, Switzerland.
- MEYER, J., MAZUREK, M. & ALEXANDER, W.R. (1989): Petrographic and mineralogical characterisation of fault zones AU96 and AU126. Chap. 2 *in*: Bradbury, M. (ed.): Grimsel Test Site – Laboratory investigations in support of the migration experiments. Nagra Technical Report NTB 88-23. Nagra, Wettingen, Switzerland.
- MÖRI, A., FRIEG, B., OTA, K. & ALEXANDER, W.R. (eds.) (2003a): The Nagra-JNC *in situ* study of safety relevant radionuclide retardation in fractured crystalline rock III: The RRP project final report. Nagra Technical Report NTB 00-07 (*in press*). Nagra, Wettingen, Switzerland.
- MÖRI, A., SCHILD, M., SIEGESMUND, S., VOLLBRECHT, A., ADLER, M., MAZUREK, M., OTA, K., HAAG, P., ANDO, T. & ALEXANDER, W.R. (2003b): Grimsel Test Site: The Nagra-JNC *in situ* study of safety relevant radionuclide retardation in fractured crystalline rock IV: The *in situ* study of matrix porosity in the vicinity of a water-conducting fracture. Nagra Technical Report NTB 00-08. Nagra, Wettingen, Switzerland.
- OTA, K., AMANO, K. & ANDO, T. (1999): Brief overview of *in situ* contaminant retardation in fractured crystalline rock at the Kamaishi *in situ* test site. *In*: Proceedings of an international Workshop for the Kamaishi *in situ* Experiments, Kamaishi, Japan, 24 – 25<sup>th</sup> August 1998. JNC Technical Report JNC TN7400 99-007, 67-76. JNC, Japan.
- OTA, K., MÖRI, A., ALEXANDER, W.R., FRIEG, B. & SCHILD, M. (2003): Influence of the mode of matrix porosity determination on matrix diffusion calculations. *J. Contam. Hydrol.* 61, 131-145.
- PARKHOMENKO, E.I. (1967): Electrical properties of rocks. Plenum Press, New York, 1967, 314 pp. Translated from Russian and edited by G.V. Keller.
- RABER, E., GARRISON, J. & OVERSBY, V. (1983): The sorption of selected radionuclides on various metal and polymeric materials. *Rad. Waste Man. Nucl. Fuel Cycle* 41, 41-52.

- SMITH, P.A., ALEXANDER, W.R., KICKMAIER, W., OTA, K., FRIEG, B. & MCKINLEY, I.G. (2001a): Development and testing of radionuclide transport models for fractured rock – Examples from the Nagra/JNC radionuclide migration programme in the Grimsel Test Site, Switzerland. *J. Contam. Hydrol.* 47, 335-348
- SMITH, P.A., ALEXANDER, W.R., HEER, W., FIERZ, T., MEIER, P.M., BAEYENS, B., BRADBURY, M.H., MAZUREK, M. & MCKINLEY, I.G. (2001b): Grimsel Test Site – Investigation Phase IV (1994-1996): The Nagra-JNC in situ study of safety relevant radionuclide retardation in fractured crystalline rock I: Radionuclide migration experiment – Overview 1990 – 1996. Nagra Technical Report NTB 00-09. Nagra, Wettingen, Switzerland.
- STROTHER, S.C., CASEY, M.E. & HOFFMANN, E.J. (1990): Measuring PET scanner sensitivity – Relating count rates to image signal-to-noise ratios using noise equivalent counts. *IEEE Trans. Nucl. Sci.* 37, 783-788.
- SYNOWIETZ, C. & SCHÄFER, K. (eds.) (1984): *Chemiker-Kalender*. 3<sup>rd</sup> completely revised edition, Springer Verlag, Berlin.
- TALVITIE, N.A. (1972): Electrodeposition of actinides for alpha spectrometric determination. *Anal. Chem.* 44, 280-283.
- THOMPSON, M., CHENERY, S. & BRETT, L. (1989): Calibration studies in laser ablation microprobe – inductively coupled plasma atomic emission spectroscopy. *J. Anal. Atom. Spec.* 4, 1-16.
- TOWNSEND, D.W., BYARS, L.G., DEFRISE, M., GEISSBUHLER, A., MISSIMER, J., RODDY, R., BRUN, T., MINTUN, M.A. & NUTT, R. (1993): Design and performance of a rotating positron tomograph, RPT-2. Contribution to IEEE Nuclear Science and Medical Imaging Symposium, San Francisco 1993.
- VOMVORIS, S. & FRIEG, B. (eds.) (1992): Grimsel Test Site – Overview of Nagra field and modelling activities in the ventilation drift 1988 – 1990. Nagra Technical Report NTB 91-34. Nagra, Wettingen, Switzerland.
- WATANABE, K., TAKEDA, S., YAMABE, T., ISHIYAMA, K. & BOSSART, P. (1993): Displacements of fractures during an *in situ* freezing and thawing test. *In: Proceedings of an International Symposium on the Assessment and Prevention of Failure Phenomena in Rock Engineering*, 5-7<sup>th</sup> April 1993, Istanbul, Turkey.
- WEAST, R.C. (ed.) (1980): *CRC Handbook of chemistry and physics*. CRC Press. Inc. Boca Raton, FL, USA.

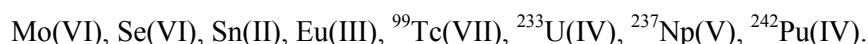
## Appendix A: Sample production and doping

*C. Degueldre, S.A. Short, H. Dollinger & P. Bossart*

For the purpose of testing the analytical techniques foreseen in the preliminary phase of the Grimsel Excavation Project (EP) numerous samples have been contacted with Grimsel water spiked with tracers. These samples were prisms of:

- 1) Mylonite
- 2) Granodiorite
- 3) Synthetic fault gouge / epoxy resin
- 4) Natural fault gouge /epoxy resin.

The samples are  $1 - 2 \times 1 - 2 \times 1 - 2$  cm, mounted on plastic stoppers and dipped in tracer spiked Grimsel water for a period of 3 months in a controlled atmosphere glove box. Spikes of tracer were evaporated in plastic test tubes (50 mL) prior to adding 50 mL Grimsel water. The tracers were (with assumed speciation):



The pH was 9.6 and remained almost constant during the 3 month test ( $9.6 \pm 0.4$ ). The Eh was also determined and was  $-150 \pm 30$  mV vs Standard H<sub>2</sub> Electrode. After the 3 month sorption period, the samples were separated and 20 mL of solution from each test was stored in different test tubes and acidified (1 % HNO<sub>3</sub>).

Each rock sample was separated from the water phase and the wet meniscus was also separated using a filter paper at the side of the sample. The sample was dried in controlled atmosphere and then placed in a laminar fume hood for recording photographically.

Note: since the exercise deals with a 3D presentation of the analytical results during the main phase of the exercise, the description of the sample must be presented within a matrix form:

$$(x, y, z, a_1, \dots, a_i, C_1, C_2, C_3 \dots G_j)$$

where

x, y, z are the coordinates

a<sub>1</sub> ...a<sub>i</sub> are properties (e.g. microporosity)

C<sub>1</sub>...G<sub>j</sub> are major elements and tracer nuclide concentrations.

## **Appendix B: Trial evaluation of LAM-ICP-MS analysis of doped rock samples from the GTS**

*M.T. Styles, A.E. Milodowski, S.R. Cheney, D.J. Bland and M.R. Gillespie*

### **B.1 Petrographic characterisation**

#### **B.1.1 General**

Upon receipt, each of the samples was observed and photographed under an optical stereo-zoom binocular microscope (Wild M400 Photomicroscope). These optical observations, coupled with additional information from scanning electron microscopy (SEM), backscattered scanning electron microscopy (BSEM), supported by energy-dispersive X-ray microanalysis (EDXA) were used to identify the mineralogy of the sample surface. A4-size optical photographs of the reacted sample block surface were produced and used as locational aids for subsequent LAM-ICP-MS analysis.

#### **B.1.2 Scanning electron microscopy**

The surface of each sample studied was initially observed by SEM, using both secondary electron imaging (SEI) and backscattered scanning electron (BSEM) imaging modes. SEM observations were made using a Cambridge Instruments Stereoscan S250 SEM instrument equipped with a KE-Developments Ltd. 4-element solid-state backscattered electron detector. Mineral identification was made by qualitative examination of the characteristic energy-dispersive X-ray spectra recorded during observation of a given mineral grain. Energy-dispersive X-ray analysis (EDXA) was carried out using a Link Systems 860 EDXA spectrometer fitted to the SEM instrument. Observations were carried out at a range of electron beam excitations from 10 to 20 kV.

The theoretical aspects of SEM techniques and their interpretation are discussed in detail by GOLDSTEIN et al. (1981). SEI images are produced by imaging low-energy secondary electrons produced in the surface of the sample under electron beam excitation. The images produced are analogous to reflected light images (with the electron detector having the 'appearance' of the 'light source') and are a function of the surface topography: surfaces oriented towards the electron detector appear bright, whereas surfaces oriented away from the electron detector appear in shadow. SEI observations therefore provide topographic information on material surfaces. BSEM images are produced by imaging high-energy primary beam electrons that are backscattered or reflected from the material surface, or just beneath the surface. The backscattering effect is primarily a function of the atomic mass and density of the material, although, it is also influenced to some extent by topographic effects. The greater the average atomic number and/or density of the material, the greater the backscatter coefficient, and consequently, the brighter the BSEM image appears. BSEM images therefore provide useful compositional information on the distribution of different phases on the surface of materials being examined.

## **B.2 Electron microprobe characterisation**

### **B.2.1 Methodology**

Electron microprobe analysis (EMPA) characterisation was carried out for two purposes:

- 1) Microchemical x-ray mapping of selected samples to investigate mineralogical complexity and distribution of major chemical components to give an indication of the representativeness of other investigations.
- 2) Quantitative point analyses of the minerals present to be used in the calibration of the laser ablation analyses.

Electron microprobe studies are normally carried out on flat polished specimens and all established techniques and corrections procedures are based on this assumption. The samples used in this study were fracture surfaces that are neither flat nor polished which introduces various errors and difficulties. Where this affects the results obtained it will be discussed at the appropriate point. The samples are not conductive to electricity and hence have to be coated with carbon to dissipate the charge induced by the electron beam. This was not very effective on the loose-surfaced natural and synthetic fault gouge samples and severe charging problems were encountered.

All the work described in this section was carried out using a Cameca SX50 computer controlled electron microprobe fitted with three wavelength-dispersive (WD) spectrometers.

#### **B.2.1.1 Microchemical X-ray mapping**

Microchemical X-ray mapping was carried out by making qualitative analyses on a matrix of  $512 \times 512$  points with the distance between points selected according to the area of sample to be studied. In this case the distance was 18  $\mu\text{m}$  for the low magnification maps and 2  $\mu\text{m}$  for high magnification, achieved by moving the specimen stage between analyses. If required, maps can be made at higher magnification by scanning the electron beam while the sample is in a fixed position. The dwell time at each point is selected according to the detection limits required and for the major elements studied here 5 ms was used. A fine-focussed electron beam, an accelerating voltage of 15 kV and a beam current (Faraday cup) of 55 nA was used throughout. Three elements (one per spectrometer) can be collected simultaneously, with several passes made if more elements are studied. Data collection is carried out using the Cameca software CIAP (Computer controlled Image Acquisition Program).

The data collected are raw X-ray counts from the spectrometers. These are processed and displayed using VISIVIEW, a Cameca customised version of the image processing system VISILOG by the French company Noesis. The data are displayed as single element colour images where the number of counts in a pixel is represented according to a rainbow colour scale, the lowest intensities are magenta and the highest are red. The data in each image are normalised to utilise the colour range and hence the colour scale is a relative scale for each image and the absolute intensity varies from one to another.

The WD spectrometers used have a small depth of focus, much less than the topography on some of the samples which means that the counts from areas out of focus are much lower than normal. This causes a contour-like banded effect on the images due to the high surface relief of most of the samples.

### **B.2.1.2 Quantitative point analysis**

Quantitative EMPA point analyses of the main mineral types in the selected samples were made using the Cameca QUANTIVIEW 3 software. Analyses were made using a fine-focussed electron beam, an accelerating voltage of 15 kV, a beam current of 20 nA and count times of 10 seconds peak and 5 seconds background. Matrix correction use the Phi-Rho-Z method. A range of natural minerals, synthetic oxides and pure metals were used as standards for calibration.

Where possible parts of the minerals that were as smooth and near to flat were selected for analysis to reduce errors. This was not always possible and is the cause of the variation in totals and some unusual element ratios found. To even out these variations, analyses are also presented normalised to the idealised total expected from EMPA.

## **B.3 Laser ablation microprobe – inductively coupled plasma – mass spectrometry (LAM-ICP-MS) analysis**

### **B.3.1 Instrumentation**

The principal behind this technique is that the trace elements in the material to be examined are determined by placing the sample in an ablation cell and removing a small sub-sample with the laser ablation microprobe (LAM). The LAM system was designed and built by the Department of Chemistry, Birkbeck College, University of London. The design and basic operation are described in United Kingdom Patent No. 91066337.0, Serial 2254444. The ablated material is transferred to the inductively coupled plasma – mass spectrometer (ICP-MS) in a stream of argon, passing through a polythene tube that connects the ablation cell to the ICP torch. This material is then analysed by a VG Plasmaquad 2+ ICP-MS. The ICP-MS uses an inductively coupled plasma to ionise the test material and a quadruple mass spectrometer to scan for ions with a mass to charge ratio in the range 6 – 250. All system parameters are monitored continuously to provide safe operation. The machine is completely controlled by a Compaq 386 Model 20e computer through dedicated ICP-MS software, with analytical results being stored on the hard disc. The LAM and the ICP-MS are interfaced using the 'dual gas flow' method as described in THOMPSON et al. (1989) and CHENERY & COOK (1993).

### **Test material preparation**

The only requirements are that the test material will fit inside an ablation chamber (about 10 cm diameter and 2 cm deep) and has a flat enough surface on which to focus the optical microscope and laser. However, the preferred sample types are: a thin section at least 30 µm thick, a polished block, single grains mounted on a slide with double sided sticky tape. The samples examined during this study were not ideal for the best results.

### **Aqueous standardisation**

Aqueous LAM-ICP-MS standards for calculating element/isotopic sensitivities are usually made up from commercial multi-element ICP standards that are certificated and traceable to international standards. Individual element solutions of appropriate quality may be used if chemical compatibility or calibration ranges require this. Times ten serial dilutions are performed by mass using a balance and an autopipette whose accuracy and precision are controlled by BGS QA Procedures.

### Analysis Procedure

The LAM and the ICP-MS are interfaced as described under instrumentation. The sample was placed inside the laser ablation cell. The ICP-MS was purged and the laser ablation cell was also purged by an independent gas stream. The ICP-MS was lit using a conventional gas flow through the nebuliser system and a minimum gas flow through the laser ablation cell. The ICP-MS ion optics were then tuned. The nebuliser gas flow was slowly reduced to  $0.4 \text{ L min}^{-1}$  and the ablation cell gas flow increased to maximise the tuning signal. This would typically be  $0.6 - 0.7 \text{ L min}^{-1}$ . The system was left to stabilise for 30 minutes.

Standard solutions and blank were analysed using Time Resolved Analysis (TRA) software version 3.2.1A. These solutions were analysed at least once during each half day of analysis time (i.e. typically the beginning and end of each day). The first material to be ablated at the beginning of the day and the last material ablated at the end of the day was a reference material (e.g. NIST612 glass, see Tab. B.1 and B.2).

During LAM analysis the optical microscope was focussed on the test material at a point of interest. The TRA software was activated and at least 20 time slices of background signal were acquired before the laser was fired. Once the desired amount of material was ablated the next analysis spot was chosen and the process repeated.

### Data Processing Procedure

Using the TRA software, each spectrum was plotted as response versus time. The spectrum was divided into two or more parts of equal time length which represented peaks and background. They were then integrated and saved as separate files.

A custom written program subtracted the background from the peak signal and then corrected the result for isotopic abundance using the standard values. From the background signal a detection limit (d.l.) was calculated. If the background counts were less than 10,000, the d.l. is 10 standard deviations calculated from Poissonian statistics, but if the background counts were greater than 10,000, then the d.l. is taken to be 30 % of the background. All the above data were then saved to the corrected response data file.

From the corrected response data for the aqueous standards, the relative sensitivity, i.e. response/concentration of the different elements and their isotopes of interest, were calculated. In this study, a number of isotopes not naturally occurring was determined. As solution tracers were not available for calibration, an estimate of their sensitivities was made. For  $^{99}\text{Tc}$  the sensitivity was estimated from nearby mass  $^{88}\text{Sr}$ , while for  $^{233}\text{U}$ ,  $^{237}\text{Np}$  and  $^{242}\text{Pu}$ , the sensitivity of  $^{238}\text{U}$  was used. It may be expected that results based on these assumptions will be accurate to within a factor of 2 – 3.

Finally, the data are normally corrected using an internal standard element program. The concentration of the internal standard element must be determined independently either from stoichiometry or a technique such as EMPA.

The LAM-ICP-MS results on the analysed spiked mineral samples are presented in Tab. B.3 to B.11.

Tab. B.1: LAM-ICP-MS results on NIST611 glass reference material

	<b>Mg</b>	<b>Al</b>	<b>Ca</b>	<b>Ti</b>	<b>Mo</b>	<b>Sn</b>	<b>Eu</b>	<b>Sm</b>
	519	10000	102000	631			489	482
	535	10000	102000	618			517	511
	565	10000	101000	660			525	521
	649	10000	103000	682			453	458
	626	10000	115000	731			439	443
	506	10000	106000	660			444	435
	538	10000	84700	803			466	479
	473	10000	78000	571			439	446
	495	10000	78900	580			470	464
	452	10000	119000	292	582	806	421	
	428	10000	112000	587	474	1020	456	
	483	10000	104000	547	520	1020	440	
	318	10000	90500	765	510	560	428	
	410	10000	89500	510	510	540	427	
	460	10000	85500	585	515	605	424	
	560	10000	97500	412	455	620	455	
	898	10000	78400	522	525	567	453	
	546	10000	84100	564	590	613	471	
	478	10000	81300	474	584	612	471	
	347	10000	57700	488	424	355	307	
	395	10000	51700	467	355	361	308	
	287	10000	48500	471	321	366	327	
<b>Average</b>	499	10000	89559	574	490	619	438	471
<b>Std. dev.</b>	127	0	19304	119	83	218	57	30
<b>RSD</b>	26	0	22	21	17	35	13	6
<b>Expected</b>	500*	10000	86000	437	500*	500*	500*	500*

\* nominal

Tab. B.2: LAM-ICP-MS results on NIST611 glass reference material

	<b>Mg</b>	<b>Al</b>	<b>Ca</b>	<b>Sr</b>	<b><sup>99</sup>Tc</b>	<b>Eu</b>	<b><sup>233</sup>U</b>	<b><sup>237</sup>Np</b>	<b>U</b>	<b><sup>242</sup>Pu</b>
	614	10600	87400	658	< 1	480	< 3	<	1600	< 3
	538	10600	87200	665	< 1	505	< 3	< 4	1620	< 3
	550	10600	87500	666	< 1	543	< 3	< 4	1720	< 3
	646	10600	85700	682	< 3	472	< 9	< 15	2420	< 17
	676	10600	90900	672	< 1	457	< 4	< 8	1590	< 8
	625	10600	96300	665	< 1	459	< 3	< 5	1470	< 6
	625	10600	96300	665	< 1	459	< 3	<	1470	< 6
	625	10600	96300	665	< 1	459	< 3	< 5	1470	< 6
	625	10600	96300	665	< 1	459	< 3	< 5	1470	< 6
	504	10600	83100	611	< 1	509	< 1	< 1	546	< 1
	555	10600	83600	625	< 1	553	< 1	< 1	601	< 1
	528	10600	84400	643	< 1	633	< 1	< 1	501	< 1
	599	10600	87200	506	< 1	286	< 3	< 3	541	< 3
	610	10600	87800	519	< 1	292	< 2	< 2	604	< 2
	550	10600	88400	516	< 1	275	< 2	< 2	492	< 2
	549	10600	92300	645	< 1	1030	< 3	< 3	542	< 3
	517	10600	89700	668	< 1	1010	< 2	< 3	475	< 2
	529	10600	94400	639	< 1	1050	< 2	< 3	483	< 2
	468	10600	87800	453	< 1	311	< 1	< 1	429	< 1
	493	10600	92300	487	< 1	345	< 1	< 1	436	< 1
	515	10600	91200	494	< 1	365	< 1	< 1	467	< 1
	651	10600	84900	689	< 1	960	< 1	< 1	1040	< 1
	714	10600	84700	696	< 1	1040	< 1	< 1	1070	< 1
	746	10600	92200	819	< 1	1180	< 1	< 1	1170	< 1
	541	10600	69700	556	< 1	408	< 1	< 1	499	< 1
	602	10600	74900	576	< 1	480	< 1	< 1	531	< 1
	684	10600	86600	650	< 1	591	< 1	< 1	659	< 1
	486	10600	61400	541	< 1	689	< 2	< 1	633	< 1
	507	10600	62400	516	< 1	668	< 1	< 1	675	< 1
	494	10600	76700	558	< 2	712	< 3	< 3	701	< 3
	692	10600	64600	598	< 1	567	< 1	< 1	556	-
	562	10600	67500	565	< 1	615	< 1	< 1	622	-
	602	10600	70400	580	< 1	689	< 1	< 1	822	-
	509	10600	47400	549	< 1	533	< 1	< 1	467	-
	614	10600	51200	550	< 1	655	< 1	< 1	483	-
	632	10600	56100	645	< 1	819	< 1	< 1	526	-
<b>Mean</b>	583	Int. Std.	81578	608		599			872	
<b>Std. dev.</b>	71	Int. Std.	13405	77		240			506	
<b>RSD</b>	12	Int. Std.	16	13		40			58	
<b>No. of samples</b>	36									
<b>Expected</b>	500*		85700	512		500*			462	

\* nominal

Tab. B.3: LAM-ICP-MS results on samples spiked with <sup>99</sup>Tc

Mineral	Mg	Al	Ca	Fe	Sr	<sup>99</sup> Tc	Eu	<sup>233</sup> U	<sup>237</sup> Np	<sup>233</sup> U	<sup>242</sup> Pu	Spot/ Raster
<b>Sample Tc8N15</b>												
Biotite?	13700	100000	6040	32700	82	< 1	< 1	< 3	< 6	< 4	< 4	S
Biotite?	14900	100000	4380	35300	90	< 1	< 1	< 4	< 6	< 3	< 3	S
Biotite?	17200	100000	8500	45600	155	< 1	< 1	< 2	< 3	< 5	< 2	R
Matrix	41600	100000	20700	206000	138	< 2	< 2	< 8	< 20	< 11	< 8	S
Matrix	15700	100000	20000	38900	72	< 1	< 1	< 1	< 2	7	< 1	R
Matrix	25700	100000	14600	86400	182	< 1	< 1	< 6	< 6	< 13	< 6	S
Matrix	14300	100000	3900	26300	62	< 1	0.6	< 1	< 1	7	< 1	R
<b>Sample Tc4G14</b>												
Biotite?	44500	100000	1600000	503000	1640	< 2	7	< 10	< 15	44	< 6	S
Biotite	45700	100000	4630	257000	17	< 1	< 1	< 2	< 4	< 2	< 2	S
Biotite	40100	100000	7850	226000	16	< 1	< 1	< 1	< 1	7	< 1	S
Biotite	48900	100000	3870	279000	23	< 1	< 1	< 1	< 1	< 2	< 1	R
K-feldspar	< 100	100000	4940	10600	35	< 1	< 1	< 2	< 3	< 2	< 2	S
K-feldspar	< 100	100000	6170	2370	136	< 1	< 1	< 3	< 4	< 2	< 3	R
Biotite	37800	100000	2860	241000	18	< 1	< 1	< 3	< 5	< 4	< 4	S
Biotite	40200	100000	2320	233000	5	< 1	< 1	< 3	< 5	< 2	< 3	S
Sphene?	4900	100000	1130000	163000	< 20	< 12	47	< 72	< 97	865	< 50	S
Sphene?	7900	100000	891000	113000	142	< 6	42	< 24	< 36	678	< 27	S
Biotite	39600	100000	< 400	208000	58	< 3	< 2	< 12	< 18	< 11	< 9	S
Biotite	38500	100000	45100	501000	86	< 17	< 11	< 67	< 128	< 75	< 59	S
<b>Sample Tc2M5</b>												
Muscovite	23000	100000	2370	48400	11	< 1	< 1	< 2	< 2	< 2	< 2	S
Muscovite	17700	100000	2240	36900	52	< 1	< 1	< 2	< 2	< 2	< 2	R
Muscovite	13700	100000	< 220	34100	37	< 1	< 1	< 2	< 4	< 4	< 4	S
Muscovite	13500	100000	3490	26600	10	< 1	< 1	< 2	< 2	< 2	< 2	R
Biotite	19300	100000	33000	60000	62	< 6	< 5	< 16	< 14	< 18	< 18	S
Muscovite?	16500	100000	4070	30300	102	< 2	< 2	< 3	< 5	< 18	< 7	S
Biotite	19400	100000	7620	57300	109	< 7	< 6	< 15	< 17	< 18	< 15	S
Biotite	80300	100000	4000	143000	24	< 2	< 1	< 4	< 5	< 6	< 5	R
Biotite	74500	100000	1830	143000	57	< 2	< 1	< 3	< 2	< 4	< 4	R
Muscovite	11800	100000	6350	24700	8	< 1	< 1	< 3	< 3	< 4	< 4	S
Muscovite	16000	100000	2100	31500	26	< 1	< 1	< 2	< 2	< 3	< 3	R

Tab. B.4: LAM-ICP-MS results on samples spiked with <sup>237</sup>Np

Mineral	Mg	Al	Ca	Fe	Sr	<sup>99</sup> Tc	Eu	<sup>233</sup> U	<sup>237</sup> Np	<sup>233</sup> U	<sup>242</sup> Pu	Spot/ Raster
<b>Sample Np2M22</b>												
K-feldspar	1160	100000	6770	10500	45	< 1	29	< 2	< 4	< 3	< 3	S
Albite in K-feldspar	544	100000	7620	6870	48	< 1	< 1	< 2	< 3	< 3	< 3	S
K-feldspar	2580	100000	6230	12800	82	< 1	< 1	< 1	< 3	< 2	< 1	S
<b>Sample Np4G8</b>												
Biotite?	< 890	100000	24800	19000	317	< 8	< 7	< 20	< 30	< 19	< 16	S
Biotite	35500	100000	4430	191000	33	< 2	< 1	< 6	< 4	< 4	< 4	S
K-feldspar	< 360	100000	44000	16700	<10	< 7	< 7	< 19	< 23	< 17	< 17	S
K-feldspar ?	24900	100000	207000	218000	349	< 5	< 5	< 8	38	< 16	< 7	R
K-feldspar	< 260	100000	16700	15600	21	< 4	< 3	< 8	< 9	< 11	< 6	R
Biotite	37600	100000	16500	246000	108	< 2	< 2	< 5	< 6	< 5	< 6	S
Biotite	43100	100000	< 550	233000	41	< 3	< 2	< 8	< 8	34	< 9	S
<b>Sample Np8N11</b>												
Fragment	11000	100000	41800	30800	54	< 1	< 1	< 1	6	< 1	< 1	S
Fragment	12900	100000	3150	33100	25	< 1	< 1	< 1	5	< 2	< 1	S
Fragment	12400	100000	5660	29100	12	< 1	< 1	< 1	< 2	< 1	< 1	S
Fragment	12400	100000	2510	24300	24	< 1	< 1	< 1	< 1	< 1	< 1	R
Large frag.	35600	100000	14500	192000	236	< 1	< 1	< 1	17	12	< 2	S
Large frag.	24000	100000	11700	128000	111	< 1	< 1	< 1	11	3	< 1	S
Large frag.	7990	100000	14400	63900	92	< 1	8	< 1	9	< 3	< 2	S
Large frag.	9380	100000	11400	36800	44	< 1	< 1	< 4	11	< 4	< 3	S
Large frag.	12700	100000	6260	37900	63	< 1	< 1	< 2	< 4	58	< 2	R
Large frag.	19100	100000	13800	48500	83	< 2	< 2	< 7	< 7	< 6	< 7	S
Large frag.	16600	100000	27100	81300	164	< 3	< 2	< 6	< 9	< 8	< 7	S
Mica frag.	18200	100000	48500	73700	837	< 1	< 1	< 3	64	< 3	< 2	S
Mica frag.	12900	100000	26700	29500	783	< 1	< 1	< 2	15	< 2	< 2	S
Mica frag.	60300	100000	37000	115000	1090	< 1	< 1	< 1	< 5	< 2	< 1	S
Green crush	25400	100000	23100	126000	167	< 1	< 2	< 3	< 12	< 8	< 3	S
Green crush	32000	100000	27100	174000	200	< 1	2	< 1	20	38	< 1	S
Green crush	30800	100000	147000	97700	209	< 15	< 19	< 38	< 50	< 44	< 38	S
Green crush	29500	100000	13800	158000	203	< 1	< 1	< 3	14	26	< 2	S
Green crush	21800	100000	25600	137000	89	< 1	< 3	< 2	23	< 6	< 2	S
Dark mica	51600	100000	8730	112000	111	< 1	7	< 2	8	27	< 2	S
Dark mica	65200	100000	31800	145000	167	< 2	< 3	< 6	22	< 7	< 6	S

Tab. B.5: LAM-ICP-MS results on samples spiked with <sup>233</sup>U

Mineral	Mg	Al	Ca	Fe	Sr	<sup>99</sup> Tc	Eu	<sup>233</sup> U	<sup>237</sup> Np	<sup>233</sup> U	<sup>242</sup> Pu	Spot/ Raster
<b>Sample U4G22</b>												
Biotite?	56300	100000	52500	260000	< 8	< 5	< 7	< 17	< 11	< 13	< 17	S
Biotite edge?	49100	100000	25300	252000	74	< 2	< 2	< 6	< 6	21	< 4	S
Biotite edge?	53400	100000	14100	241000	34	< 1	< 2	< 6	< 5	< 5	< 5	S
Biotite?	50200	100000	44700	262000	448	< 5	< 7	< 23	< 14	< 18	< 17	S
K-feldspar?	256	100000	20200	12900	96	< 1	< 1	< 2	< 2	< 2	< 2	S
K-feldspar?	763	100000	25900	26400	159	< 1	< 2	22	< 4	< 6	< 3	S
Biotite edge	44200	100000	7220	261000	51	< 1	< 1	14	< 2	< 2	< 2	S
Biotite	46300	100000	10900	230000	42	< 1	< 1	7	< 2	< 2	< 2	S
K-feldspar	472	100000	4950	9500	31	< 1	< 2	< 3	< 4	< 4	< 3	S
K-feldspar	215	100000	10700	5140	46	< 1	< 1	57	< 2	< 2	< 2	S
K-feldspar	1030	100000	17200	14400	71	< 1	< 1	< 8	< 2	< 2	< 1	S
<b>Sample U2M13</b>												
Quartz or K-feldspar?	285	100000	14600	12900	136	< 2	< 2	< 8	< 5	< 4	< 5	S
Quartz or K-feldspar?	133	100000	6510	7600	96	< 1	< 2	< 6	< 3	< 4	< 3	S
Quartz or K-feldspar?	1560	100000	10400	13600	146	< 1	< 1	20	< 2	< 3	< 2	S
Quartz or K-feldspar?	15300	100000	41800	92600	653	< 1	4	91	< 2	68	< 2	S
Biotite?	32400	100000	77400	133000	182	< 4	< 5	134	< 11	< 32	< 14	S
Biotite?	32000	100000	39400	118000	355	< 2	< 3	67	< 7	< 7	< 6	S
Biotite?	5900	100000	7920	28300	63	< 1	17	81	< 1	< 3	< 1	S
Biotite?	2210	100000	6070	20900	25	< 1	49	13	< 2	< 2	< 1	S
Biotite?	34000	100000	109000	182000	406	< 7	< 9	1140	< 34	< 31	< 25	S
Biotite?	1110	100000	7030	8270	44	< 1	< 1	40	< 2	< 2	< 2	S
Biotite?	23800	100000	15500	67500	187	< 1	4	43	< 3	< 4	< 4	S
Biotite?	7830	100000	21900	55800	125	< 1	< 1	122	< 2	70	< 2	S
<b>Sample U8N12</b>												
Matrix	33400	100000	10000	54500	227	< 1	< 1	13	< 1	4	< 1	S
Clast	25000	100000	12300	36100	277	< 1	< 1	11	< 1	10	< 1	S
Clast	17700	100000	10600	33000	362	< 1	1	2	< 1	37	< 1	S
Matrix	22000	100000	31900	52300	1130	< 1	2	7	< 1	16	< 1	S
Clast	27900	100000	10600	37300	220	< 1	< 1	7	< 1	8	< 1	S
Clast	22000	100000	5420	42000	154	< 1	1	4	< 1	7	< 1	S
Matrix	22400	100000	6870	41600	166	< 1	1	4	< 1	5	< 1	S
Clast	35900	100000	6850	51600	142	< 1	< 1	59	< 1	2	< 1	S
Matrix	34900	100000	6700	62400	199	< 1	< 1	5	< 1	4	< 1	S

Tab. B.6: LAM-ICP-MS results on samples spiked with <sup>242</sup>Pu

Mineral	Mg	Al	Ca	Fe	Sr	<sup>99</sup> Tc	Eu	<sup>233</sup> U	<sup>237</sup> Np	<sup>233</sup> U	<sup>242</sup> Pu	Spot/ Raster
<b>Sample Pu4G4</b>												
Muscovite	19600	100000	5940	87900	69	< 1	< 1	< 1	< 1	< 1	< 1	S
Mica	4020	100000	6700	13600	163	< 1	< 1	< 1	< 1	< 1	< 1	S
Albite?	4580	100000	9670	17700	191	< 1	< 1	< 1	< 1	< 1	< 1	S
Albite?	7950	100000	45100	50400	683	< 1	3	< 1	< 1	1	< 1	S
Mica	7870	100000	102000	83200	1160	< 1	5	< 1	< 1	139	< 1	S
Mica	3330	100000	21800	17300	405	< 1	1	< 1	< 1	< 1	< 1	S
Mica	17800	100000	540000	74600	268	< 1	24	< 1	< 1	34	< 1	S
K-feldspar	1750	100000	19800	12600	357	< 1	14	< 1	< 1	< 1	< 1	S
K-feldspar?	1870	100000	10100	8500	242	< 1	1	< 1	< 1	2	< 1	S
K-feldspar?	2620	100000	41500	9470	240	< 1	< 1	< 1	< 1	< 3	< 1	S
<b>Sample Pu2M20</b>												
Quartz rich	15200	100000	60200	28500	113	< 6	< 14	< 9	< 9	< 10	< 1	S
K-feldspar	5560	100000	17500	19200	216	< 1	7	< 1	< 1	< 2	< 1	S
Quartz rich	7820	100000	9160	17000	129	< 1	< 1	< 1	< 1	< 1	< 1	S
K-feldspar	27600	100000	8640	56100	171	< 1	< 1	< 1	< 1	190	< 21	S
Matrix	6340	100000	173000	35700	397	< 13	< 18	< 25	< 30	< 19	< 1	S
Matrix	13800	100000	7580	31700	170	< 1	< 1	< 1	< 1	< 1	< 1	S
Matrix	36000	100000	10800	79800	130	< 1	< 1	< 1	< 1	3	< 22	S
Matrix	20600	100000	131000	90600	441	< 11	< 14	< 25	< 22	70	< 1	S
Matrix	24600	100000	61100	46600	342	< 1	4	< 1	< 1	18	< 8	S
Mica	23500	100000	66300	97700	514	< 4	6	10	< 8	< 8	< 8	S
<b>Sample Pu8N23</b>												
Biotite?	41100	100000	25200	95600	418	< 1	7	< 1	< 1	< 1	< 1	S
Muscovite?	37500	100000	13200	90800	165	< 1	< 1	< 3	< 2	< 5	< 2	S
Matrix	8840	100000	37300	20000	34	< 1	2	< 1	< 1	6	< 1	S
Matrix	33700	100000	17200	84100	150	< 1	< 1	< 1	< 1	< 2	< 1	S
Matrix	28900	100000	13900	79500	171	< 1	3	< 1	< 1	7	< 1	S
Matrix	14000	100000	11900	38900	120	< 1	2	< 1	< 1	16	< 1	S

Tab. B.7: LAM-ICP-MS results on samples spiked with several elements

Mineral	Mg	Al	Ca	Fe	Sr	Mo	<sup>99</sup> Tc	Sn	Eu	<sup>233</sup> U	<sup>237</sup> Np	U	Spot/ Raster
<b>Sample C6M17</b>													
<b>Spike Elements: Mo, <sup>99</sup>Tc, Sn, Eu, <sup>233</sup>U, <sup>237</sup>Np</b>													
Mica	15100	100000	2270	28100	48	<1	<1	91	16	<1	<1	<1	S
Feldspar?	15300	100000	8330	22300	381	<1	<1	73	14	<1	<1	22	S
Biotite	22300	100000	5350	42600	218	<1	<1	183	40	2	<1	2	S
Biotite	19400	100000	7290	29100	137	<2	<1	41	33	<1	<1	2	S
Biotite	33100	100000	7130	65600	93	<1	<1	74	35	<1	<1	<1	S
Muscovite	11100	100000	3850	18600	128	5	<1	119	63	<1	<1	6	S
Muscovite	11800	100000	9820	21100	206	5	<1	244	76	<1	1	2	S
Feldspar?	24000	100000	3950	47800	98	2	<1	187	44	<1	<1	4	S
Feldspar?	24000	100000	7030	37900	196	<1	<1	186	64	<1	<1	11	S
Mica	34300	100000	8570	56200	133	<1	<1	281	99	2	<1	69	S
Mica	14900	100000	12200	21500	204	1	<1	199	50	1	<1	15	S
Mica	10100	100000	32600	32200	948	<1	<1	296	91	<1	<1	110	S
Mica	12200	100000	21100	28000	455	<1	<1	44	41	<1	<1	62	S
Feldspar?	18100	100000	4960	24800	121	<1	<1	107	26	<1	<1	5	S
<b>Sample C4M9</b>													
<b>Spike Elements: Mo, Sn, Eu, <sup>233</sup>U, <sup>237</sup>Np + (Se)</b>													
Biotite	59100	100000	6480	64700	213	<3	<1	105	121	3	<2	<1	S
Biotite	62200	100000	30000	76200	239	274	<9	722	285	67	<21	<9	S
Biotite	40200	100000	29000	40400	427	<3	<1	823	102	7	<3	5	S
Biotite	42500	100000	6240	51400	297	18	<2	231	128	17	<2	<2	S
Albite	435	100000	5800	1090	214	<2	<1	74	25	9	<1	<1	S
Albite	6130	100000	21700	17500	880	<2	<1	1070	223	12	<5	75	S
Albite	3010	100000	8590	5880	463	29	<1	127	428	18	13	<1	S
Muscovite	27000	100000	22100	29700	729	<2	<1	265	303	48	9	18	S
Muscovite	36500	100000	9570	42400	237	<2	<1	145	55	7	<2	<2	S
Muscovite	18700	100000	19600	17500	758	13	<1	236	494	27	18	<1	S
Muscovite	25200	100000	33000	35200	2380	18	<1	902	1140	57	44	75	S

Tab. B.8: LAM-ICP-MS results on samples spiked with Eu

Mineral	Mg	Al	Ca	Ti	Fe	Mo	Sn	Eu	Sm
<b>Sample Eu2M15</b>									
Muscovite	12000	100000	6130	896	20200	3	15	26	
Muscovite	12300	100000	8120	1230	26000	13	16	30	
Muscovite	13100	100000	14800	1320	34200	3	24	40	
Muscovite	14600	100000	7810	1160	33700	< 3	16	78	
Muscovite	12500	100000	5500	1180	27500	3	22	39	
Muscovite	10300	100000	8490	1080	23100	12	18	31	
Muscovite	13300	100000	5610	1550	32700	< 1.2	16	27	
Biotite	43100	100000	14000	5090	109000	60	64	42	
Biotite	22200	100000	13100	2740	53300	9	34	33	
Biotite	78200	100000	20100	8590	166000	< 14	34	32	
Biotite	30500	100000	17400	3180	75100	< 3	14	11	
Biotite	14400	100000	10900	1560	36200	< 1.7	20	14	
Albite?	25600	100000	406000	4150	177000	128	140	139	
<b>Sample Eu4G6</b>									
Biotite	47300	100000	124000	22500	436000			2330	42
Biotite	59700	100000	46900	14000	357000			848	6
Biotite	46600	100000	4650	10500	228000			95	< 0.32
Biotite	49600	100000	8320	12600	245000			144	< 0.56
Biotite	49100	100000	6820	12100	271000			485	8
K-feldspar	1340	100000	16700	1080	14200			387	< 0.40
K-feldspar	1390	100000	9330	306	9220			336	< 0.44
K-feldspar	1360	100000	11100	630	5700			244	3
K-feldspar	37	100000	7820	636	1910			47	< 0.45
K-feldspar	515	100000	3510	110	1780			98	< 0.36
K-feldspar	585	100000	15800	717	5920			284	< 0.51
<b>Sample Eu8N20</b>									
Matrix?	16300	100000	26700	3590	43700			158	< 0.99
Matrix?	25200	100000	10600	2720	88100			131	10
Matrix?	22300	100000	6730	2080	56900			30	1
Matrix?	44700	100000	15000	4840	162000			387	5
Matrix?	38200	100000	11300	2900	85800			117	2
Matrix?	12300	100000	15000	1210	32500			93	1
Matrix?	13600	100000	30200	1060	22600			198	5
Matrix?	23900	100000	17900	3360	65500			158	2
Matrix?	23500	100000	25600	5240	72000			162	36
Matrix?	85900	100000	76100	10900	327000			821	< 13.10
Matrix?	32400	100000	61700	2940	84300			306	12
Matrix?	26300	100000	16000	5800	73500			207	3
Matrix?	32600	100000	21000	3820	92400			193	17
Matrix?	133000	100000	60000	13300	444000			700	3
Matrix?	30600	100000	12900	3300	70500			127	2
Matrix?	16500	100000	3290	1640	35600			96	3
Mica?	26500	100000	12100	4190	79000			190	3
Matrix?	10500	100000	3120	932	18900			23	3
Matrix?	22300	100000	5770	2310	57800			99	6
Matrix?	6750	100000	18200	19200	14800			33	2
Matrix?	42300	100000	60100	5440	125000			1140	18

Tab. B.9: LAM-ICP-MS results on samples spiked with Mo

Mineral	Mg	Al	Ca	Ti	Fe	Mo	Sn	Eu
<b>Sample Mo2M11</b>								
Biotite	24300	100000	<1070	3830	59400	< 15	25	< 0.69
Biotite	29900	100000	<1490	2500	85300	19	< 25	< 0.85
Biotite	18200	100000	22800	1860	39100	< 3	20	< 0.42
Biotite	82400	100000	<2390	10400	193000	< 11	49	< 1.69
Biotite	42800	100000	31100	3840	89800	< 7	33	< 3
Biotite	43200	100000	12700	5350	83700	68	43	< 1.32
Muscovite	13700	100000	11600	2240	43200	< 13	41	< 0.57
Muscovite	16800	100000	41900	2320	49100	42	< 11	< 1.8
Muscovite	17900	100000	11600	2100	46600	12	27	< 0.36
<b>Sample Mo4G12</b>								
K-feldspar	42	100000	1570	89	1990	< 1	3	< 0.08
K-feldspar	44	100000	1400	30	1520	1	3	0
K-feldspar	149	100000	2820	100	669	3	< 1	< 0.08
K-feldspar	287	100000	1980	8	1200	< 1	3	1
K-feldspar	199	100000	174000	< 6	905	< 1	<6	< 0.24
K-feldspar	47	100000	< 44	26	272	1	1	1
K-feldspar	85	100000	485	159	941	15	8	4
K-feldspar	59	100000	1680	< 8	6630	10	13	< 0.35
<b>Sample Mo8N9</b>								
Matrix	32400	100000	9760	5580	74400	97	62	< 0.6
Matrix	20300	100000	3190	1990	37800	10	19	0
Matrix	13200	100000	6170	1480	37000	41	21	< 0.10
Matrix	28200	100000	7510	6830	75600	60	26	< 0.20
Matrix	14200	100000	5710	1600	30500	13	19	< 0.13
Biotite?	56600	100000	31200	6250	185000	82	44	< 0.84
Biotite?	28200	100000	34300	3040	51600	65	38	< 0.68
Matrix	20900	100000	1670	2330	31700	15	13	< 0.09
Matrix	13000	100000	9340	5050	27700	14	16	< 0.14
Matrix	26400	100000	5170	2500	39700	7	15	< 0.13
Matrix	22200	100000	3290	2960	41300	23	28	< 0.25
Matrix	23700	100000	1010	2770	54800	16	13	1

Tab. B.10: LAM-ICP-MS results on samples spiked with Sn

Mineral	Mg	Al	Ca	Ti	Fe	Mo	Sn	Eu
<b>Sample Sn2M12</b>								
Muscovite	11000	100000	5210	1130	23300	< 3	21	1
Biotite	37300	100000	12200	4940	123000	15	75	< 0.30
Biotite	12600	100000	6090	1820	33900	19	23	< 0.61
Biotite	27900	100000	10900	2560	72200	10	64	< 0.31
Biotite	28900	100000	11800	3230	65000	16	22	< 0.57
Biotite	31100	100000	10300	4630	72100	< 2	44	< 0.69
Biotite	30700	100000	9870	4430	82800	< 5	28	< 0.65
Muscovite	7850	100000	8190	664	20600	7	34	1
Muscovite	11700	100000	6630	1110	25300	< 1	19	< 0.21
Muscovite	9100	100000	7640	814	22900	< 1	20	2
<b>Sample Sn4G17</b>								
Biotite	35800	100000	11100	1230	618000	< 208	382	91
Biotite	42400	100000	< 3140	9310	214000	< 24	72	< 2.25
Biotite	52900	100000	10000	3230	306000	5	36	< 0.24
Biotite	12900	100000	< 1600	10500	99600	< 7	80	< 1.11
Biotite	30800	100000	< 2050	6740	119000	< 18	133	< 1.43
K-feldspar	1560	100000	6670	210	34300	< 8	< 11	< 0.62
K-feldspar	79	100000	< 605	35	< 199	< 5	36	< 0.91
K-feldspar	204	100000	13400	1270	15000	< 3	69	1
K-feldspar	103	100000	10400	802	2470	26	22	< 0.49
K-feldspar	229	100000	< 418	326	9910	11	45	< 0.76
K-feldspar	< 142	100000	88000	< 50	13100	< 16	125	< 3.89
<b>Sample Sn8N21</b>								
Muscovite	35700	100000	39300	2960	68700	65	148	< 1.45
Muscovite	17000	100000	7480	1530	39000	4	46	< 0.20
Matrix?	43300	100000	5040	4180	90000	2	43	< 0.23
Matrix?	38000	100000	9280	4680	101000	23	206	< 0.65
Muscovite	28100	100000	1850	3270	66700	< 0.83	81	< 0.24
Muscovite	21400	100000	4510	1650	43300	5	79	< 0.21
Muscovite	28600	100000	3400	2550	43500	< 0.53	136	0
K-feldspar	15900	100000	11500	2580	58900	3	85	< 0.81
K-feldspar	42900	100000	14600	3620	101000	< 2.32	60	< 1.72
Muscovite	19100	100000	17500	2730	42600	34	72	< 1.0
Muscovite	27100	100000	13300	6590	72600	< 2.74	116	< 1.3
Muscovite	36000	100000	10500	3440	85100	7	127	1
Muscovite	39100	100000	57200	4280	109000	< 3.1	201	4
Matrix	43400	100000	15500	5430	124000	3	235	1
Matrix	52800	100000	26400	4440	131000	< 1.70	119	10
Matrix	75300	100000	17700	8540	177000	24	365	< 0.94
Matrix	52400	100000	27300	5670	192000	9	307	< 0.5
Mica	17800	100000	3580	1550	30400	4	38	< 0.11
Mica	17200	100000	5260	1610	43900	3	71	< 0.19
Matrix	29100	100000	15900	4790	76400	25	166	< 0.34
Matrix	17600	100000	10300	10500	31300	< 0.41	26	1
Matrix	35700	100000	30700	4940	64600	< 1.5	93	2

Tab. B.11: LAM-ICP-MS results on samples spiked with Se

<b>Mineral</b>	<b>Mg</b>	<b>Al</b>	<b>Ca</b>	<b>Ti</b>	<b>Fe</b>	<b>Se</b>	<b>Mo</b>	<b>Sn</b>	<b>Eu</b>
<b>Sample Se8N16</b>									
Muscovite?	13000	100000	8210	2920	28100	< 24	6.04	38.4	1.04
Muscovite?	20100	100000	2370	3060	36900	138	2.45	38.3	< 0.37
Muscovite?	13300	100000	37200	1150	47500	187	18.6	63.6	11
Resin	11600	100000	10100	991	18800	< 55	5.81	26.5	< 0.26
Matrix	49300	100000	32600	6870	126000	388	6.9	237	2.02
Matrix	73300	100000	10000	7820	136000	< 90	14.1	31.6	< 0.83
Resin	73000	100000	59200	< 276	228000	3660	473	1730	< 20
Matrix	23300	100000	6630	2930	66700	164	5.66	122	1.12
Muscovite?	43300	100000	24100	4560	95200	<109	< 1	251	2.74
Matrix	17400	100000	< 9550	< 77	< 1720	< 1750	< 17	< 134	< 8
Matrix	23600	100000	22100	2100	49400	284	25.7	48.6	2.93
Matrix	29500	100000	11700	2610	50400	< 344	< 2	< 30	< 1.2
Matrix	41400	100000	15100	3220	133000	796	11.9	122	< 1.00
Matrix	31000	100000	23500	3540	130000	< 61	11.7	142	1.26
Matrix	22600	100000	7820	2670	73800	< 33	2.88	66.2	< 0.27
Matrix	14800	100000	4900	2400	30400	< 8	1.18	17.8	0.9
Matrix	50100	100000	14500	5040	92600	< 106	5.61	117	2.03
Matrix	16700	100000	9660	3340	42200	< 74	12.7	90.1	0.84
Matrix	33600	100000	18200	4030	77200	144	6.71	52.3	3.6
Matrix	53700	100000	17100	6110	198000	< 216	13.4	148	< 0.70

## Appendix C: Determination of the radiation dose and required activity

*R.P. Maguire, J.H. Missimer and K.L. Leenders*

### C.1 Introduction

A rock sample containing a fracture is to be measured in order to determine the morphology of channels in the fracture and also the porosity variations through it. The sample will be 2 m long and between 0.35 m and 0.5 m in diameter with an approximately 0.05 m porous region running its length in the centre (Fig. C.1). It is to be imaged with PET RPT-2 tomography which has a 3D acquisition 0.5 % total efficiency similar to that of the present ECAT 9334-16 scanner. It is also planned to measure smaller rock samples of length and diameter 0.2 m with a 0.01 m porous region in a feasibility study. In order to determine the activity required for the experiments and hence the radiation dose rates from the samples it is necessary to consider the attenuation problems of measuring such dense objects.

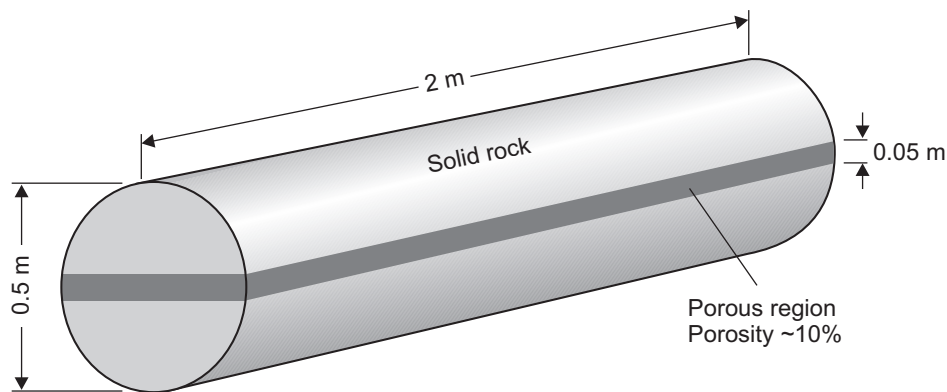


Fig. C.1: Approximate layout of the rock core